UNIVERSIDADE FEDERAL DO PARANÁ

LEANDRO ALUISIO SCHOLZ

TRACING BIOFILAMENTS FROM IMAGES: ANALYSIS OF EXISTING METHODS TO QUANTIFY THE THREE-DIMENSIONAL GROWTH OF FILAMENTOUS FUNGI ON SOLID SUBSTRATES

CURITIBA

2018

LEANDRO ALUISIO SCHOLZ

TRACING BIOFILAMENTS FROM IMAGES: ANALYSIS OF EXISTING METHODS TO QUANTIFY THE THREE-DIMENSIONAL GROWTH OF FILAMENTOUS FUNGI ON SOLID SUBSTRATES

Dissertação apresentada como requisito parcial para do grau de Mestre em Engenharia Química, no programa de Pós-graduação em Engenharia Química do Departamento de Engenharia Química, Setor de Tecnologia, Universidade Federal do Paraná..

Área de Concentração: *Engenharia Química.*

Orientador: Prof. Dr. David Alexander Mitchell.

Coorientadora: Prof. Dr. Maura Harumi Sugai-Guérios.

CURITIBA

2018

Catalogação na Fonte: Sistema de Bibliotecas, UFPR
Biblioteca de Ciência e Tecnologia

S368t Scholz, Leandro Aluisio
Tracing biofilaments from images: analysis of existing methods to quantify the three-dimensional growth of filamentous fungi on solid substrates / Leandro Aluisio Scholz. – Curitiba, 2018.

Tese - Universidade Federal do Paraná, Setor de Tecnologia, Programa de Pós-Graduação em Engenharia Química, 2018.

Orientador: David Alexander Mitchell – Coorientador: Maura Harumi Sugai-Guérios.

1. Fungos. 2. Fungos filamentosos. 3. Imagem tridimensional. I. Universidade Federal do Paraná. II. Mitchell, David Alexander. III. Sugai-Guérios, Maura Harumi . IV. Título.

CDD: 579.5

Bibliotecário: Elias Barbosa da Silva CRB-9/1894

MINISTÉRIO DA EDUCAÇÃO
SETOR SETOR DE TECNOLOGIA
UNIVERSIDADE FEDERAL DO PARANÁ
PRÓ-REITORIA DE PESQUISA E PÓS-GRADUAÇÃO
PROGRAMA DE PÓS-GRADUAÇÃO ENGENHARIA QUÍMICA

TERMO DE APROVAÇÃO

Os membros da Banca Examinadora designada pelo Colegiado do Programa de Pós-Graduação em ENGENHARIA QUÍMICA da Universidade Federal do Paraná foram convocados para realizar a arguição da Dissertação de Mestrado de **LEANDRO ALUISIO SCHOLZ** intitulada: **Tracing biofilaments from images: Analysis of existing methods to quantify the three-dimensional growth of filamentous fungi on solid substrates**, após terem inquirido o aluno e realizado a avaliação do trabalho, são de parecer pela sua aprovação no rito de defesa.

A outorga do título de mestre está sujeita à homologação pelo colegiado, ao atendimento de todas as indicações e correções solicitadas pela banca e ao pleno atendimento das demandas regimentais do Programa de Pós-Graduação.

CURITIBA, 29 de Maio de 2018.

DAVID ALEXANDER MITCHELL
Presidente da Banca Examinadora (UFPR)

DANIEL WEINGAERTNER
Avaliador Externo (UFPR)

MARCO ANTONIO FERREIRA RANDI
Avaliador Externo (UFPR)

Rua Cel. Francisco Heráclito dos Santos, s/nº - CURITIBA - Paraná - Brasil
CEP 81531-980 - Tel: (41) 3361-3590 - E-mail: ppgeq@ufpr.br

I dedicate this dissertation to my mother and father, Ivone and Paulo. This dissertation is also dedicated to Luiz Henrique Douat, for his presence could have made my path even more pleasant and happy.

Acknowledgements

I would like to thank a few individuals who I worked with and also those who participated in my life during this period. First, I thank professors David and Maura for everything they taught me during this period, for every discussion, fruitful or not, and every conversation about my future prospects. Even more important, David and Maura relied on me and gave me the freedom I needed to conduct this project in such a way that made it possible for me to meet and discuss with the researchers in other international institutions. I will be forever thankful and I wish to be able to continue working with them in the future.

I would also like to thank the examiners of this Masters project, who took their time to read this document and participate in my defense. If I could, I would invite more than just three so the discussions would be even more fruitful. I would like to give special thanks to Sébastien Tosi (IRB Barcelona) who could not manage to participate formally in the examination but contributed with many suggestions and comments.

Beyond the aforementioned individuals, I wish to thank the funding agency CAPES for awarding me a scholarship during the 24 months of my masters. I must also thank the European Molecular Biology Laboratory (EMBL) for awarding me the EMBL Advanced Training Centre Corporate Partnership Programme Fellowship so I could attend to the Bioimage and Data Analysis Course in Heidelberg in the spring of 2017. There I could meet members of the Network of European Bioimage Analysts (NEUBIAS).

My thanks must also go to the Chemical Engineering Postgraduate program (PPGEQ - UFPR) for accepting me as a student, especially the coordinator Prof. Dr. Alexandre F. Santos and the secretary Cintya Kuznharski for the support over the last two years. Special thanks go also to UFPR microscopy facility and its staff, now with the name of Centro de Técnicas Avançadas em Fluorescência (CTAF), where Maura performed the experiments and obtained the images used in this work. The members of our research group LTFE (Laboratório de Tecnologia Fermentativa e Enzimática) and LTEB (Laboratório de Tecnologia enzimática e biocatálise) must also be reminded. Special thanks to Janaína de Almeida, Gerson Mello, Robson Alnoch, Glauco Dias, Anelize Finkler, Luana Pitol, Rafaela Pinter, Ana Clara Caznok, Karina Lobermayer, Amanda Souza and also Sara Jimenez Correa, one of our temporary visitors. It was great to work with all of you.

Apart from the academic colleagues and institutions, I would like to thank my whole family, specially my mother Ivone and her partner Thiago Ricelli Silva, my father Paulo, my sister Fernanda, and my step-brother Luiz Ricardo and his beloved Ana Paula for all the support and care you have always given me. Apart from them, I must be grateful for the greatest friends I have, Alex Machado, Felipe Cardinot, Flávia M. Pereira and Alexandre Malheiros. Thanks for all the conversations, the laughter and also the serious conversation over all these years. Also, I thank my friends from political movements and the friends I made because of my love for rock climbing: Paulo Palozi, Paulo Oliveira, Lucas Cipolla, Rômulo Fontanelli and Michelle Maia.

Finally, the most special and warm thanks must go to my partner, Beatris Martin and our recently adopted and loving dog, Charlotte. We have been together for quite a while and experienced many turbulent times, but I must say I am grateful to have met you that day. Your thoughtfulness, love, care and support is impossible to describe and they were crucial during my masters.

RESUMO

Análise de imagens de biofilamentos tem se tornado uma parte importante na pesquisa em biologia e biotecnologia, pois ela não só elucida a morfologia destas estruturas, mas também fornece ideias sobre o desenvolvimento destas estruturas. Além disso, a morfologia pode ser correlacionada com outras variáveis. Por exemplo, análise de imagem de fungos filamentosos permite correlacionar produtividade de enzimas com diferentes morfologias. Há um interesse em compreender como o micélio de um fungo filamentoso se desevolve ao crescer em substratos sólidos. Para estudar isso, foram obtidas imagens 3D do fungo em crescimento em diversos tempos, objetivando computar dados da morfologia e dinâmica de crescimento: velocidades de extensão da colônia e de pontas, número e posição de ramificações e pontas, comprimentos de segmentos, entre outros dados. Porém, antes de computar estes dados, foi feita uma análise da literatura de métodos de traçado de biofilamentos. A análise foi realizada para facilitar a compreensão do vasto número de métodos disponíveis, desde componentes individuais (e.g. técnicas de realçe de filamentos) a *workflows* completas de traçado de biofilamentos. Também há muitas opções de implementações de software. Na análise, foram incluídas 87 publicações envolvendo *workflows* de traçado de filamentos ou componentes. Para a análise, criou-se uma classificação (10 classes, que incluem interação com o usuário, abordagem teórica, técnica de imageamento, entre outras classes e 120 sub-classes) para apoiar a análise com o uso de conceitos de teoria de grafos. A metodologia proposta poderá ser utilizada no futuro com ferramentas de semântica web e uma base de dados e permitirá analisar um número maior de dados. Desta análise, identificaram-se os métodos mais comuns de melhoramento de imagem (Realçe de filamentos, 44.9%, suavização, 16.3% e Subtração de *background* 14.3%) e as tendências em abordagens teóricas (e.g. abordagens baseadas em grafos juntas à algoritmos de aprendizado de máquina, realçe de filamentos como o *gradient vector flow* seguidos de abordagem *Level-set fast-marching*). Após a análise da literatura, foram selecionados os métodos de melhoramento mais comuns e avaliados segundo seu impacto na qualidade da imagem. Os testes foram realizados em duas amostras de imagem (experimentos do crescimento de *Aspergillus niger* de microscopia confocal de varredura a laser) através de um planejamento fatorial completo e análise do índice de similaridade estrutural, SSIM, e razão sinal-ruído, SNR. Resultados mostraram que o algoritmo *rolling ball* de subtração de *background* com raio 20 pixels teve o maior efeito positivo em SSIM e SNR no geral. Então, ao utilizar as imagens melhoradas como entrada, foram testados 5 métodos de traçado de filamentos (APP, APP2, NeuTube, NeuronStudio e NeuroGPS-Tree). Os resultados do traçado foram avaliados qualitativamente: O método NeuTube mostrou os resultados visualmente mais acurados. Definiu-se então o método e foram traçadas as imagens completas 3D e no tempo e obtivemos parâmetros morfométricos e da dinâmica do crescimento do fungo (perfis de biomassa e comprimentos totais, por exemplo). Embora se observe que o uso de traçado de filamentos é promisor para obter mais dados do crescimento de fungos filamentosos, discutiu-se a necessidade de aprimorar as técnicas de preparo de amostra e das configurações na aquisição das imagens, de maneira a aumentar a qualidade final das imagens e fornecer resultados mais confiáveis e concretos após o traçado para então tirar conclusões dos dados.

Palavras-chave: fungos filamentosos, filamentos biológicos, análise de imagem, traçado de filamentos, melhoramento de imagem.

ABSTRACT

Image analysis of biofilaments is becoming an important part of research on biology and biotechnology because it does not only elucidates the morphology of such structures but also gives insights into their development. Additionally, the morphology can be correlated with other variables. For example, image analysis of filamentous fungi allows the correlation of enzyme productivity with different morphologies. We are interested in understanding how the mycelium of a filamentous fungus develops during growth on solid substrates. In order to study that, time-lapsed 3D images of the fungus during growth were obtained, with the intention of computing growth dynamics and morphometric data: colony and tip extension rates, number and positions of branches and tips, segment lengths, among others. However, prior to computing this data, we analysed the literature of biofilament tracing methods. The analysis was done to facilitate the understanding of the vast number of methods available, from single components (e.g. filament enhancement techniques, and specialized model-based approaches) to complete biofilament tracing workflows. There were also many software implementations options. The analysis comprised 87 publications proposing complete biofilament tracing workflows or workflow components. For the analysis, we created a classification methodology (10 main classes, including user interaction, theoretical approach, imaging technique, among other classes and 120 sub-classes) and analysed the publications using graph theory concepts. The proposed methodology could be used in the future with semantic web tools and crowd-sourced web-based databases, allowing the analysis of greater number of data. Out of this analysis, we identified the most common image enhancement methods (Filament enhancement 44.9%, smoothing 16.3%, background subtraction 14.3%) and the theoretical approach trends for biofilament tracing (e.g. graph-based approaches coupled with machine learning algorithms, image enhancement such as gradient vector flows followed by model-based fast marching approach). Following the literature analysis, we selected the most common image enhancement methods to be used prior to biofilament tracing and evaluated their impact on image quality. The tests were done on two sample images (experiments of the growth of *Aspergillus niger* on two different carbon sources obtained by confocal laser scanning microscopy) through a full factorial design of experiments and analysis of the structural similarity index, SSIM and signal-to-noise ratio, SNR. Results show that background subtraction (Rolling-ball algorithm, 20 pixels radius) had the most positive effect on SSIM and SNR. Then, using the enhanced images as input, we tested 5 different biofilament tracing methods (APP1, APP2, NeuTube, NeuronStudio and NeuroGPS-Tree). We evaluated the tracing results visually and qualitatively: NeuTube was the method with the most visually accurate results. After choosing NeuTube as the best method, we applied it to our complete 3D time-lapsed images and computed some growth dynamics and morphmetric parameters (e.g. biomass profiles, segment and total lengths). Although we indicate that biofilament tracing methods are a promising approach to obtain more data on the growth of the filamentous fungi, we discuss the need to improve the sample preparation techniques and image acquisition set-up in order to increase the quality of the images so the tracing results provide more reliable and concrete results to draw conclusions.

Keywords: filamentous fungi, biological filaments, image analysis, filament tracing, image enhancement.

List of Figures

List of Tables

List of Acronyms

CFD	Computational Fluid Dynamics
CLSM	Confocal laser scanning microscopy
eGFP	Enhanced green fluorescent protein
FAIR	Findable, accessible, interoperable and reusable
Glu	Glucose
GUI	Graphical user interface
HVS	Human visual System
LSFM	Light sheet fluorescence microscopy
MIP	Maximum intensity projection
MSE	Mean-squared error
NA	Numerical aperture
PGal	Polygalacturonate
PSF	Point spread function
PSNR	Peak signal-to-noise ratio
px	pixel(s)
RGB	Red, green and blue
ROC	Receiver operating characteristic
SEM	Scanning electron microscopy
SmF	Submerged fermentation
SNR	Signal-to-noise ratio
SSC	Solid substrate cultivation
SSF	Solid-state fermentation
SSIM	Structural similarity index
TED	Tree edit distance
UFPR	Universidade Federal do Paraná (Federal University of Paraná)
YOP	Year of publication

List of Symbols

φ	Biomass concentration, in mg dry weight $/cm^3$
D	Depth of the axial field of an image (z axis)
k	index of the slice of the volumetric image
T	Diameter of the hiphae in in micrometers
x	length of the image, in μm (Equation 5.2)
z	depth of the image, in μm (Equation 5.2)
X_k	Biomass volume in slice k, in μm^2
V_k	Volume of the slice k, in in μm^2
$y_{k,min}$	upper value of the xz plane of slice k
$y_{k,max}$	lower value of the xz plane of slice k
L_{edge}	Euclidean distance between two nodes (edge) from the graph representation of the traced biofilments
$L_{edge,i}$	Euclidean distance between two nodes (edge of index i)
d_{hypha}	Estimated diameter of the hyphae of the traced biofilaments
n_{edges}	number of edges in the graph or subgraph
n_i	number of tips at time i
$K_{cross,i}$	fraction of the edge i ($0 \leq K_{cross} \leq 1$) that crosses either upper or lower xz planes of the slice
t_i	Time in which the image frame i was taken
$L_{total,i}$	Total length of the traced biofilament at time i
dL/dt_i	colony extension rate at time i
dt_i	time elapsed between frames, in h
$q_{tip,i}$	tip extension rate, in μm.h^{-1}, at time i

Contents

1 Introduction

In industrial biotechnology there is an interest in understanding how filamentous fungi grow in a fermentation system and how filamentous fungi generate products of interest, for example hydrolitic enzymes, i.e. lipases and pectinases, and secondary metabolites, such as penicillin. One approach used to gain understanding and optimize fermentation systems is to study the relationship between the morphology of the growing mycelium and the production of such products of interest.

Among the different types of fermentation systems, solid substrate cultivation (SSC) also known industrially as Solid-state Fermentation (SSF), is an alternative to the well established systems such as sumberged fermentation (SmF). SSC has advantages when compared to submerged fermentation. For example, it shows increased productivity of hydrolytic enzymes due to more favourable growth conditions for fungi. SSC also allows the use of agro-industrial waste nutrient sources, such as citric pulp (orange peel and bagasse) (Bhargav et al., 2008) and the fermented solid, the end product of the SSC process containing the produced enzymes and microorganism, may be used to catalyse a reaction of interest (Pitol et al., 2017). However, SSC occurs in a more complex environment, in which the relationship between morphology and productivity is still unclear. When on a surface of a solid substrate, the fungus grows in a heterogeneous system that comprises a continuous gas phase (Moist Air), a moist solid phase and an additional liquid biofilm, which may either be formed or not depending on the stage of growth and the conditions of the environment. As a result, the fungus shows quite a complex morphology: its hyphae do not only grow in the surface of the substrate (surface hyphae), but also over it (aerial hyphae) and underneath the surface of the substrate (penetrative hyphae), producing a three-dimensional (3D) biomass distribution. For this reason, fungal growth and its morphology on solid substrate is difficult to study and needs to be better understood.

In order to study fungal morphology, it is necessary to observe the growth of filamentous fungi. For this purpose, one must count on images. These images may be obtained by different techniques, depending on the desired scale of observation, but light microscopy (i.e. bright field and confocal) is the most common way of acquiring images of a growing fungus. During this project, time-lapsed 3D images obtained by a confocal laser scanning microscope (CLSM) will be used. Such images have certain characteristics: dark background and bright foreground objects, low contrast and uni-modal pixel intensity distributions and the presence of the complex mycelial network. One of the concerns in this project is to properly evaluate the quality of the image and evaluate if they can be used to extract realiable and accurate data. Thus, it is important to consider possible changes to sample preparation procedures and image acquisition settings that could improve the quality of the images so they can be used for further image analysis.

With the images in hand, the next important step is to obtain desired morphological and growth dynamics data from these images. The data are obtained by using image processing and analysis methods and, more specifically, biofilament tracing methods. Such methods may vary in many ways: some are developed to process three-dimensional images, some were developed to function for a specific imaging technique or filament complexity. Other image analysis methods

may be robust and be capable of working properly on images of low quality (for example noisy images, images with inhomogeneous illumination). One issue we face is that there are not many studies on the growth or morphology of filamentous fungi on solid substrates that apply image processing and analysis methods, especially with 3D images. However, the field of bioimage analysis provides a broad literature if the search is expanded to biofilament tracing methods in general. The morphology of neurons (Donohue e Ascoli, 2011), plant roots (Lobet et al., 2013), blood vessels (Kirbas e Quek, 2003) and even cytoskeletal structures (Xu et al., 2015) of cells have been studied and many biofilament tracing methods are available. In fact, the field of image analysis applied to biological images (bioimage analysis) has grown considerably in the last decade. Thus, given the great complexity and variety of the literature on image analysis and biofilament tracing methods, it is important to analyse the options and make an educated choice of which methods are suited to be used in the images and study the growth and morphology of the fungus. This is the main focus of the present work.

In this project, the focus is on two main issues. First, there are many biofilament tracing methods available in the literature, but researchers who study fungal growth and morphology need to learn about them and identify what are the most appropriate to their images. Therefore. it is important to organize and classify the literature of biofilament tracing methods and in this work, we propose a classification methodology, provide information on the main theoretical aspects and principles of biofilament tracing methods available in order to help solve the issue of having too many methods and options of implementations available. The second issue relates to the choice and benchmarking of filament tracing methods. In order to address that, we evaluate results of image enhancement methods, filament tracing methods and results of the computation of growth dynamics and morphometric data from the images obtained by our research group. In addition, based on the results of these steps, we propose modifications on the procedures to obtain the images, which include the sample preparation step and the image acquisition set-up. Finally, we begin a discussion of future efforts on benchmarking of biofilament tracing methods, which is a key part for the improvement of existing methods, the development of new biofilament tracing methods and the increase the communication between all researchers who are interested in tracing biofilaments.

2 Fundamental theory

In this chapter, we present the fundamental theory of the four areas related to our work: fungal growth theory, fungal morphology and topology, microscopy (especially confocal microscopy) and image analysis. But first, we explain why the choice of studying filamentous fungi.

2.1 Why filamentous fungi? Why solid-state fermentation?

Penicillium crysogenum, Aspergillus niger, Trichoderma reesei, and *Rhizopus oryzae* are all examples of filamentous fungi. Beyond that, they are industrially relevant filamentous fungi. They have been used in food processes for centuries to produce soy sauce,*tempeh*, and many types of cheese. In addition, these and many other fungi produce quite a wide variety of bioproducts, ranging from antibiotics to hydrolytic enzymes. Their use in the industry has only increased in past decades. For example, in the antibiotics market, whose products are produced mainly by fungi, from 2005 to 2009 the 42 US$ billion global market has increased the sales in the major antibiotic classes, cephalosporins by 3.4% and broad-spectrum penicillins by 5%, respectively (Hamad, 2010). The 4.2 US$ billion (2015) enzyme market also is expected to reach high economic growth, with an annual growth rate of 7% from 2015 to 2020 (Singh et al., 2016).

2.2 The growth of filamentous fungi and their morphology

2.2.1 Basic definitons and concepts

In order to understand this project, it is crucial to describe how a filamentous fungus grow. But let us first specify a few details about this group of living organisms. Filamentous fungi are eukaryotic[1] microorganisms and they have their own kingdom in the phylogenetic tree[2], known as *Fungi*. Fungi may develop in two basic morphologies, yeasts and hyphae, and fungi in the latter form are also known as filamentous fungi. However, some fungi may alternate between yeast and hyphal forms (Kües e Fischer, 2006). With respect to feeding capabilities, fungi are heterotrophic organisms and do not fix carbon as plants do. In other words, the complex nutrients neccesary for their growth (e.g. the famous monosaccharide glucose) are absorbed from the environment, passing through the cell wall and plasma membrane (Alexopoulos et al., 1996). These nutrients, usually polysaccharides such as starch, pectin and cellulose, cannot be absorbed by the fungus as they may be quite big molecules. They need to be 'digested' into smaller pieces, monosaccharides, through the secretion of digestive enzymes and then absorbed by the fungus.

[1] An organism consisting of a cell or cells in which the genetic material is DNA in the form of chromosomes contained within a distinct nucleus. Eykariotic organisms have specialized cell organelles, such as mithocondria and the endoplasmic reticulum.

[2] The phylogenetic tree is the diagramatic representation of the evolutionary development and diversification of all living organisms

Now, knowing these basic definitions and concepts, it is possible to describe fungal growth and morphology into more detail.

2.2.2 Description of the life cycle and the growth of filamentous fungi in solid media

Fungi reproduce by forming spores, which are part of the fungal reproductive cycles. Spores are specialised cells of the fungus that can function as resting or dispersal propagules and each spore has the potential to generate another individual of the species, provided that certain conditions are met. In this section, we refrain from describing all types of fungal spores and reproductive cycles by focusing on the life cycle of fungal *Genus Aspergillus*, of which *A. niger* is the model organism of the present work. Refer to the well known refence book series *The Mycota*, especially volume I by Kües e Fischer (2006) for more details about the many spore types and reproductive cycles.

As stated before, a spore may grow and generate another individual provided certain conditions are met. These conditions are general and common to most fungal species. First, the spore needs free water to activate. In some cases it is sufficient that the environment has high relative humidity. The second condition is the presence of oxygen, since fungi are obligate or facultative aerobes and the spores usually need oxygen to be activated. An optional, tough common condition, is the presence of carbon dioxide, because it acts as a primer for various biochemical reactions. Finally, spores activate under certain temperature ranges, usually narrower than those of vegetative growth[3] (Carlile et al., 2001).

The life cycle in *Genus Aspergillus* may be sexual, assexual or parasexual. However, *A. niger* only reproduces assexually (Casselton e Zolan, 2002; Pel et al., 2007). Figure 2.1 depicts the three different life cycles. The orange arrows in Figure 2.1 describe the assexual cycle. For growth on solid substrates, assume that the spore is in contact with both the solid substrate and the air and has the conditions to start growing. If spore activation conditions are met, the spore, also known as conidiospore, activates and begin to swell mainly due to the absorption of water. At this moment, the spore changes from a latent or dormant state and goes through a series of physiological changes that marks the beginning of the somatic phase, also known as vegetative growth phase.

After activation and swelling, the spore starts taking up nutrients from the environment to grow and one or more germ tubes appear. The germ tube typically takes the form of a hypha, an approximately cylindrical shape cell compartment, and elongates exponentially, as a result from the rapid nutrient absorption that follows its appearance. After the germ-tube reaches a certain length, commonly 60-200 μm (Trinci, 1974), it starts mitotic cell division and creates branches of new hyphae. The new hyphae, in turn, continue to explore the vicitiny and take up nutrients and also produce new branches. The first hyphae commonly remain in the surface of the substrate and grow in an organized way such that an hypha avoids getting in contact with other neighboring hyphae. This characterizes the beginning of the development of the mycelium of a single colony (originated from a single spore), the complex network of interconnected hyphae.

As the hyphae in the surface of the substrate continue growing and foraging for nutrients, the mycelium may find hyphae from another colony. Hyphae may then start changing their growth direction to avoid contact with other hyphae, while other hyphae may cross one another or even stop growing. At this stage, hyphae have likely explored the whole surface of the substrate or may have generated an amount of biomass that requires more nutrients than the surface hyphae alone can provide in order to be maintained. Hence, hyphae may start penetrating the solid substrate or

[3] Vegetative growth, or the somatic phase of a filamentous fungus comprises the growth stage in which the fungus multiplies its cells mitotically, and does not produce any specialized reproductive cells or structures.

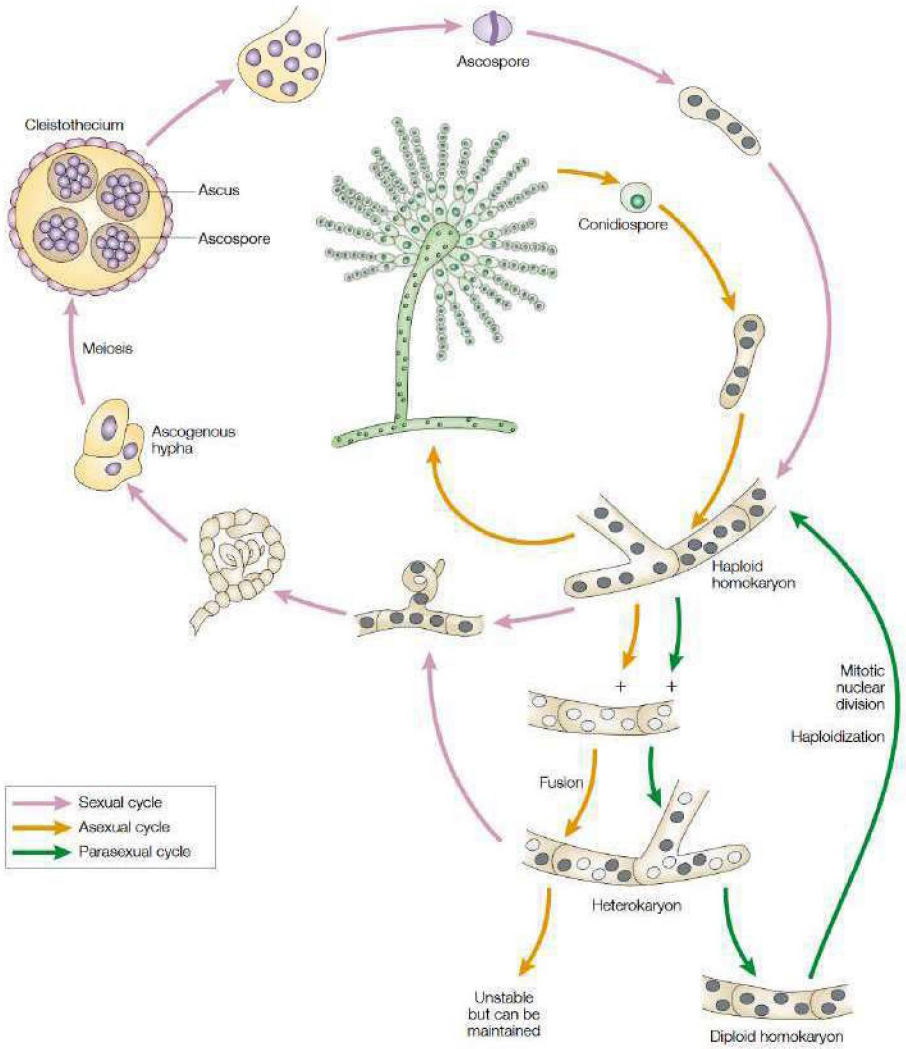

Figure 2.1: Representation of the sexual, assexual and parasexual reproductive cycles of the *Genus Aspergillus*. Reprinted by permission from Macmillan Publishers Ltd: Nature Reviews Genetics, Casselton e Zolan (2002), copyright 2002.

growing above the surface, therefore increasing the density of the mycelium. As a result, the mycelium comprises hyphae that grow in contact with different phases of the system: hyphae located mainly on the surface of the substrate (surface hyphae), beneath the surface (penetrative hyphae) and above the surface (aerial hyphae). This is an important point in the current research on fungal growth on solid media (Sugai-Guérios, 2016; Rahardjo, 2005).

At a certain point during the growth of the mycelium, cues may cause the fungus to begin changing from its vegetative phase to the reproductive phase, in which the production of assexual reproductive structures and spores take place. We also call this phenomena sporulation. Similar to stage change of a spore from dormancy to activation, the change from vegetative growth to the sporulation (or reproductive) phase will occur under certain conditions. Sporulation usually begins when mycelial growth rates decline (Moore-Landecker, 2001) and also begins as a response to nutrient exhaustion (Carlile et al., 2001), although some fungi can grow vegetatively and sporulate at the same time. Moreover, the environment must provide proper nutritional conditions along with proper temperature, light, pH, water availability (moisture) and oxygen availability. It is reasonable to assume that the mycelium grows vegetatively in much broader ranges of conditions than in the reproductive phase and the latter starts as signals indicate that, if the fungus is to survive, it must sporulate and disperse the spores in the environment. In order to

do that, sections of the mycelium start the process to produce the conidiophores, the flower-like structure shown in the center of Figure 2.1. Genetically, the conidiophores and conidiospores are simple structures and the requirements for their development are similar from those of the vegetative mycelium. The conidiophore bears a number of conidiospores, ready to be dispersed and find new areas do grow and forage for nutrients, therefore granting the chance for the fungus to survive (Moore-Landecker, 2001; Carlile et al., 2001). Figure 2.2 shows *Aspergillus niger* conidia observed by scanning electron microscopy (SEM).

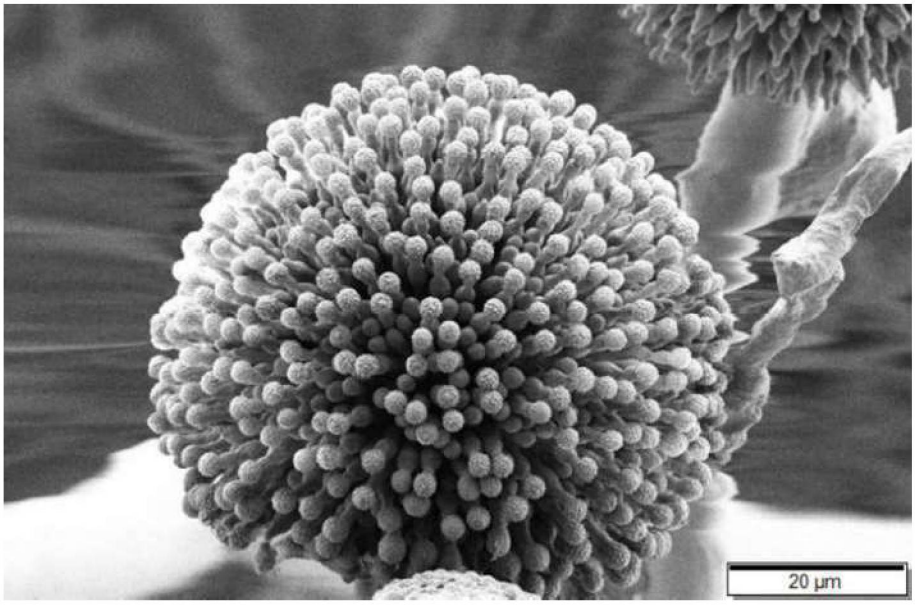

Figure 2.2: *Aspergillus niger* conidia prepared using the freeze drying method, SEM image (Murtey e Ramasamy, 2016).

Now the two alternative lifecycles, namely sexual and parasexual, are briefly described. The parasexual cycle may occur when when hyphae or mycelia with genetically different nuclei cross with each other. The resulting mycelium is not stable if continues to grow vegetatively and reproduce assexually. Then, the haploid[4] nuclei with different genetic material may fuse, forming diploid nuclei , and will continue vegetative growth. Over time, random chromossome losses will restore the haploid chromossome number and generate a genetically different organism. The green arrows in Figure 2.1 indicate the parasexual cycle. In the case of sexual cycle, the fruiting body develops, where a pair of nuclei destined for meiosis divides, forming the ascogenous hypha. These hyphae then become specialized cell, in which the two haploid nuclei fuse and then meiosis generates the ascospores (the spores resultant from sexual reproduction). The fruiting body, named cleistothecium, holds thousands of ascospores, which will be dispersed similarly to the conidiospores when the cleistothecium opens (Casselton e Zolan, 2002).

2.2.3 How is the morphology related to stages of the growth on a solid surface?

As the reader now understands the basic principles of the growth, development and reproduction of a filamentous fungus, the discussion follows with more details into how fungal growth on solids can be characterized with respect to the morphology.

[4] an haploid cell has a single set of unpaired chromossomes, whereas a diploid nuclei has two complete sets of chromossomes. For example, *Aspergillus nidulans*, a haploid nuclei has 8 chromossomes and a diploid has 2.8 = 16 chromossomes.

The growth of a filamentous fungus on solid substrates is the major mode of growth found in nature and where all hyphal types to be described here are present. So, let us first direct the focus on the vegetative growth of the mycelium on a solid surface. As the germ tube and the first hyphae appear, most of the mycelium grows in the surface of the substrate, which can be considered roughly a growth in two dimensions: through the width and length of the surface. Occasionally, some hyphae may penetrate the solid substrate if there is enough dissolved oxygen in the medium (Rahardjo, 2005). This two-dimensional growth can be considered the first stage. Hence, we characterize the mycelium in this stage as surface mycelium. However, it is more common to give the name to the hyphae as surface hyphae. The growth pattern follows a polarized hyphal growth[5], where the hyphae expand radially from the initial location of the spore. This pattern is well known and has been studied for many decades and has provided valuable insights into how growth occurs in a bigger scale, the visible scale of the mycelium (Trinci, 1971).

The next stage involves expanding the reach of the mycelium further on the surface of the substrate as well as expanding the reach of nutrients beneath the substrate surface. Surface mycelium become more dense and some hyphae begin penetrating the solid substrate. The growth of such hyphae tends to be perpendicular to the substrate surface. These hyphae are known as penetrative hyphae. In addition to hyphae growing beneath the surface, some hyphae may also start growing above the surface, although not necessarily at the same time that the penetrative hyphae appear. The hyphae growing above the substrate surface are known as aerial hyphae. Aerial hyphae may be either in contact with the air phase or with a thin layer of free water (commonly referred to as biofilm) that often appears near the surface of the substrate as a result of the increased density of mycelium near the surface (Rahardjo, 2005). Biofilm hyphae is the name given to the hyphae in contact with the water layer.

At this stage, the mycelium adds another dimension to its growth pattern and shows higher morphological complexity on a three-dimensional growth pattern: as opposed to the radial expansion of the surface hyphae, penetrative hyphae do not show a radial expansion pattern. The first penetrative hyphae grow approximately perpendicular to the surface of the substrate and as they develop, new hyphae may as well grow perpendicular to the surface or grow in different patterns. In fact, penetrative hyphae may grow in different ways, as it has been noted in previous works (Sugai-Guérios, 2016; Nopharatana, 1999). Similarly, aerial hyphae may also show different growth patterns, as observed in the thesis of Sugai-Guérios (2016), but such patterns are yet to be further elucidated.

Finally, as the mycelium grows in three-dimensional space, aerial hyphae will grow higher above the substrate surface and increase biomass in previously occupied heights. Oppositely, penetrative hyphae will grow deeper beneath the substrate surface and also increase biomass density. At a certain point during the growth, environmental conditions may change that allow the mycelium to start producing reproductive structures. In the case of *Aspergillus niger*, conidiophores appear. Apart from being the spore producers, the conidiophores have three main features: first, they have greater hyphal diameter compared to vegetative hypae. Second, they do not produce branches from the main hypha. Thrid, conidiophores can grow to much higher heigts above the substrate surface compared to aerial hyphae. The resulting mycelium shows three areas: The growing front, comprising less dense mycelium and located at the edge of the mycelium radius, the dense vegetative mycelium and the reproductive hyphae which began growing above the vegetative mycelium (see Figure 2.3).

The growth of a fungus is divided into three main stages with respect to morphology. In addition, the hyphae are separated into five types, depending on the environment they are

[5] Polarized growth of a hypha is characterized by its unequal growth direction. The plarization of a hypha depends on the cytoskeleton and its dynamics (Kües e Fischer, 2006)

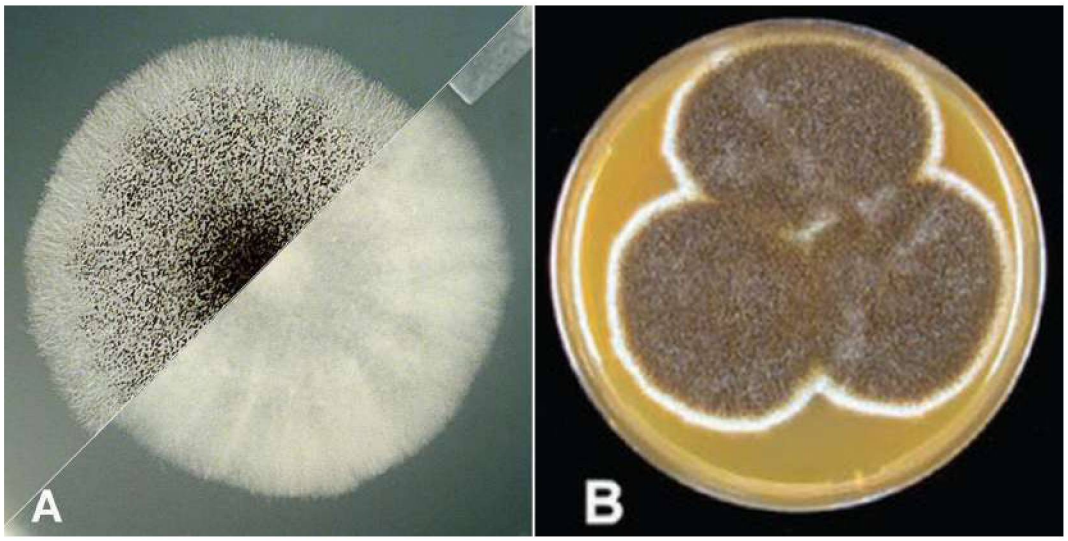

Figure 2.3: (A) *Aspergillus niger* colony in agar culture medium (Not specified) INSPQ (2010). © Gouvernement du Québec, Institut national de santé publique du Québec, 2010. (B) another colony of *Aspergillus niger* grown in malt extract agar (MEA) for 7 days and 25^oC (Samson et al., 2007). Both colonies show the less dense growing front and the more developed region, where reproductive aerial hyphae are present and the mycelium is more dense.

in contact with (Rahardjo et al., 2006). Hyphal types are: surface, penetrative, aerial, biofilm, and reproductive aerial hyphae. Recent studies suggest that penetrative hyphae can be further separated into two different types, long penetrative hyphae (scouting) and short penetrative hyphae (Nopharatana, 1999; Sugai-Guérios et al., 2016; Sugai-Guérios, 2016). The visible difference between these two types is their position in the medium and their topology. Long penetrative hyphae, named as scouting penetrative hyphae (Sugai-Guérios et al., 2016), appear to produce fewer branches and penetrate deeper into the substrate, whereas vegetative penetrative hyphae are shorter and stay near the substrate surface and show more branches. Sugai-Guérios et al. (2016) also suggests that these hyphae have different functions and physiological states: scouting penetrative hyphae explore the composition of the substrate and search for new colonization sites and they do this by secreting a pool composed of different hydrolytic enzymes that will act on the extracellular medium and hydrolyse the substrates. The hydrolysis products will then trigger the fungus to secrete the appropriate enzymes for the substrates present in the medium.

This section presented the different stages in the growth of a filamentous fungus on a solid surface and the different types of hyphae, with a classification based in spatial position and the medium that the hyphae are in contact with. In section 2.3 we will show the importance of these morphological observations, which add to the understanding of fungal physiology and productivity.

2.3 Fungal morphology and its importance

The study of the morphology of filamentous fungi has contributed to understand fungal growth and correlate the morphology with many parameters of interest. However, these studies were mainly focused on a different type of growth, submerged fermentation (SmF). In submerged fermentation, the fungus grows in a continuous liquid phase in which the main nutrient source and the other key nutrients are dissolved (oxygen, salts, etc). Depending on the culture system configuration and origin of the nutrients, the continuous liquid phase may be mixed with a discontinuous gas phase (air bubbbles) and small solid particles. The discontinuous gas phase

commonly appears due to mixing of the fermentation broth in order to ensure proper oxygen distribution and the solid particles may be part of the nutrient source and contribute to the initiation of the growth and mycelial aggretation. In the following sections, we discuss the use of morphometric data obtained through image analysis for different purposes: correlate morphology with fermentation broth rheology and transport phenomena, correlate fungal morphology with different physiological states and use morphology data in fungal growth models. In case the reader is interested in finding more details about the possibilities of the use of fungal morphology information, the comprehensive reviews of Grimm et al. (2005), Papagianni (2004) and Krull et al. (2013) can be found in the literature.

2.3.1 Morphology, transport phenomena and the rheology of the fermentation broth in submerged fermentation

It was noted that, in an SmF bioreactor, the viscosity of a fermentation broth increased drastically when the mycelia in the system were shorter, fragmented and compact (Van Suijdam e Metz, 1981). Metz et al. (1981) argued that even if this was known, most of the studies of the morphology of fungi were qualitative. The authors developed a semi-automated quantitative method to examine dispersed mycelia in SmF. Their work relied on a digitizing table upon which an image from the microscope could be projected and then a number of points along the hyphae were determined. After defining points of the hyphae on the computer (tips and branch points), they computed the distances between points and measured several variables: length of the main hypha, total length of all hyphae of a single particle, the mean length of the branches, the mean length of the segments and the number of branches. With these measurements three additional variables could be determined: the hyphal growth unit (HGU), mean hyphal diameter and the dimensionless effective length. Although a novelty in that period, their method was not accurate and depended on an operator to define the points to be calculated. The method was a step forward towards better quantitative measurements of filamentous fungi, and indicated that the three most useful measurements of dispersed mycelia that correlated with the fermentation broth rheology were the length of the main hypha, the total hyphal length and the HGU.

The introduction of more robust, reliable and faster methods using image analysis was made by a series of publications from Packer e Thomas (1990), Tucker et al. (1992) and Cox e Thomas (1992). With the studies in the area during that period, these researchers went from a semi-automated image analysis method that only analysed disperse branches to a fully automated image analysis system that was capable of analysing dispersed mycelia, clumped and aggregated mycelia, the latter commonly known as pellets. Packer e Thomas (1990) added the calculation of the proportion of biomass in clumps and aggregates, because in some cases, the proportion of clumps and aggregates was significantly high and could affect the rheological properties of the fermentation broth. Based on this observation,researchers further evaluated the morphology of the clumps and aggregates, because they wished to quantify their influence on the rheology of the broth. Tucker et al. (1992) took the calculations forward and proposed the calculation of the area, perimeter,clump circularity - an estimate of clump roughness - and clump compactness in addition to the previously defined variables. Their study focused on the development of a novel and faster computation methodology for morphometric data instead of correlating of morphology data with broth rheology, although rheology was the main reason these studies had been carried out. Furthermore, Cox e Thomas (1992) identified two different regions of the pellet morphology: the core and the annular region, whose analysis was possible with the use of the same variables proposed by Tucker et al. (1992). Some morphological measurements are represented in the following figure.

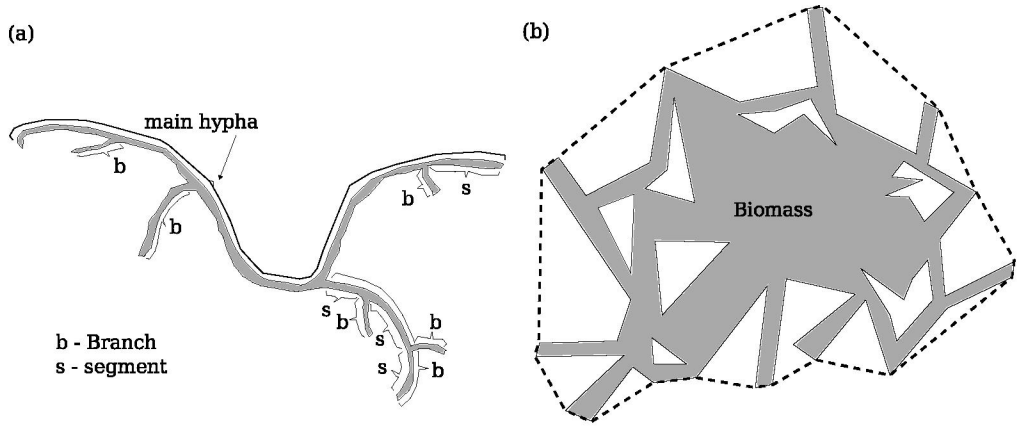

Figure 2.4: Representation of some morphological measurements of filamentous fungi in their different morphologies (a) fragmented hyphae, whose main hypha, branches and segments are identified .(b) clump or pellet. external solid lines (-) perimeter and dashed lines (- -) convex perimeter. Adapted from Metz et al. (1981) and Tucker et al. (1992).

2.3.2 Morphology and the correlation with physiological states and enzyme productivity

As seen, the morphology strongly influences the rheology of the fermentation broth and transport phenomena affecting fungal growth, therefore affecting the productivity (Van Suijdam e Metz, 1981; Hille et al., 2005). Apart from the correlation with broth rheology, other publications on fungal morphology show the correlation of the morphology with physiological states[6] of the fungus or show that specific morphologies of *Penicillium crysogenum* relate to an increased production of penicillin (Vanhoutte et al., 1995; Paul et al., 1994). Here only a few relevant examples are presented on how morphometric data obtained by image analysis may help characterizing physiological states and enzyme productivity.

One of the first attempts to use image analysis to characterize physiological states are shown in the work of Packer et al. (1992). The image analysis workflow proposed by the authors involved the computation of the total, cytoplasmic and degenerated hyphal cell volumes and, consequently, the proportions of cytoplasmic and degenerated (with high degree of vacuolation) volumes. The authors suggested that these measurements could be used to better understand the physiological changes, product formation and other metabolic processes. Following their work, the work of Vanhoutte et al. (1995) is also a good example of how image analysis can provide relevant morphometric data to help characterize physiological states. In this work, the authors classified hyphae of the growing mycelium of *Penicillium crysogenum* into five groups based on their location (apical, distal, both regions), degree of vacuolization, respiratory activity and the number of nuclei. Their experimental approach to identifying these groups consisted in using two dyes and the acquisition of both monochrome images and coloured images (with Red, Green and Blue, RGB, channels). In addition to the identification of the different physiological

[6] a specific state in which the living organism, in our case a filamentous fungus, carries out their chemical and physical functions. In industrial biotechnology, we are interested in identifying physiological states that increase the production of the products of interest, e.g. hydrolytic enymes

states based on these five groups, the author suggested that there could be a potential relationship between the existence of two groups and the increased production of penicillin.

Recently, Novy et al. (2016) proposed the use of CLSM and graphic user interface-aided (GUI-aided) manual tracing of the complex three-dimensional mycelium of *Trichoderma reesei* to measure cell compartment lengths and widths in different culture conditions. The authors were interested in the production of cellulotytic enzymes by *Trichoderma reesei* growing on lignocellulosic feedstocks. Thus, these morphometric measurements were evaluated in combination with results of the cellulase activity of the cultivation. It was suggested that the morphology affects cellulase activity and indicate that this approach was useful to analyse and optimize cultivations of *T. reesei* on lignocellulosic feedstocks. Since this study was one of the few that used 3D images of CLSM, more details and discussion about this work is available on section 2.4.2.

Still in the domain of sumberged fermentation, a relevant study on the relationship between pellet morphology and oxygen transport and availability within the pellet was conducted by Hille et al. (2005). The authors used 3D images obtained CLSM to analyse the biomass fraction profiles of *Aspergillus niger* as a function of the radius of the pellet, which is an indirect indication of the dense pellet or the so called disperse and "fluffy" morphology. Despite the fact that the images obtained for their research were 3D, the computations of biomass fraction was performed individually for each 2D image part of the stack (More details about this work are in the following section 2.4.2). They evaluated the biomass fraction profiles along with the oxygen concentration of the pellets also as a function of the radius of pellet radius. With such combination of image analysis and other experimental procedures do quantify the oxygen in the pellets, authors showed that the oxygen transport relates strongly with pellet morphology.

Some preliminary results have been published about the relationship between fungal morphology and enzyme production in SSC. Te Biesebeke et al. (2005) studied the growth of *Aspergillus oryzae* and observed that mutant strains with highly branched hyphae showed increased enzyme secretion. Similarly, other researchers studied the growth of *A. oryzae* in rice *koji* and observed that a higher acid protease and acid carboxypeptidase production occured when mycelia penetrated to a lower depth in the solid substrate (Ito et al., 1989). Another important consideration is that the morphology of the fungi in a bioreactor influences bed compactness: small portions of fermented solid and biomass may aggregate into big lumps due to interactions between aerial hyphae, affecting air flow and, consequently, mass and heat transfer throughout the bed (Schutyser, 2003).

2.3.3 Morphology data and fungal growth models

An approach to achieving a better understanding of the complex fungal morphology and the phenomena involved in fungal growth is the development of computational and mathematical models capable of describing how the fungus grows. Two different activities are associated with this approach: First, experiments that focus on obtaining quantitative morphological parameters or specific physical and biochemical phenomena involved in fungal growth and, second, the development of mathematical or computational models that describe fungal growth. Experiments provide insights regarding the growth as well as useful data for the validation of the models. On the other hand, the results of the models themselves will give different insights into how the fungi grow and indicate directions for future experiments. In general, the models seek to represent the growth of fungi in a realistic way, although some of them may focus on the morphology and others on the physical and biochemical phenomena involved in fungal growth (Coradin et al., 2011; Sugai-Guérios et al., 2016; Balmant et al., 2015). Further studies must attempt to develop

models that are capable of representing both the morphology and the physical and biochemical phenomena, because such a model would better describe the development of fungal mycelia in SSC (Sugai-Guérios et al., 2015).

One of the few works on solid-substrate cultivation that deserve attention is the one by Nopharatana et al. (2003). A strain of *Rhizopus oligosporus* was analysed during growth in artificial agar culture media and with different carbon sources using images obtained CLSM. Their goal was to obtain information on the volume occupied by biomass in space, as a function of the distance from the substrate surface. This way, the growth of both aerial and penetrative biomass could be studied similar to the laboratory experiments of Ito et al. (1989) and Te Biesebeke et al. (2005). The novelty in the work of Nopharatana et al. (2003) was the use of CLSM to extract quantitative information about the biomass distribution in space. This way, the results of the biomass profiles in different growth periods could be used as input to validate fungal growth models. Nopharatana (1999) developed a fungal growth model using equations to describe tip generation and growth to describe the collective behaviour of the mycelium.

Sugai-Guérios et al. (2016) present a more recent modelling work that used the morphometric data obtained by Nopharatana et al. (2003) of *Rhizopus oligosporus* as well as the data obtrained by Ito et al. (1989) on the growth of *Aspergillus oryzae* on rice grains. Their discrete model, named layer model, described the growth of penetrative hyphae in solid substrates by means of the biomass distribution as a function of the distance from the surface of the solid substrate. Their results indicate that there might be two different types of penetrative hypae and they suggested further investigations to confirm such suggestions.

Apart from the morphometric data already presented, spatial parameters such as tip growth angle frequency distributions and branching angle frequency distributions are also important when modelling fungal growth and studying more complex systems. Yang et al. (1992) intended to measure these variables and develop a model to simulate fungal growth and suggested that angle distribution measurements on the 2D dimensions could be extended to the 3D space. Thus, his calculation methodology and model would be relevant for an application on SSC systems, since the latter systems can be more complex in terms of different morphologies and directional preferences of hyphal growth. In addition, the authors were limited to the microscopy techniques that were available during that period, which imposed the calculation to be applied in less complex mycelia with fewer branches. An evaluation of a fungal culture on a solid substrate will require more powerful microscopy techniques but could adapt Yang et al. (1992) calculation methodology.

The discrete lattice-based model[7] of Coradin et al. (2011) deserves special attention, because it attempts to describe aerial hyphal structures and capture three-dimensional fungal growth behavior. The model represented aerial hyphae as biomass voxels and as growth iterations occurred over time, the hyphae occupied different spaces and grew in different directions with different probabilities. Unfortunately, the model was not fully capable of mimicking a real aerial mycelium and was validated based only with the results of Nopharatana et al. (2003), due to lack of additional data. The lack of quantitative morphological measurements in the area limited the development of a more detailed growth model. If a complete set of morphological parameters from table 2.2 were available, the growth rules of the model of Coradin et al. (2011) could be changed and the results could potentially better represent the real growing mycelium.

[7] A discrete lattice-based model is a fungal growth model that describes the space available for the growth of the fungus as three-dimensional array of cubes, which may be empty or occupied by a hyphal tip or a hyphal section behind the tip.

2.4 The current state of the literature on analysis of 3D morphology of filamentous fungi

2.4.1 The use of confocal laser scanning microscopy (CLSM)

The images used in the present work were acquired by a Confocal Laser Scanning Microscope, Model A1MP, Manufactured by Nikon Inc.. The microscope was provided by the Laboratory of Multi photon and Confocal Microscopy at the Federal University of Paraná, part of the Center for Advanced Fluorescence Techniques, supported by CAPES and FINEP (Financiadora de Estudos e Projetos). Figure 2.5

CLSM has a great advantage compared to wide-field microscopy, because it is capable of obtaining multiple images from different optical sections, in other words, xy planes in the z direction of the sample. In addition, CLSM provides an image with enhanced contrast and resolution for thick specimens, due to the image formation method, which excludes out-of-focus light (Claxton et al., 2006). With high resolution (pixels representing as much as a fraction of a micrometer), high contrast (images with reduced blur due to the reduction of out-of-focus light) images and fast computer processing capacity, samples of growing mycelia can be obtained as 2D image stacks, and may transformed into 3D or 4D object representations of the sample (4D, with time t being the fourth dimension). This allows the morphology of filamentous fungi to be studied with fewer limitations compared to individual 2D images obtained by conventional wide-field fluorescence microscopy. With CLSM images, even a full 3D reconstruction by computational models is possible. The microscope is very versatile, thus it can provide a wide range of configurations for different applications. However, there is a trade-off between the size of the field of view and the chosen resolution, so this relationship controls the microscope ability to acquire images per time unit (i.e. if the image has a high quality and a wide field of view, image acquisition may take so long that it is no longer possible to obtain more than an image every few minutes).

2.4.2 The limits of the literature

We have shown that there are many studies that obtained morphometric data of the fungal growth on submerged fermentation. However, the litetature lacks morphometric data of the growth of fungi on solid substrates. In addition, there are not many works that proposed methods to quantify the complex mycelial morphology using 3D images, specially using CLSM. In this section we discuss further the limitations of the literature with respect to the interest of the present work, which involves the understanding of the complex morphology and growth of filamentous fungi on solid substrates using 3D images.

The 3D image from CLSM may be processed and analysed in different ways: (1) each 2D image of the 2D stack may be analysed individually (2) the images can be merged into a single projection image (commonly a maximum intensity projection, MIP[8], of all images) or (3) the 3D image may be treated as a 3D volume and the complete xyz pixels, now voxels (volume elements) are used in the image processing workflow. Given the fact that future works should seek a better 3D representation of the mycelial distribution, approach (3), the use of the complete 2D stack is the preferred approach. Based on these different ways of analysing the images, Hille et al. (2005) used each 2D image of the stack for their analysis (1) and the work of Novy et al.

[8]A maximum intensity projection of a 3D image is a 2D image of the same size of the xy dimensions of the original 3D images, whose pixel values in position (i, j) are defined as the maximum pixel value existing in any of the z slices in the same $(i.j)$ position

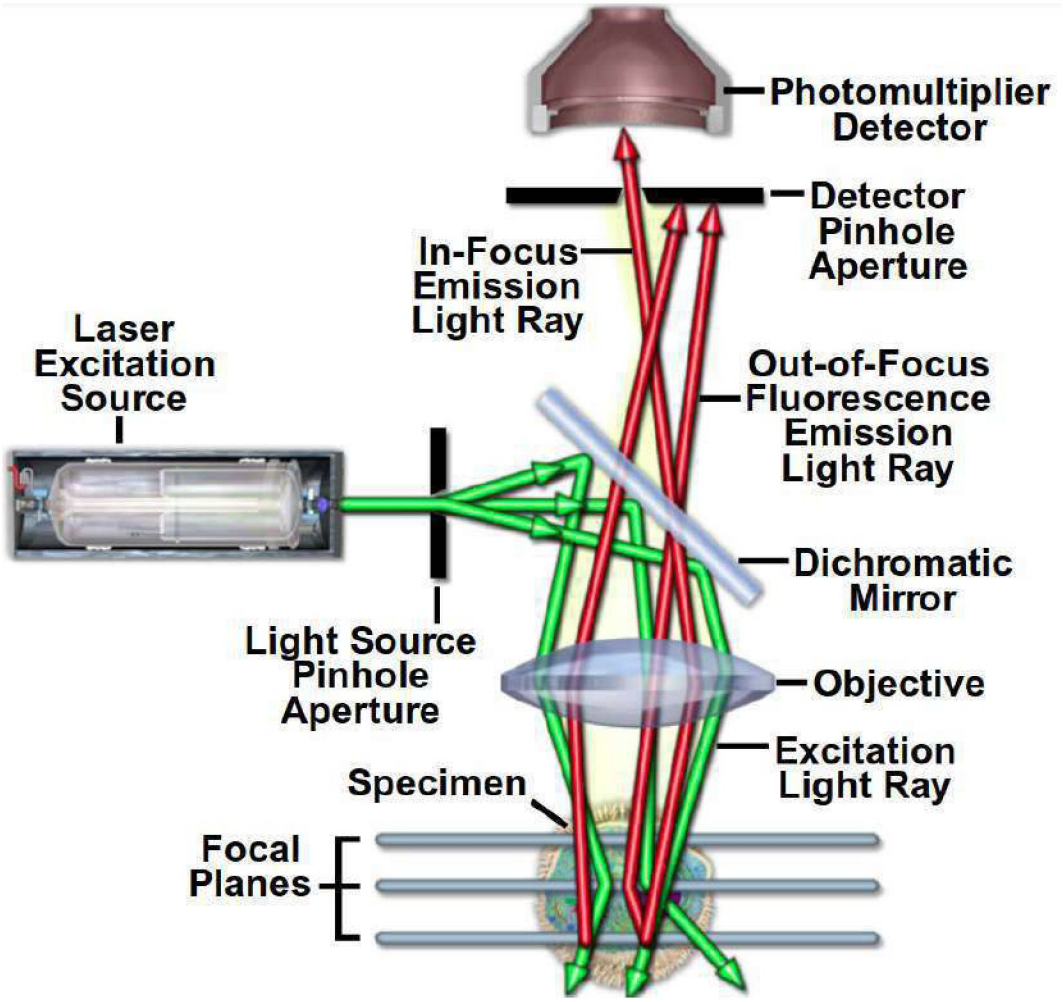

Figure 2.5: Principal light pathways in a basic confocal microscope configuration. Source: Paddock et al. (2018)

(2016) used the complete set of images and created a simple 3D model of the mycelial network (3). In contrast, the work of Nopharatana et al. (2003) used a single 2D image (2), obtained as a projection of the pixel with maximum intensity of from the stack.

These works also differ on the application of the study. Two of the studies were applied to SmF (Hille et al., 2005; Novy et al., 2016) and one was in SSC (Nopharatana et al., 2003). As a result, the way parameters are calculated were distinct. Hille et al. (2005) measured the volume fraction of biomass in pellet-shape mycelia as a function of the radial distance from the center of the pellet. As opposed to this radial biomass volume fraction profiles in a pellet, Nopharatana et al. (2003) determined the biomass volume fraction in the system as a function of depth and height from the substrate surface. Despite the similarity in the variables, a critical difference arises from the type of image used for the calculation. Nopharatana et al. (2003) applied an equation in order to take into account the spatial distribution of the hyphae in the planes not represented in the maximum intensity projection image (xz and yz, see equation 2.1),

$$\varphi = \frac{\pi^2 T}{8D} ln(1 - F) \tag{2.1}$$

where T is the diameter of the hyphae, D is the axial depth of the image (z axis of the original images), F is the area fraction occupied by biomass in the MIP image and φ is the biomass concentration in mg dry weight/cm^3. On the other hand, using all stacks of the 3D

Table 2.1: Studies that obtained quantitative morphological parameters of filamentous fungi from CLSM images

Authors	**Application**	**Image type**	**Morphological parameters**	**Goal**	**Software**
Hille et al. (2005)	SmF *Aspergillus niger*	2D image stack	Biomass volume fraction as a function of pellet radius	Relate morphology with O_2 diffusion	ImageJ with implemented macro
Novy et al. (2016)	SmF *Trichoderma reesei*	2D image stack	Cellular compartment length, cellular compartment width and branches per compartment	Relate morphology with the production of enzymes	Matlab®
Nopharatana *et al.* (2003)	SSF *Rhizopus oligosporus*	single 2D MIP image	Biomass concentration as a function of the distance from the solid surface	Study aerial and penetrative hyphae, validade model	ImageJ

image, Hille et al. (2005) computed each voxel occupied by biomass to determine the volume fraction occupied by biomass. Distinctively, Novy et al. (2016) calculated the length and width of the cell compartments composing the mycelium as well as the average number of branches per cell compartment.

These measurements (cell compartment length, width and average number of branches per cell compartment), even showing slight differences in the definition (please see table 2.2 for clarification) from other authors, were widely studied and calculated by researchers and in many different cases, mostly being applied to conditions of SmF, and are notably the most used parameters (Barry, 2010), either to find a relationship between morphology and other process variables or for the development of fungal growth models. With respect to biomass concentration or volume fraction profiles, despite being less explored, some authors used the experimental results of biomass profiles to validate their models (Coradin et al., 2011; Sugai-Guérios et al., 2016). The issue with these studies is that the information obtained is still insuficient: when one determines only length, number of branches and width, other determines the biomass fraction profiles. We judge this to be insufficient because for the specific case of the use of morphometric data to models, more parameters should be required.

A final aspect to be pointed out is related to the image analysis methods and software packages used to implement the morphological calculations. The two software packages used by the authors in Table 2.1 to calculate the morphological parameters were Matlab® The MathWorks Inc. (2015) and ImageJ Schneider et al. (2012). In Matlab, there are two toolboxes developed specially for image processing and computer vision operations, and ImageJ is open-source and has a wide range of functions and plug-ins for different applications. Two works used ImageJ, though Hille et al. (2005) implemented a macro to perform automatic calculations after the image was loaded into the software and Nopharatana et al. (2003) performed the calculations manually with the aid of the available functions and plug-ins. In the case of Novy et al. (2016), the authors implemented a program in Matlab that automatically calculated their variables (cell compartment length, width and average number of branches per cell compartment) and then displayed a simple ball-and-stick model of the mycelium. The balls represented septa and the sticks the length of the cell compartment. Unfortunately, the algorithm implementation proposed by Novy et al. (2016) depended heavily on the user, who was required to define the cell compartments based on the position of two subsequent hyphal septa.

Along with the morphological parameters obtained by authors from Table 2.1, additional parameters may be useful for the development of new fungal growth models or the improvement of exsiting models. The variables presented in table 2.2 were calculated in previous studies on submerged fermentation (excluding Riquelme et al. (1998), whose work studied the fungus growing on agar culture media). Note that measurements of hyphal extension rate, branching angle and tip growth angle, which were calculated by (Yang et al., 1992) and are not morphometric parameters but growth dynamics parameters, were used to develop a growth model capable of predicting the development of a single spore into a pellet in SmF. The authors suggest that the model could be adapted to describe hyphal growth on the surface of a solid, but no such model has been developed yet, though other models were published to describe growth in SSF (Coradin et al., 2011; Sugai-Guérios et al., 2016).

The availability of quantitative morphological data of the growth of filamentous fungi cultivated on solid substrates will contribute to: (a) the investigation of the relationship between morphology and the production of metabolites of interest, (b) the analysis of the effects of morphology on micro and macro transport phenomena related to fungal growt, (c) the study of hyphal differentiation and physiology and finally (d) the improvement and development of computational and mathematical models that simulate fungal growth. Furthermore, the current

Table 2.2: Relevant morphological parameters of filamentous fungi

Variable	Unit	Description	References
Total length	μm	total mycelial length	1, 2, 3, 4
Branch length*	μm	length of a single branch	1, 2, 3, 4
Segment length*	μm	length of the section of a hypha between two subsequent branch points	1
Cellular compartment length*	μm	length of a section of the hypha between two septa	8
Width or Diameter*	μm	average diameter of the hyphae	1, 4, 8
Number of tips	-	number of growing tips	1, 3, 4, 8
Hyphal Growth Unit (HGU)	μm	total length divided by number of tips	1, 3, 4
Hyphal extension rate*	$\mu m.min^{-1}$	extension rate of an hypha	5, 7
Branching rate*	$branch.min^{-1}$	branching rate of an hypha	7
Hyphal tendency to meander*	-	width of a minimum box surrounding the hypha over hypal diameter	6
Branching Angle*	degrees	Angle from which a new branch grows	5
Tip growth angle*	degrees	Angle from which a new section of hypha (of fixed length) grows	5

* apart from the total length, number of tips and HGU, all the variables may be calculated for individual hypha, as an average or even as a frequency distribution for the whole population of hypha. In addition, the parameters may be calculated separately for different regions of the mycelium (aerial, penetrative and surface hyphae).

1-Metz et al. (1981) 2-Adams e Thomas (1987)
3-Packer e Thomas (1990) 4-Tucker et al. (1992) 5-Yang et al. (1992)
6-Riquelme et al. (1998) 7-Reichl et al. (1990)
8-Novy et al. (2016)

research does not fully explore the potential of CLSM and other advanced microscopy techniques and existing image processing and analysis techniques. For example, Nopharatana et al. (2003) used a single 2D MIP image instead of the full 2D image stack, Hille et al. (2005) only determined the biomass volume fraction profiles in pellets and the method of Novy et al. (2016) was heavily dependent on the user. Also, these works only focused on a few morphological parameters.

2.5 Image analysis

In this section, some basic information about introductory theory of image processing and analysis theory are provided. Here, the reader will not find exhaustive and comprehensive information on such broad subject. However, Chapters 4 and 5 provide more details about image analysis specific to biofilament tracing methods. The books of Jähne (1997), Shapiro e Stockman (2001a),Gonzalez e Woods (2011), Jähne et al. (1999), Serra (1984) and also the course material

of Miura (2013) are recommended for more in-depth theory. This section of the dissertation was mainly inspired by Miura's course book and Gonzalez e Woods (2011).

Section 2.5.2 of this chapter provides additional information on pre-processing used in biofilament tracing methods. It may appear as out of place, however such information would not be required for the publication manuscript of Chapter 5 and is available in the current chapter.

2.5.1 Basic principles of image processing and analysis

What is a digital image?

A digital image consists of a matrix whose elements named pixels (picture element, *px*, or volume elements, voxels) contain a value (or values) that represents its brightness or intensity. When the image is represented visually, the value of each pixel are converted to a certain colour scale. A common greyscale image will have pixel colour intensities that range from black to while, with pixels with intensity values in between showing lighter or darker grey pixels. There are different types of images with respect to the colour model used, for example RGB (Red, Green and Blue), CMYK (Cyan, Magenta, Yellow and Key). The simplest and probably the most common type is the greyscale image, and the images used in the present work are all of this type. Figures 2.6 and 2.7 show examples of an image and its matrix representation.

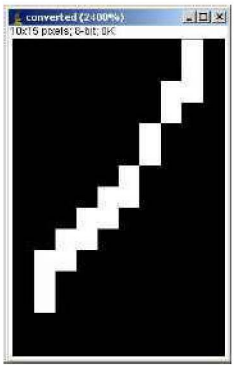

Figure 2.6: Example of a digital image. Source: Miura (2013).

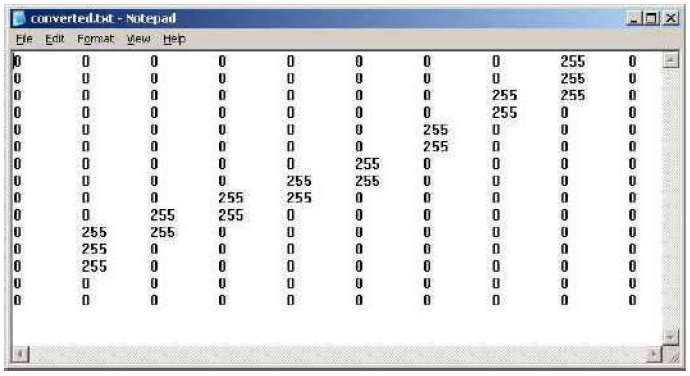

Figure 2.7: Example of matrix representation of the image from Figure 2.6. The white line in Figure 2.6 corresponds to non-zero numbers in the matrix. Source: Miura (2013).

Besides colour and pixel intensities, the image is also defined based on the bit depth. The bit depth defines how many different possible intensity values an image has. The higher the

bit depth, the more precise is the intensity scale of the image [9]. The smallest possible bit depth of an image is the bit depth of 1. Images of bit depth 1 are the binary images [10]. Then, the more common image bit depths are 8-bit, 12-bit and 16-bit, in which the intensity scales is divided into 256 (0 to 255), 4096 (0 to 4095) and 65556 (0 to 65535), respectively. In some cases, the 32-bit floating point bit depth is also used, which represent pixel intensity of the images with much greater range of intensity values because of the way the values are stored[11]. During this work, binary, 8-bit and 16-bit images were used.

One of the main interests of the research on fungal growth is the capability to observe their three-dimensional growth. Thus, 2D images are insufficient and 3D images are preferred. 3D images may be interpreted simply as a stack of 2D images. In some situations, in order to facilitate visualization, the information contained in the 3D image may be 'compressed' as a single image as a result of the projection along the z axis, known as projection. The most common projection is the maximum intensity projection, MIP, which only stores the maximum intensity value of the x, y pixel position along the z axis. See figure 2.8.

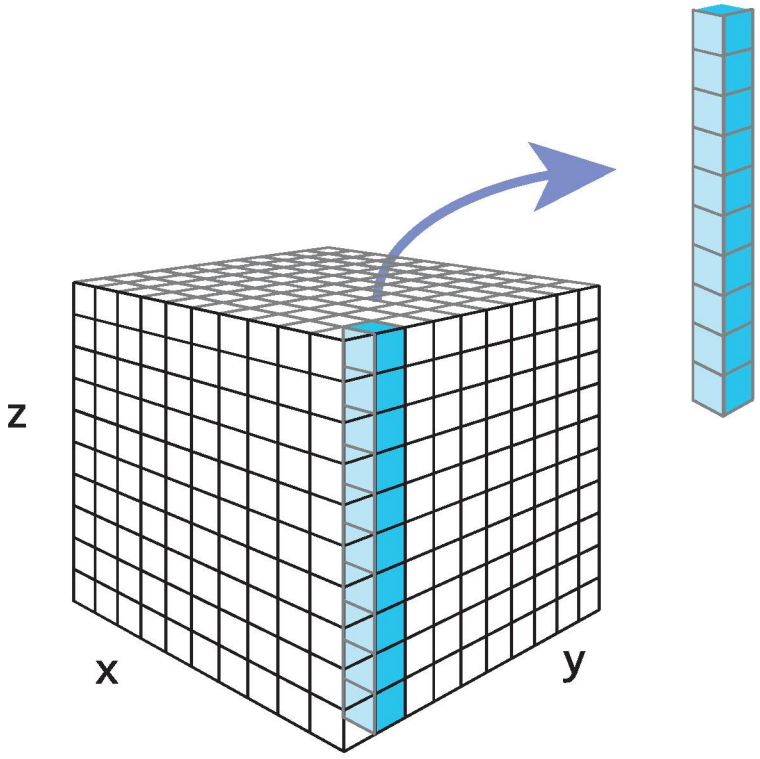

Figure 2.8: Representation of a 3D image, which is a three-dimensional matrix. A projection process would then use the pixels of all the x, y positions in the z axis to compute a single value (maximum, minimum, mean, etc) and show the projection image. Source: Miura (2013)

[9] However, bare in mind that the bit depth also defines how much memory is required to store the image in a computer. The higher the bit depth, the more memory for storage it requires

[10] Since the computer treats information with the binary number system, the amount of information to be stored is represented with base 2, as 2^n

[11] 32-bit floating point images utilize 1 bit to represent the sign S of the value, 23 bits to represent a fraction F and 8 bits to describe an exponent E. $pixelvalue = (-1)S.1.F.2.(E-127)$

2.5.2 An image analysis workflow

An image analysis workflow can be represented by the diagram presented Figure 2.9, but an important differentiation needs to be clarified. There are two different processes categories; Processes whose input and output are images and processes whose inputs are images but whose outputs are attributes extracted from those images Gonzalez e Woods (2011).

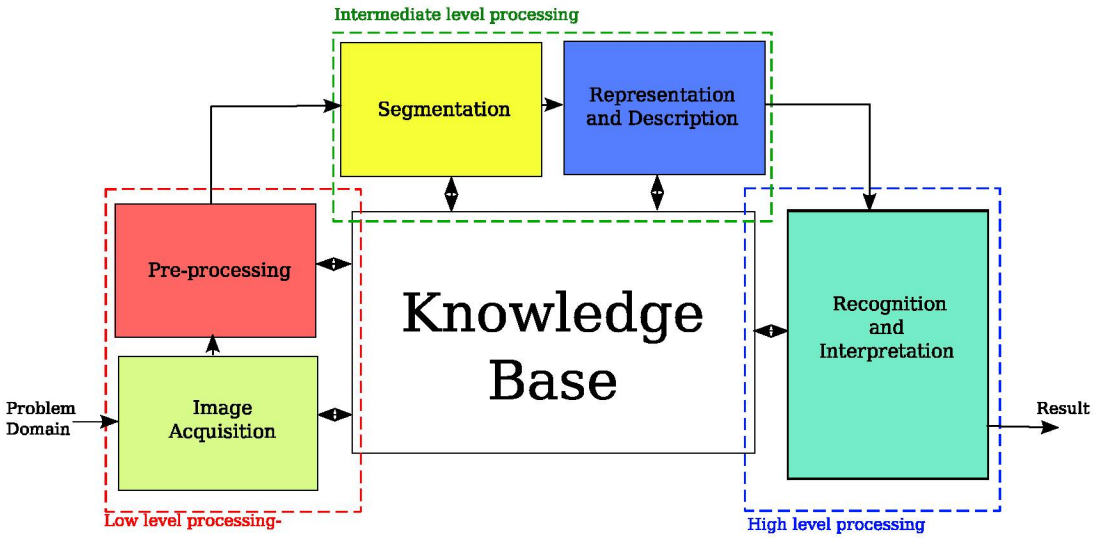

Figure 2.9: Block diagram representation of an image analysis workflow. Adapted from Gonzalez e Woods (2011)

Starting with the domain of the problem, it is necessary to define what is the objective of the workflow, what are the research questions to answer and what are the expected results that will help answer the research question and will be obtained by applying the workflow to the images.

The first step involved defining how the images will be acquired. The image acquisition step comprise of tasks such as choosing the imaging modality, the image properties (size, bit depth, colour model) and the number of images required. Following image acquisition is the pre-processing step. Pre-processing step involve mainly image operations to remove undesirable objects from the image or enhancing features of interest. Some authors prefer to name pre-processing as image enhancement or more specific terms. In any case, operations related to contrast enhancement, feature enhancement, image denoising and smoothing may be included as pre-processing. The output of these first steps are images, and may be classified as low level processing. Then, the third step is segmentation, which involves to partition the image in different segments in order to represent the image in a simpler way or in a way that makes further processing easier. In general, segmentation is arguably the most difficult task in image processing and is considered the core of a workflow. is one concept in the border of image processing (image as input and as output) and image analysis (image as input and other types of data as output). Segmentation is followed by Representation and description processes. In this step, the features of interest of the image are to be represented in a mathematical or computational way such that further operations are capable of obtaining the desired information from the image, for example, the nucleus of a cell (with an approximately circle shape) whose volume needs to be determined may be represented as a circle. Image description will attempt to extract attributes from the image that result in relevant quantitative information. In the case of the nucleus of the cell, a value of the radius of a circle may be assigned. These two latter processes can be classified as intermediate level processing and most commonly have data other than images as

outputs. Finally, Recognition and interpretation steps will finalize image analysis and provide the final desired outputs. Recognition process will assign labels and classify the image based on the desired descriptors and together with all the information previously obtained will allow its interpretation and finally provide a final result, which can be an action, mathematical parameters, a qualitative conclusion about the problem, etc.. In the center of Figure 2.9 the big white block represents a knowledge base, which is also part of the workflow. The knowledge base refers to previously obtained knowledge of the problem and it can be altered and improved as the image analysis system goes through its processes each time an image is analysed. The double-sided arrow refers to this bilateral relation, with which the process is improved and so as the knowledge base itself with new information obtained from each step.

More recently, the increase share of machine learning approaches on research on bioimage analysis has been causing several discussions on what is the general workflow that could include techniques such as pixel classification using deep neural networks. In some cases, researchers suggest that the general workflow could comprise of a pre-segmentation step and a classification step, which could use several different machine learning approaches. However, the present work will keep the classical definitions of the image analysis workflow.

Image enhanement methods

For the specific case of tracing of biological networks such as neurons, cytoskeletal structures and the mycelia of a filamentous fungus, the review presented in chapter 4 shows that there are four most common image enhancement techniques, also known as pre-processing techniques by some researchers, to improve image quality of the tracing results. These pre-processing techniques are: Filament enhancement (also known as vessel enhancement), background subtraction, smoothing and deconvolution (often applied to confocal images). The technique of image intensity normalization was included in a smaller number of filament tracing workflows but was also useful.

Filament enhancement techniques, of course, enhance the specific area of interest: the filaments themselves. The methods of Frangi et al. (1998) and Sato et al. (1998) are the most widely used of this group, although there is still a lot of research related to improvement of filament enhancement methods and there are many other options available (Law e Chung, 2008; Wilkinson e Westenberg, 2001; Krissian et al., 1997). Filament enhancement methods rely on information about the gradients of the image, in other words, the rates of change of the intensity of the pixels related to certain directions. The gradients may be considered in the method through different calculations. For example, some techniques use anisotropic diffusion equations and calculate second order derivatives of the image of the directions orthogonal to the image gradient of intensity, while others evaluate gradients by analysing the eigenvalues of the Hessian matrix of the voxels in the image in order to compute the likelihood of a vessel being present (Krissian et al., 1997; Frangi et al., 1998; Sato et al., 1998). The end result of the filament enhancement image is an image which shows regions of reduced intensity where there are no filament-like structures and regions of conserved intensity where there are filament-like structures. However, some of these methods fail to maintain image intensity where filaments cross, usually referred to as branching points, especially in the case of Frangi et al. (1998) and Sato et al. (1998).

Background subtraction involves the estimation of the background intensity of the image at every pixel and obtaining an image of the estimated background, which is subtracted from the original. There are different ways of obtaining the estimated background image, and one of them, used for uneven background correction, is the rolling ball radius approach: each pixel background intensity is estimated processing the image using morphological opening operation with a ball structuring element (Sternberg, 1983).

One of the most widely used pre-processing techniques is image smoothing. Smoothing involves simpler operations compared to filament enhancement. The image is convolved with specific filters that reduce the differences in intensity of neighbouring pixels. Median filter is commonly used as a smoothing filter in biological filaments as it reduces noise in the image while conserving edges. On the other hand, Gaussian smoothing is used as well, although it has a stronger impact on edges compared to the median filter. Another generally applied technique is image intensity normalization, which can be used in cases where the image shows low foreground pixel intensities or maximum pixel intensities are lower than the image bit depth (for example, the maximum intensity of the foreground pixels of an 8-bit is 100, whereas the maximum possible intensity is 255). Normalization is nothing but a linear stretch of the image intensities. Because of that, besides increasing intensity of the desired foreground pixels, normalization also increases the intensity of noise and it may result in images of poorer quality.

Image deconvolution is the last technique to be described. Such technique is based on the principles of light diffraction and the microscopy limitations which causes the pixel intensities of the acquired image to be influenced by out-of-focus light. To minimize image blurring caused by these physical limitations, the point spread function (PSF) is obtained. It is a function that represents the light diffraction pattern of a point source of light using the same microscope and lens configurations used to obtain the image. With the PSF, the image quality is improved by performing deconvolution. This name comes from the fact that the image of the sample is acquired by convolving the image of the object with the PSF. There are two main types of image deconvolution: Conventional and blind deconvolution. The first is performed when the PSF of the imaging equipment is known and obtained experimentally, whereas blind deconvolution is applied when the real PSF of the equipment is not known, therefore it is estimated. Deconvolution is probably the technique that would yield the best image quality improvements with respect to noise, increase in resolution and contrast (Cannell et al., 2006), although it is a computationally expensive technique. For this reason it may not be feasible in big images or big datasets of images and in cases where real-time enhancement is required.

There are many different options of equations that estimate the PSF and perform deconvolution. More details can be found in the works of Sage et al. (2017); Kirshner et al. (2013).

2.5.3 Basics of benchmarking

In this section, a brief description of benchmarking is provided as well as additional details into image quality parameters, biofilament tracing metrics and ground truth and synthetic images.

How to verify the quality of the solution?

The results of any quantitative methods, including image processing and analysis methods, must meet certain quality levels so they can be used in research. There are many ways to verify the quality of the solution of an image analysis component or the solution of a complete workflow. Researchers in image analysis commonly use the term *benchmarking* to refer to the process of analysing, comparing the results of image analysis methods and identifying the best methods based on defined metrics. In case the solution of the method to compare has an image as output and improvements in image quality are desired, it is possible to use general image quality parameters as metrics, such as the structural similarity index and the signal-to-noise ratio. Other common option is the use of the receiver operating characteristic curve (ROC curve) and computation of the true positive rate, true negative rate, false positive rate and false negative rate. Using the ROC curve and these metrics is possible when there is a gold standard, also known as

a ground truth result, which is considered the correct result of the method. An example case of the use of ROC curve is to compare the segmentation results, where there is a binary image as output and another binary image as ground truth. Many other ways to perform benchmarking exist. For example, one of the simplest ways though not quantitative is comparing methods by qualitative observation of the tracing results. For each specific case, such as the one of our interest (biofilament tracing methods that output a graph representation of the filaments in the image), more specialized metrics were developed.

General image quality parameters

For many decades the image processing community has used mainly two parameters to assess image quality, namely the mean squared error, or MSE, and the signal-to-noise ratio, SNR. The MSE is of simple computation and its calculation is based in the sum of the squares of the differences between the pixels of an image and a reference image. In contrast, SNR requires a reference image and is computed as the sum of the squared intensities of the pixels divided by the MSE.

An issue perceived with the MSE is that its value does not always reflect in better or worse perceived image quality, for it does not account for structural information and imply a series of assumptions about the image signal when used, but these assumptions are not always true for images, for example the assumption that pixel intensity of all pixels is equally important. The main point is: there might by images of quite distinct quality that show similar or even same MSE, making it insufficient to measure perceived image quality. A good discussion about the pros and cons of using the MSE can be found in the work of Wang e Bovik (2009). Unlike the MSE, the SNR (not the peak signal-to-noise ratio, PSNR) is more useful because it carries information regarding the magnitude of the signal compared to the magnitude of the noise present in the image. In addition, the presence and magnitude of different categories of noises relates to the configuration of the microscopy equipment used to acquire the images. In confocal microscopy, the pinhole size affects the SNR, as well as type of detector and scan rate. (Sheppard et al., 2006, 1992).

There is another group of image quality parameters based on properties of the human visual system (HVS). The structural similarity index (SSIM) is one that received special attention in the past years (Wang et al., 2004). The principle of the SSIM is based in the assumption that the human visual system is highly adapted to extract structural information of objects, therefore the SSIM considers that a degraded image results from perceived changes in structural information of the objects in the image. The SSIM calculation framework is based on three components: luminance, contrast and structure, as equation 2.2 depicts,

$$SSIM(x,y) = [l(x,y)]^{\alpha} \cdot [c(x,y)]^{\beta} \cdot [s(x,y)]^{\gamma} \tag{2.2}$$

where $l(x,y)$, $c(x,y)$ and $s(x,y)$ are the luminance, contrast and structure functions, respectively. $\alpha > 0$, $\beta > 0$ and $\gamma > 0$ are parameters to adjust the importance of each component.

In this work, we will use both the SNR and the SSIM to evaluate the effect of the image enhancement techniques on image quality.

Biofilament tracing metrics

Among the benchmarking alternatives is the use of metrics that are especially tailored for one's research purposes. In neuron research, the DIADEM metric has been proposed in order to assess the quality of biofilament tracing methods (Gillette et al., 2011). The DIADEM metric works with the final tracing results of a neuron, which is defined as a tree-like structure. The result

is a graph representation of the neuron, usually in the swc file format. The .swc file format is a node list and it has 7 data items describing each node: node id or node number, structure identifier (created to classify neurons), x, y and z spatial positions, radius, and parent node. The intention with the DIADEM metric was to provide a quality measurement that focused on the tree structure and compared a tracing result against a gold standard node by node or branch by branch. The DIADEM metric produces a single similarity value (from 0 to 1) and was based on matching branch points and end-points and the topology between two tracings and has been widely used. Although there were existing and standard metrics such as the tree edit distance (TED), the authors of the DIADEM metric state that such metric is not spatially specific and in the specific need to understand neuronal morphology and topology, such measurements are not suitable. Thus, this is probably the reason for its success and wide use.

Another proposed metric is Netmets (Mayerich et al., 2012). Netmets was proposed to be useful for the more general benchmarking framework of biological networks, which include both tree-like structures and closed-loop networks. NetMets takes into account the geometry and the connectivity of the tracing results and provides four normalized values that represent the degree of similarity between two tracing results, two for geometry and two for connectivity. The metric calculations also use as input an .swc file of the tracing results as well as the closed-loop models with Alias/Wavefront .obj file format as input. The geometry metrics quantifies the quality of the tracing as a ratio of the length of filaments in the first tracing that do not exist in the second tracing and the total length of fibres in the first tracing, whereas the connectivity metric quantifies the quality of the tracing based on the rate of false positives and false negatives using concepts related to the problem of graph isomorphism.

The use of metrics to evaluate and compare biofilament tracing methods is critical to support the improvement of existing methods and the development of more robust and generalized biofilament tracing methods.

On ground truth datasets and synthetic images

An important step in the benchmarking process is the acquisition of ground truth datasets or the definition and creation of synthetic image datasets. The ground truth datasets in biofilament tracing methods are usually images annotated by specialists in imaging or the study of the object of interest. These annotations usually have the same format as the output of a biofilament tracing method or is provided in such a way that conversion to the appropriate format is possible. Such step in benchmarking may be considered a bottleneck given that, in recent years, datasets are getting larger and the complexity of the biofilaments to be traced may as well hinder the process of manual tracing (Mayerich et al., 2012). However, in order to perform detailed benchmarking, these ground truth datasets are essential. In addition to their utility in benchmarking, some recent biofilament tracing methods that include a machine learning approaches may required part of the ground truth datasets for their learning step.

An alternative to the use of ground truth datasets created by human specialists is the use of synthetic images. With synthetic images, the results are known when the image is generated, which makes it possible for use in benchmarking. An example of synthetic image generation algorithm is VascuSynth, proposed by Hamarneh e Jassi (2010). The authors propose a method to simulate volumetric images of a tree-like biofilament structure and generate their ground-truths, location of branch points, branch properties and tree hierarchy. VascuSynth has been used recently with success by (Wang et al., 2011; Sazak et al., 2018). Their tree generation algorithm is based on blood vessel theory and require data such as the initial and final blood pressure, the blood flow through the vessels an the oxygen requirements for regions in the simulated volume. Another tool is the TREES toolbox, proposed in the work of Cuntz et al. (2011). Their tree

generation simulates neuronal cells and uses an extended minimum spanning tree algorithm followed by resampling the tree, tree smoothing, spine insertion and rendering for visualization.

Despite the advantages of the use of synthetic images, it may not be considered a reliable benchmarking tool, since it may be difficult to process the image in such a way it has the same quality (noise, contrast, etc) a real image would have. However it is accepted as a proof of concept in many situations. Recent benchmarking efforts in other areas, for example single particle and cell tracking, proposed the use of both synthetic and real image datasets (Chenouard et al., 2014; Maška et al., 2014).

3 Objectives and strategic plan

3.1 Objectives

The literature lacks quantitative morphological and growth dynamics data of the complex three-dimensional growth of filamentous fungi in solid substrates. However, microscopy techniques and the use of image analysis are sufficiently advanced to allow the acquisition of such data. In Chapter 2, we noted that the research field of the growth of filamentous fungi on solid-state still has not fully explored the capabilities of the filament tracing methods from images.

Given the current state of the knowledge in biofilament tracing methods for images of filamentous fungi, the main objective of this research project is to evaluate potential biofilament tracing methods for three-dimensional images that could provide sufficiently accurate and reliable results to the images obtained by our research group and analyse whether there are any possible improvements in the image acquisition procedures in order to increase the quality of the biofilament tracing results.

Specific objectives were drawn to help achieve our main objective:

- Understand the literature of biofilament tracing methods and perform an extensive literature analysis of the existing biofilament tracing methods in other research areas (Presented in Chapter 4) .
- Evaluation of the image enhancement operations found in the first step (literature analysis) to increase image quality prior to the execution of the biofilament tracing methods (Presented in Chapter 5).
- Evaluation of the different biofilament tracing methods found in the literature and definition of the method to be used further to extract a representation of the mycelial network from the images acquired by our research group (Presented in Chapter 5).
- Discussion potential improvements in the image acquisition step and further improvements in benchmarking and evaluating the biofilament tracing methods (Presented in Chapter 5 and 6).

3.2 Stages of the project and structure of this dissertation

The images obtained during the doctoral studies of Sugai-Guérios (2016) will be used (More details are available in section 5). The fungus used in this project was a fluorescent strain of *Aspergillus niger* ATCC 1015 (CBS 113.46). Since the images were already available, this project did not involve the acquisition of new images, hence the focus was on evaluating the images and in the image processing and analysis step.

In order to achieve the defined objectives, the project involved three main stages:

- Literature analysis of biofilament tracing methods in other areas of biology (neurons, blood vessels, plant roots, cytoskeletal structures, among others).
- Testing and an analysis of image enhancement and biofilament tracing methods found in the previous stage.
- Calculation of morphometric and growth dynamics data of the growth of *A. niger* and evaluation of the results.

The structure of this document comprises 7 chapters, with the main chapters described below:

Chapter 4 presents a thorough review of biofilament tracing methods existing in the literature, which involves the definition of a classification methodology and the use of basic graph theory to analyse the selected literature. In the review, many areas of biology related to research on biofilaments were covered. A list of available software implementations was created and the chapter provides a discussion of the main features these biofilament tracing methods have in common, for example with respect to the theoretical approach used and the user interaction required by the method. In addition, important issues to be managed by the bioimage analysis community are pointed out, such as the construction of a database of ground truth datasets.

Chapter 5 presents the evaluation of a number of image enhancement methods and biofilament tracing methods that were applied to our images. After the evaluation, we selected the most appropriate image enhancement method, based on image quality parameters, and the best biofilament tracing method, based on a qualitative visualization of the tracing results. Following the selection of the image enhancement and biofilament tracing methods, we obtained the tracing results of two of our datasets of time-lapsed 3D images to compute some of the most common fungal morphometric and growth dynamics data.

Chapter 6 revisits the main contributions of this project to the scientific community and its limitations and also provides ideas of further research opportunities.

4 Unveiling the past and future of image analysis methods applied to biological filaments

This chapter comprises a thorough analysis of the existing methods for tracing biological filament structures from images. This section is a first draft of an article that could be submitted to a journal that has in its scope biological image analysis.

4.1 Summary

In the area of bioimage analysis, the number of options of biofilament tracing methods has grown considerably in the last decade. Because of that, the task of analysing such great amount of publications that propose biofilament tracing methods has proven to be a challenge. Now, it is becoming more difficult for users of image analysis methods and image analysts to cope with the huge variety of algorithms and various options of implementations available. In addition, many new researchers (life scientists, engineers and computer scientists) are entering this highly interdisciplinary area. Thus, there is a need to use common vocabularies and to improve knowledge communication between the different groups using biofilament tracing methods. In the present work, we perform a thorough analysis of a selection of 87 biofilament tracing publications, with a focus on 3D images and confocal microscopy techniques. For the analysis, we propose a classification methodology and an analysis approach that may later be explored by researchers through crowdsourced databases of image analysis methods, ontologies and graph analysis.

4.2 Introduction

When picturing biological filament networks, researchers with different backgrounds may imagine quite distinct examples: from plant roots and pulmonary airways to cytoskeletal structures. Researchers from the areas related to many of the cited examples (plant physiology, neurosciences, industrial biotechnology, computer-aided medical diagnosis and others) are often interested in the morphology and topology of their complex filament networks and structures. Image processing and analysis techniques are probably the most common way of obtaining more quantitative information about such complex structures.

There is a vast number of publications that discuss image analysis methods capable of identifying, extracting and representing biological filament networks from images, henceforth known as biofilament tracing. Unfortunately, a great number of these methods stay within their own research fields, so users and developers from other fields may have difficulty in finding

or even using them. This happens for many reasons, but mostly because the majority of such methods is thought to be suitable only for specific filament types, imaging techniques, and certain image quality parameters. Another possible reason is the fact that there are research fields which are more familiar with the use of image analysis than others, while other fields have not yet explored image analysis or researchers do not know its potential to boost their research. In the present work, we present the first ever attempt to integrate the literature of biofilament tracing from different fields.

There are literature reviews available for specific biofilament tracing cases, such as blood vessels (Kirbas e Quek, 2003; Lesage et al., 2009) and neurons (Donohue e Ascoli, 2011; Meijering, 2010), but the literature lacks a more general review and discussion on biofilament tracing methods. Therefore, our goal with this work is to provide relevant information about image analysis methods for biological filament networks, more specifically, for intermediate and advanced users that wish to improve their knowledge of the theory behind the many different options of biofilament tracing methods and the practical side of the methods, e.g. the available implementations. By expanding the analysis of literature, we wish to minimize potential rework by researchers and increase the knowledge exchange and contributions in the community of biological filament networks.

In order to achieve our goal, we perform a thorough analysis of the biofilament tracing literature, with a focus on 3D images and confocal microscopy techniques. First, we discuss the general image analysis workflow, which is common to the majority of the image analysis methods. Then, we describe our proposed classification method based on previous publications to aid in our analysis. We then describe how the selection of publications was done and discuss the most common features of the biofilament tracing methods. In our classification, three are the key features: (i) the description of the image enhancement (or pre-processing) step, the theoretical approach of the tracing step, and the type of user interaction the method requires. In addition, we provide a detailed list of software packages, libraries, and plug-ins available for use, with a focus on open-source and free alternatives. Finally, we go further and identify combinations of methods and features used by groups of publications/methods through graph visualization and analysis.

4.3 How image processing is used to identify and trace biological filaments?

4.3.1 General workflow and concepts of an image analysis system

Prior to discussing the details regarding the image analysis methods and our analysis of the literature, we describe basic concepts of image analysis and the major steps involved in an image processing and analysis system Gonzalez e Woods (2011) or workflow Miura (2016). The image analysis system or workflow is the framework with which a specific problem can be solved with the use of images, for example, the task may be to compute the total length of a filament network from light microscopy images or calculate the total number of the branch points and end points of the same filament network. Such workflow can be separated into five main steps: (i) image enhancement (or pre-processing), (ii) segmentation or object identification, (ii) representation or object extraction, (iv) post-processing, and (v) data analysis or interpretation. After the image is acquired (we do not discuss this step of the process in our work), the image analysis system receives an image as input and is constructed so that it outputs the desired results (in the form of numerical parameters, plots or other visualizations), or data that can be processed to compute the

desired results. In order to produce the results, there is a combination of components within each of these main steps, which comprise of specific image processing algorithms or data processing tasks. These components are the building blocks of the image analysis system and will be put together in an appropriate way so, in the end, it outputs the results with the desired accuracy, precision, processing time and amount of user interaction. Figure 4.1 shows a block diagram that describes a general image analysis system.

The first step after image acquisition is image enhancement, also known as image pre-processing. Often the biological images to be analysed will contain undesired features such as noise, artefacts, uneven illumination, and inhomogeneous intensity of the objects of interest. The presence and intensity of these undesired features depend highly on the imaging technique, the sample preparation and staining procedures, and the relationship between the size of the objects of interest and the resolution capabilities of the imaging technique. One would then choose the components of an enhancement step so they minimize or remove the undesired features, therefore improving image quality, which will consequently improve the results of the upcoming steps and potentially of the final result. The enhancement may be more or less important depending on the robustness and accuracy of the segmentation and representation steps. For example, enhancement may not be even necessary, because the further steps of a workflow may function properly and provide accurate results even if the image contains undesired features.

Following pre-processing is the segmentation step. In this step, the workflow will identify both the object of interest and the other regions in the image and separate them. Segmentation is the most critical step in the process since the result of the segmentation method affects greatly the accuracy and precision of the final results. For example, if the result of a segmentation step does not separate a spherical artefact from the filaments in the image, the further steps in the image analysis system may not account for that error and consider such spherical artefact as a filament. Furthermore, it can be difficult to choose or develop the appropriate segmentation component, because the appropriate segmentation component also depends on the results one wishes to obtain.

Image representation, also named object extraction, occurs after the image is segmented. The goal of the representation step is to extract the information of the object of interest from the image and represent it in a scientifically meaningful way so that it can be further processed or computed to obtain the desired results. In some cases, the representation step may be coupled with the segmentation step in a component. This occurs in cases where the theoretical fundamentals and the implementation of the algorithm of a component allow such combination. An example is template matching algorithm for biological filaments, where the result of the segmentation step already gives the information needed to build the representation of the object (Template matching algorithms will be discussed in section 4.3.2). The representation step receives an image as input and outputs other types of data, thus the representation step is different from the pre-processing and segmentation steps. The network of biofilaments is commonly represented as a graph, in which the filament network is defined as a collection of nodes and edges connecting these nodes. Topology is an inherent part of the graph representation. Each node in the graph representation has a parent node, therefore the graph shows the connectivity between two elements of the filament network. Additional information may also be present in the graph representation, for example, the radius of each node.

Post-processing takes place after representation step. A common case of post-processing in biological filaments is in skeleton-based methods. After the skeletonization process, branch connection and branch pruning steps are often added to the algorithm. With this post-processing, unconnected branches are connected and spurious branches can be deleted from the skeleton. The use of post-processing steps tries to improve the final result and yield increased accuracy, precision

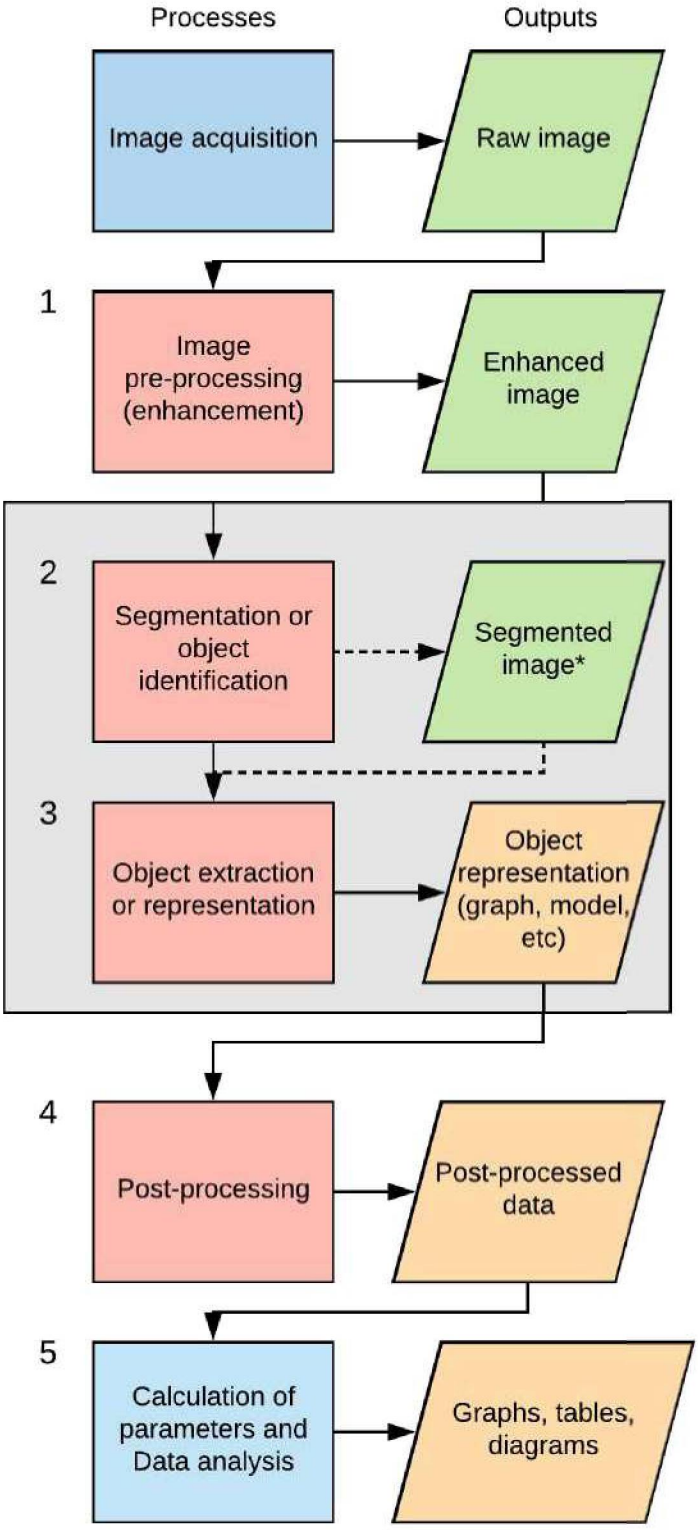

Figure 4.1: Block diagram representing an image analysis system or workflow. Steps 2 and 3 may be associated depending on the approach used. Note (*): commonly, a segmented image is a binarized image representing background and foreground (object of interest) but a segmented image may not be needed depending on the theoretical approach.

or reduce the processing time of the results. However, for a beginner user, an intermediate user or image analyst, it may be difficult to choose or develop a post-processing component, since

such post-processing steps often leave the domain of image analysis theory (image analysis components that have lower level of complexity) and require a solid background on mathematical methods, optimization, and programming.

The last step in the workflow of the image analysis system is the actual computation and analysis of the data. Results computation and analysis depends on many different aspects and in this work we will not discuss details about it. Note that the aspects such as the goal of the research, the type of output data, the type of the biological filament, the scale in which one wishes to analyse and the type of phenomena being studied affect the final data computation and analysis step.

4.3.2 Classification of image analysis methods in the literature

In the present work, we consider image analysis methods that, from an image of a biofilament network, are capable of obtaining a graph representation of this biofilament network. Such graph representation shall have nodes representing the main structure of the filaments (e.g. the centrelines or de medial axis of the filaments), with their spatial position and radius. In addition, the relationship with other nodes is represented by the edges between them in order to represent the correct topology of the biofilament network.

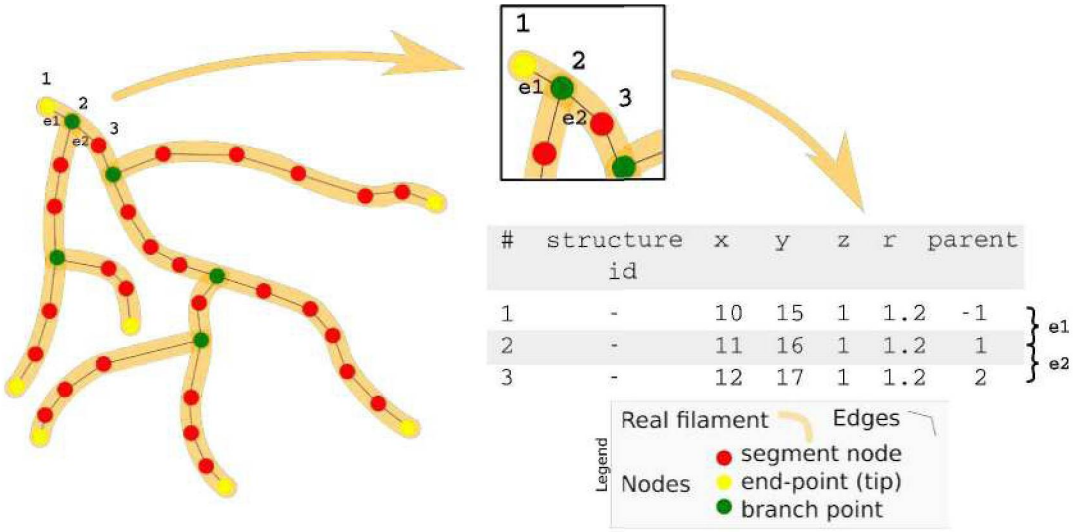

Figure 4.2: Schematic representation of the result of a filament tracing method. The nodes and edges of the tracing result should overlap with the position of the real filament.A small region with nodes (1,2 and 3) and edges (e1 and e2) identified shows how the example of the output .swc file format as a list of nodes that provide the node id, its position in the image (x, y and z coordinates), its radius (in px) and the parent node, which defines the edges between the nodes.

The classification we propose includes information that is potentially useful for all kinds of researchers interested in image analysis of biological filaments: from beginner and intermediate users of image analysis methods to bioimage analysts and developers of image analysis methods. Although this is true, our focus is to provide sufficient information for intermediate users and bioimage analysts so they can better understand the great variety of options out there and make better decisions of which tools to choose and build the workflow to solve their specific problems.

The task of classifying image analysis publications is a challenge. Classification can be really difficult and time-consuming since different areas of research that work with bioimage analysis (of which biology, biotechnology, and computer science are the major areas) may use different wording for image analysis techniques or the authors do not clearly define the

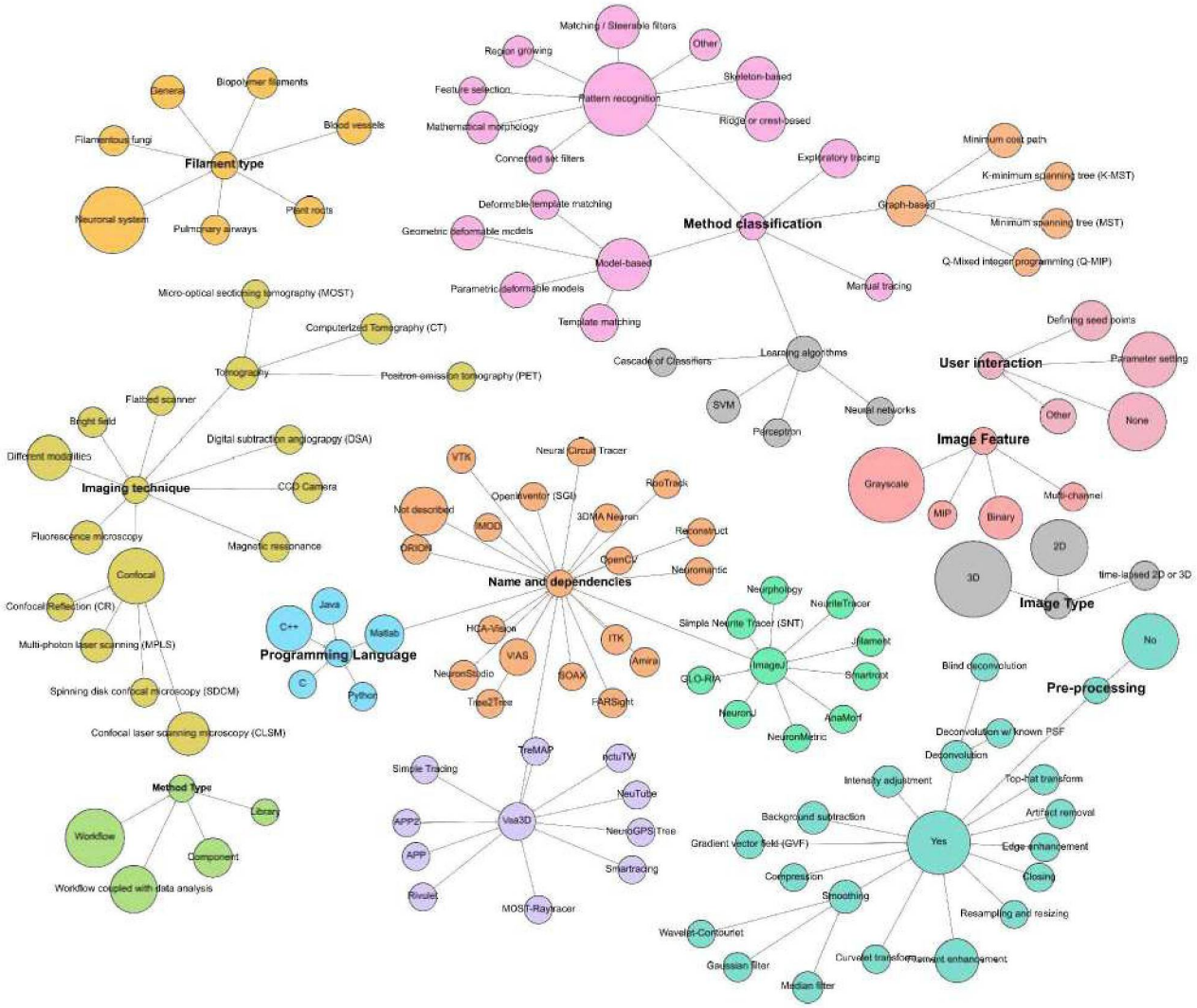

Figure 4.3: Graph representation of the classes of our proposed classification methodology. The ten main classes are: Method type gGreen), Filament type (yellow), Pre-processing (light green), Method classification (Pink, gray and light orange nodes), Image Type (Gray), Image feature (salmon), Imaging Technique (Dark yellow), Name and dependencies (light orange, light green), User interaction (mate pink) and Programming language (light blue).

classification of their methods on their work. Because classification is so difficult and to avoid complete rework, we considered two previously proposed classification methods as starting point of our work: The classification of Kirbas e Quek (2003) and Donohue e Ascoli (2011). We modified and adapted the classes as new techniques appeared since the publication of these reviews. In other situations, we changed the classes because it would make the analysis clearer and easier for the readers.

4.3.3 Description of the classification method

Our classification is divided into ten main categories as shown in Figure 4.3. We developed this classification to categorize what we call generally a method, which can be either an image analysis workflow, a component or a collection. Each category used to classify the methods will be discussed in the following sub-sections.

Filament type

The class *Filament type* was included to verify the research fields using filament tracing methods. We added simple terms such as *neuronal systems, blood vessels*, and *plant roots* as subclasses (see complete list in Figure 4.3). In addition, we considered a subclass called *General* for methods that were developed and tested for two or more different types of filaments.

Method type

The type of method is a class that defines whether the method is a component, a workflow (see section 4.3.1 for more details) or a library. A component comprises one or more image processing operations that alone would not yield the final graph representation of the biofilament network. An example of a component is a filament enhancement algorithm or a morphological thinning operation on a binary image. Components are used as part of a workflow, therefore they usually require the use of other components to provide the final tracing result. On the other hand, a workflow is a combination of components, by which an input image is modified and processed in order to output the graph representation of the biofilaments.[1]

Method name and its software dependencies

This class defines the name of the method and also relates a method with other software packages or libraries required. In other words, a certain method may require another software package or libraries to be installed so they can be used. Such methods may be considered either a plug-in/add-on or a script/macro implementation. Although the *Method name* class defines the relationship of one method with other software packages and libraries, the relationship is observed indirectly. The observation is indirect in the sense that we do not specify a subclass edge as "plug-in of" or "script/macro of", but we just relate the name of the method with other software packages and libraries.

Image enhancement

It is important to know whether the method includes an image enhancement step or not since the existence or absence of such step can be related to how robust the further steps in the workflow are and also can be related to data input requirements of the method . We classified the publications primarily based on the existence or absence of an image enhancement method by including *Yes* and *None* subclasses, but also specified the types of enhancement used as subclasses of *Yes*, presented in figure 4.3. More detailed discussions about the pre-processing methods are in section 4.4.

[1]While defining such class *Type*, the intention was to divide it into three categories: component, workflow, and workflow coupled with data analysis. We created these three subclasses because most methods did not have a data analysis step and we wanted to discuss its importance for researchers, for previously unknown variables, could be useful for researchers in all the areas that do research in morphology and topology of biological filaments. However, this subjects is deep and complex enough for it to be the subject of another publication, so we only briefly discuss the data analysis step and variables. Refer to these publications to learn more about data analysis and variables: Heaton et al. (2012); Thomas (1992); Yang et al. (1992) for the analysis of fungal filament networks, Uylings e Van Pelt (2002) for the analysis of neurons, and Junker e Schreiber (2011) for global network properties related to graph theory.

Theoretical approach (includes segmentation, representation, and post-processing)

The is one of the most important classes of our classification and certainly the most complex and detailed. Based on the theoretical approaches of a method, one can have a better idea of how robust, accurate and fast a method may be. By knowing the theoretical approaches behind a method, it is also possible to note cases in which they may work or not. In addition, when image analysts and developers know the principles of the many theoretical approaches used to solve the same problem, they can develop new workflows or components using combinations of these approaches, in other words, find an approach that was not completely explored and tested and improve it. For this reason, it is crucial for such approaches to be clearly known and defined. Despite the importance of the definition of the theoretical approaches, a clear definition and separation of the theoretical approaches is nearly impossible because the classification of the approach is somewhat flexible and sometimes a certain approach can be classified in more than one way. That is why classifying is so difficult. In our work, we bring about this subject and encourage the bioimage analysis community to discuss the classification of theoretical approaches. In the following subsections, we present a detailed description of the subclasses considered within *Theoretical approach* class and refer to the basic bibliography for each main subclass subject.

1. Pattern Recognition

   Pattern recognition relates to computer vision and image analysis, although it is also known as part of the theory of machine learning. In our scope, the subclasses of pattern recognition involve mainly lower-level algorithms that try to detect, enhance, diminish, or measure features of interest in the images. A great part of the pattern recognition subclasses involves mathematical morphology theory, such as skeleton-based, ridge or crest-based, and watershed methods. The concepts of image gradients, filters, matching and steerable filters, and convolution are part of this class as well. Shapiro e Stockman (2001b), Forsyth e Ponce (2003), and Gonzalez e Woods (2011) discuss most of the theory found in the *Pattern recognition* subclasses found in our analysis.

   (a) Skeleton-based
   (b) Matching and steerable filters
   (c) Ridge or crest-based
   (d) Region growing
   (e) Connected set filters
   (f) Mathematical morphology
   (g) Other approaches

2. Model-based

   Humans are capable of identifying objects even if only part of the object can be seen. Humans can also identify unknown objects based on what they know about similar objects. This is possible because we use our previous knowledge of the other objects we have seen, such as shape, color or other features. In other words, we know something about the object before seeing it. Researchers have used this idea as an approach in algorithms to detect or extract the object of our interest by using previous knowledge about the object. Such algorithmic approaches are known as Model-based. The *Model-based* class comprises higher level algorithms, where the concept of model is introduced, which is how the object of interest can be represented or detected in the

image in mathematical terms. Xu et al. (2000), Yoo (2004), Sethian (1998) and Kass et al. (1988) provide some background on model-based methods.

Figure 4.4 shows examples of a template matching model (4.4A) and parametric deformable model (4.4B). The robustness and accuracy of a model-based method rely on how well the chosen model represent the dataset and the features of interest. For example, template matching methods such as the one depicted in Figure 4.4A fails to detect filaments with irregular surfaces and also filaments near branching points, which makes them suitable for filaments that do not have many branching points or to situations in which the branching points are not important. In case one chooses to use such method but wishes to detect branch points, an additional branch-point detection approach or post-processing step are needed improve the detection of branch-points. In some publications, for example the works of Krissian et al. (2000); Sato et al. (1998) and Frangi et al. (1998), authors treat as models the multi-scale filters that describe filament shapes to be detected and enhanced. In the current work, we categorize such publications in the *Matching/steerable filters* subclass of Pattern recognition. The types of model-based approaches are listed below:

(a) Template matching

(b) Parametric deformable models

(c) Geometric deformable models (or front propagation)

(d) Deformable template matching

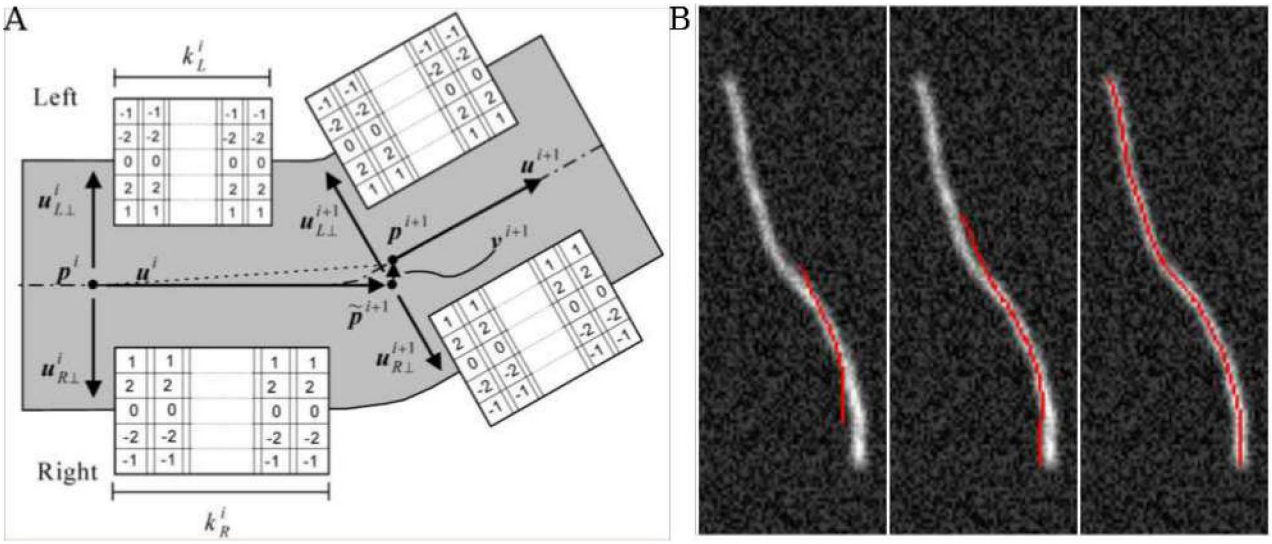

Figure 4.4: Examples of model-based approaches. (A) a template matching approach which is combined with exploratory tracing or vectorial tracking. The template is a low-pass differentiator of the form $[-2,-1,0,1,2]^T$ and the length of the kernel is adapted to better localize edges and link dynamically potential broken edges. The response of the template is checked to obtain the vectorial orientation u of the point p within the image and this response is searched recursively to detect all the filaments starting from initial seed points (user defined or automatically detected) (Al-Kofahi et al., 2003). (B) an open active contour approach (snakes). The 'snakes' are deformable parametric curves which are actively deformed based on the minimization of an energy function that commonly encompasses two different energies: an internal and an external energy (Smith et al., 2010). Image from the *JFilament* plug-in website `http://athena.physics.lehigh.edu/jfilament/`.

3. Graph-based

In mathematics and computer science, graph theory has been used for many decades. Differently, its use in image analysis is recent and it has been proposed as part of workflows of image analysis of biological filaments because of the nature of the final result of the biological filament tracing is a network of nodes connected by edges, exactly how a graph is defined. Basic graph theory references can be found in Diestel (2010) and Bondy e Murty (2011).

Graph-based algorithms exist most commonly as post-processing steps since the graph itself is not an image any more. Although the graph is not an image, it can be constructed using image properties. For example, a graph of a segmented foreground section of the image may compute the edge weights of a pair of nodes as the difference in intensity between these two nodes. On the other hand, there are situations in which the graph does not use image properties. An example occurs when the biological filaments that are extracted from the image by other approach but the resulting filament is represented as a graph. In that case, the only property that may relate to the image is the spatial position of the nodes, which should fall within a section of the filament in the image it was extracted from. In image analysis, graph-based methods commonly apply either shortest path (SP) algorithms, minimum cost path (MCP) or minimum spanning tree (MST) algorithms, in which the costs and optimality criteria may differ for each method.

There are at least two potential issues arising from using graph-based methods. The first is that the paths in the graph, which should represent the centrelines of the filament, may not be located at the exact centreline position. Secondly, MST algorithms possibly generate spurious branches due to its global optimality criteria. Due to these two issues, additional post-processing steps exist to improve the results of the final graph.

(a) Minimum cost path

(b) K-Minimum spanning tree (K-MST)

(c) Minimum spanning tree (MST)

(d) Q-Mixed integer Programming (Q-MIP)

4. Exploratory tracing or vectorial tracking

Exploratory tracing, also known as vectorial tracking methods, are used to track the object using local image properties and not the whole image. These methods are most commonly coupled with model-based methods. The model is recursively fit to regions in the image starting from user-defined or automatically detected seed points. Sometimes both the start and endpoints are required. As the models fit to limited regions of the image, the fitted model provides information about the direction and position in which the next tracing iteration will occur. Owing to the analysis of local image properties, this approach is computationally fast, but it fails in detecting highly branched or faint (in intensity) structures, because the models usually consider the filaments as being sections cylinders or ellipses. In addition, it may also fail to detect biological filaments with different filament diameters. For this reason, exploratory tracing coupled with model-based or other approaches commonly require post-processing steps to connect branches, in other words, fix filament intersections that the algorithm did not detect. Examples of such exploratory tracking approaches can be found in the works of Tsai et al. (2004), Al-Kofahi et al. (2008) and Rigort et al. (2012) (Figure 4.5)[2].

[2]Reprinted from Journal of Structural Biology, 177(1), Alexander Rigort, David Günther, Reiner Hegerl, Daniel Baum, Britta Weber, Steffen Prohaska, Ohad Medalia, Wolfgang Baumeister, Hans-Christian Hege, Hans-Christian,

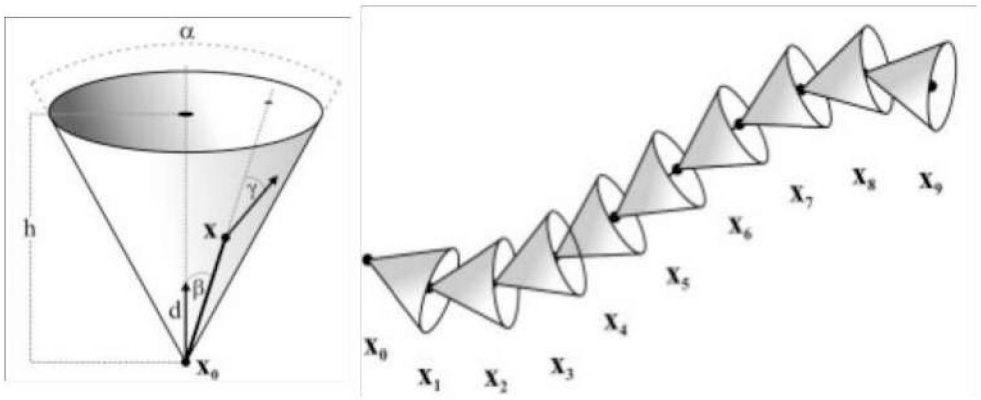

Figure 4.5: In (Rigort et al., 2012), the exploratory tracing were performed with a cone search window centered in the previous filament point x_0. Each point within the search cone receives a likelihood measure that defines what is the likelihood of the voxel to belong to a filament. The process is repeated for all voxels that are above a user-defined likelihood threshold.

5. Learning algorithms

   This group of algorithms is receiving a lot of attention in recent years. Within this group, we include neural network algorithms and other machine learning methods. In the present work, the defined specific classes did not use the most common way of separating learning algorithms (e.g. (i) supervised learning, (ii) semi-supervised learning, and (iii) unsupervised learning), although as these are growing in use in image analysis, it may be necessary to change the way to classify them. Only a few methods that use learning algorithms were found in the selected publications, so the sub-classes within *Learning algorithms* for image analysis of biological filaments will potentially grow over the next years.

   (a) Support vector machines (SVM)

   (b) Perceptron

   (c) Cascade of classifiers

   (d) Neural networks

   Learning algorithms in image analysis are used together with other approaches as means of improving parameter setting or improve image segmentation. A critical downside of most learning algorithms is the fact that they usually require significant amounts of test datasets (commonly known as *'ground truth'* or *'gold standard'* used by the learning algorithm in the learning process. However, such datasets may also be used to validate the method so a small part of the ground truth datasets is used for the learning process and the remainder may be used to validate the accuracy and precision of the methods. Examples of works that use learning algorithms may be found in Sironi et al. (2016); Santamaría-Pang et al. (2015); Liu et al. (2016).

6. Manual tracing

   Manual methods are included as part of *Theoretical approach* although they are not based on any theory. Manual tracing is performed by a user, often an expert in its field,

and is aided by a graphic user interface (GUI), so the user can select points in the image that represent nodes and identify edges between nodes, or select the image pixels that are part of the filament. Manual annotation of the images was for a long time the most used method to analyse images, however the situation has changed (see results).

Image type

The image type class refers to the types of images which an tracing method is capable of processing and the type of image required to execute the method. For example, the workflow proposed by Zhou et al. (2016) is capable of processing 3D images, but for that, it uses 2D maximum intensity projections (MIP) of the 3D images. In our classification, the node of the workflow of Zhou et al. (2016) has edges to image types *2D Stack (3D)* and *2D MIP*. The subclasses of *Image type*are *2D stack (3D)*, *2D*, *MIP*, and *time-lapsed 2D stack (3D)*.

Image intensity features

The methods differ by the image features used to execute their image processing steps. A certain method may only use binary images, other methods use grayscale or multi-channel (for example red, green, and blue - *RGB* - channels) image data or even information from both a binary and grayscale data. The class *Image feature* was added to define clearly what features a method uses. Sometimes it is not clear which features a method uses, and the more complex a method is or the more combinations of components it has, the higher is the chance that it uses more than one type of image feature. Subclasses *binary*, *grayscale* and *multi-channel* were defined as part of our classification.

Imaging technique

Different imaging techniques provide different types of images and, more importantly, different image qualities. In addition, the object of interest appears as low-intensity pixels or voxels in certain modalities, such as brightfield microscopy, but the same object appears as high-intensity pixels or voxels in fluorescence microscopy. For this reason, the class *Imaging technique* is crucial, so each method is defined as capable of processing images obtained by specific imaging techniques. The subclasses of the class *Imaging technique* are presented in Figure 4.3. We note that there is a special sub-class for methods that were developed for more than one imaging technique, named *Different modalities*. In section 4.4, we discuss why methods developed to work with images of different modalities are so important.

Programming language

Methods are also classified based on the programming language used. This is useful information for people who wish to understand more details behind the implementation of the methods and the theoretical approach used by the methods. In addition, a person who wants to start working with image analysis could prioritize their learning of a programming language based on the languages that are most used for image processing and analysis applications. The subclasses *Java*, *C*, *C++*, *Python* and *Matlab* exist within the class *Programming language*.

User interaction

There are cases where user input is required, for example when the user: (i) defines starting or endpoints at which the method should begin or finish (ii) defines parameters according to the

characteristic of the object of interest and characteristics of the image and (iii) edits the results based on their own judgement. Furthermore, some methods do not require user input or user input is optional. The class *User interaction* defines all these cases, along with the subclasses *None*, *Parameter setting*, *Defining seed points/endpoints* and *Other*.

Description of the analysis method

First we performed a search in the literature and recorded all search terms used. Then, we performed first readout and observed how many citations the publication had and separated the publications that appeared to be most relevant. After the first readout, we noted the potentially relevant citations of these first papers and took notes of other potential search terms. Again, we performed the task of observing potentially relevant publications and performed a new search, then again taking notes of new search terms. The search for publications was done in Web of Science and Google scholar databases with search terms related to our research interest (Filamentous fungi). The search terms for the first, second and following searchers can be found in Table 4.1.

Table 4.1: Search terms and boolean operators used to find publications of biofilament tracing methods

Search	**Search terms**
first	filament*, grow* OR elong* OR ext*, image proc*, morpho* OR physiol*
second	filament* OR network*, image, analys* OR process*, morpholog* OR topolog*, reconstruct* OR extract*
following*	curvilin* structure*, curv* feature*, tubular structure*, tube OR tube-like, tree OR tree-like, filament* network*, tracing

$\star$ used in conjunction with a combination of the keywords from the previous searches

After the selection of the first papers (about 50), we read them all and extracted the key terms that could relate to our classification, by constructing a large table, which consisted of an graph adjacency matrix, identifying edges between publications and their classification nodes. After the first publications, we went to general literature of image analysis to verify similar terms or concepts that could be misinterpreted and then adapted our classification accordingly. We then selected more publications and performed the same detailed readouts and classification. After that, once the table was sufficiently complete, we used GephiBastian et al. (2009) graph visualization and analysis software v0.9.2 to generate a graph visualization. We used the filter capabilities and computed the network parameters (node in-degree, node out-degree, pagerank, modularity score) to perform our analysis and get useful insights.

4.4 Results and discussion

4.4.1 Details of the publications: Year of publication, Journals and events and research fields

We analysed 87 publications that propose image analysis methods for biofilament tracing. Figure 4.6 shows a histogram of the year of publication (YOP) of the selected works. YOP spanned from 1994 to 2016, covering 22 years of developments in the subject, although the majority of works were published in the last 16 years. Only 5.7% of the publications (5 of them) have YOP

earlier than 2000. The YOP mean and modes are 2009 and 2008 and 2011, respectively. We must note that the literature is still under expansion, although our YOP histogram may show otherwise. With this review, we present quite recent literature, in which almost half the selected works were published after 2010, and we selected the works that appeared to showcase novel approaches or reached the state-of-the-art at the time of publication.

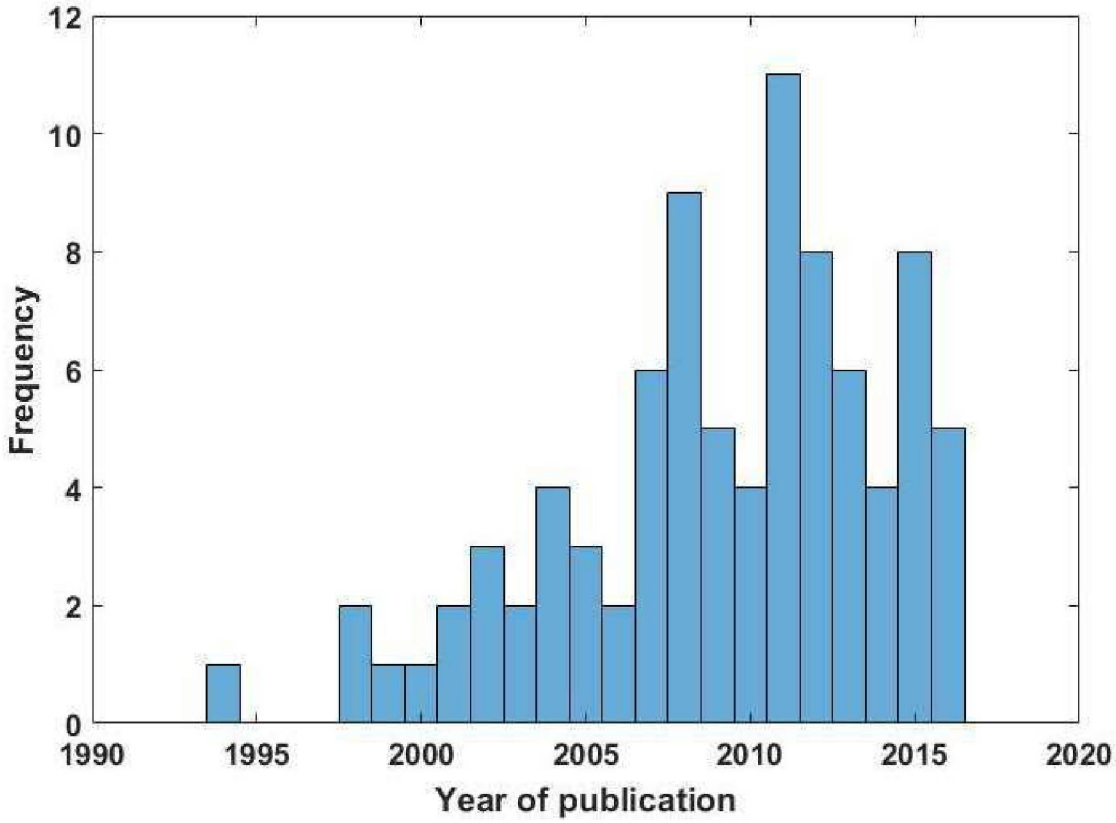

Figure 4.6: Frequency histogram of the Year of Publications (YOP)

The category in which the journals or events (Conferences, symposia or others) where the selected works were published (Figure 4.7) shows that approximately 22% of the journals and events are categorized as computer science and its specific areas. In addition, nearly 30% of the publications can be related to the area of computer science (Interdisciplinary applications, Image processing and computer vision, Artificial intelligence, Information systems, Pattern Recognition, Software Engineering and also Mathematical & computational biology).

In addition to the category graph presented in Figure 4.7, Figure 4.8 shows a word cloud of the journal and events in which the works were published. The word cloud may help direct the readers to specialized journals that published relevant works related to image analysis of biological filaments. The categories graph and the word cloud clearly show that neuroscience research is a relevant part of the literature. On the other hand, journals associated with computer science and its interdisciplinary applications are relevant as well. Although we expanded our search to provide a significant variety of research areas, note that there may be other journals and scientific events that publish relevant works on biofilament tracing methods as the selected publications comprise a tiny microcosm of the whole literature.

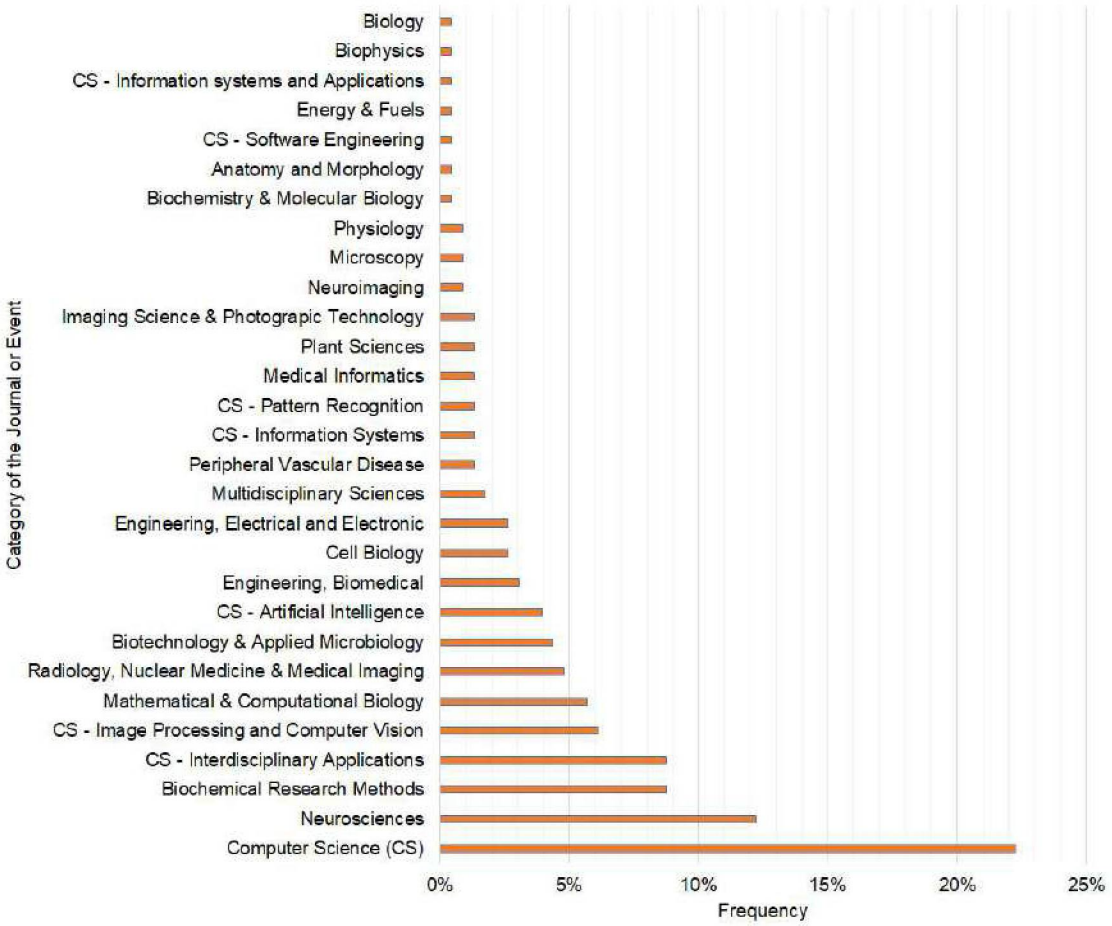

Figure 4.7: Bar plot of the categories of the journals and scientific events from the selected publications. The categories of 34 of the journals were based on Journal Citation Reports by Thomson Reuters, 1 From Springer journal category and the 8 remaining event categories were defined by the author.

4.4.2 Overview of the literature according to the proposed classification method

Relevant classes and insights about their relationship

With the selected works and our proposed classification, the resulting graph comprised 226 nodes, 9 being of the main classes, 130 of the sub-classes and 87 of the publications evaluated. There was a total of 1382 edges representing the relationship of the articles between the classes and sub-classes and also the relationship between the classes and the sub-classes. In order to evaluate the relevance of the classification nodes, we computed the node degrees.

The average node degree of the sub-classes was 10 and the standard deviation was 14. Figure 4.9 provides the cumulative frequency curve of the node degrees of the sub-classes. If one considers a relevant sub-class node to have a higher degree than the mean plus one standard deviation, it can be noted that there are only a few relevant sub-classes, with in-degrees higher than 24 (15 nodes, approximately 11.5% of the total sub-class nodes). The majority of the sub-class nodes have 1 to 4 degrees, comprising 58.5% of the total sub-class nodes. These results show us that our classification can be considered quite specific, at least with respect to the imaging technique and software sub-classes, which have degrees of 16 and 41, respectively. On the other hand, other main classes are less detailed (have fewer sub-class nodes) and will result in sub-classes with higher degrees, such as the existence of pre-processing, which has *Yes* and *No*

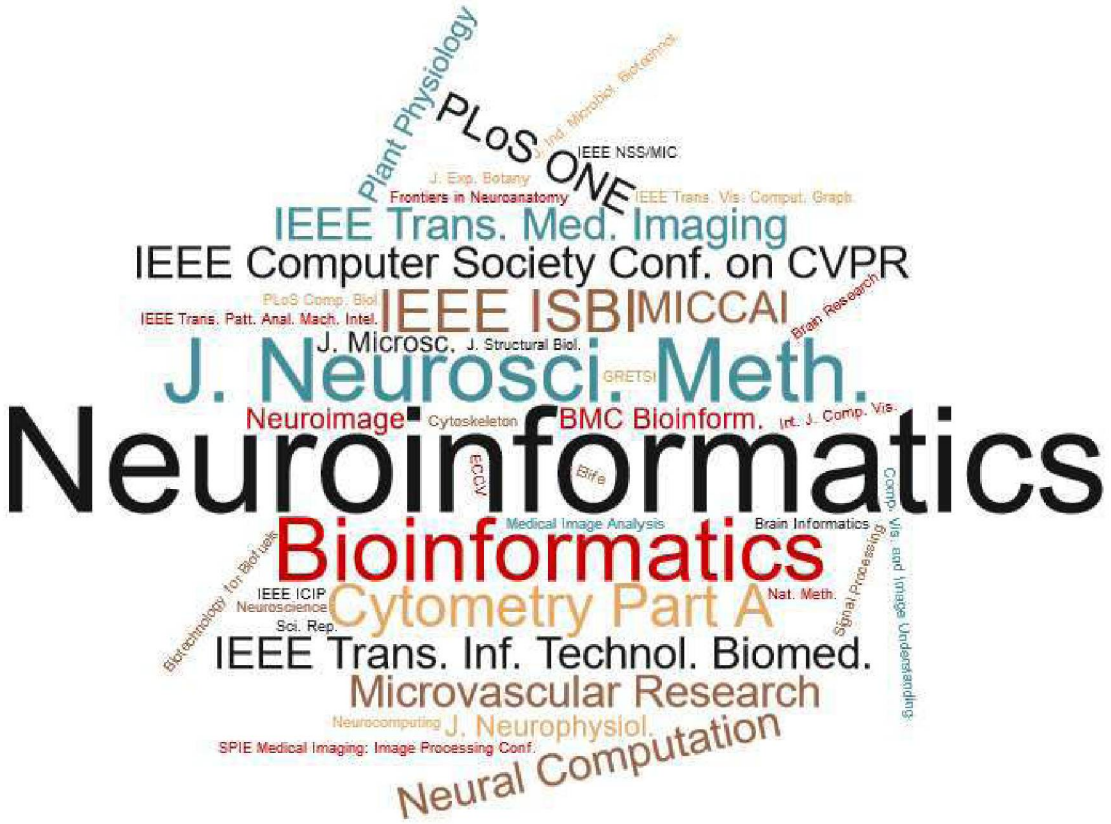

Figure 4.8: Word cloud showing the most frequent journals and scientific events from the selected publications. The sizes are according to the frequency of appearance.

nodes, and image feature, having *grayscale*, *binary*, *Maximum intensity projection (MIP)* and *Multi-channel* nodes.

Table 4.2 shows the most relevant sub-classes based on our classification. With respect to the type of work, 46.3% were classified as workflows, therefore requiring further calculation operations in order to obtain desired morphometric parameters. Another main group is of the workflows coupled with data analysis, 33.8% which provide some morphometric and topological measurements. In addition, we observed that each individual research group working with specific types of filaments is interested in their own morphometric parameters, although parameters such as total length, segment lengths, number of branch points, end-points, and filament radii are of common interest since they describe the basic information of the biofilaments. Such result shows that there is an opportunity for development of a common framework to compute morphometric parameters of all types in a single implementation, which would be of great value for every researcher that works with filament tracing.

One of the most important classes, *pre-processing* (or image enhancement), shows us that the selected works are quite balanced in this category. 55.2% (48 methods) defined a pre-processing or image enhancement step, of which approximately 46% of these included a filament enhancement method (see Figure 4.10). The remaining pre-processing methods were much less prominent, although smoothing (16.7%), background subtraction (14.6%), intensity normalization/equalization (12.5%), and deconvolution (12.5%) were other options chosen by the authors of the methods. The sum of the percentages goes beyond 100% due to the fact that it was common to combine more than one enhancement technique. In contrast, the methods that do not include any pre-processing step are divided into two groups: the model-based methods (especially

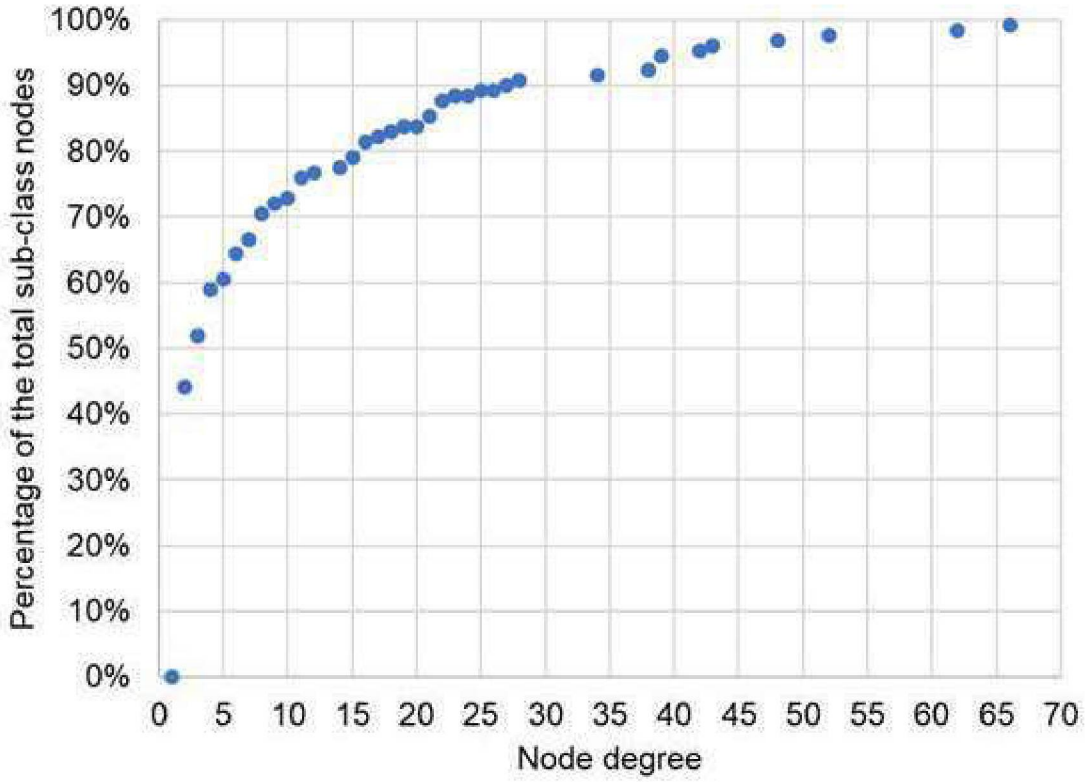

Figure 4.9: Cumulative frequency plot of the degree of the sub-class nodes.

parametric deformable models and template matching) and the pattern recognition methods combined with learning algorithms, graph-based or model-based approaches (see Figure 4.11). For this reason, model-based methods, especially template matching and parametric deformable models, may be potentially more robust to noisy datasets. Similarly, pattern recognition methods that combine with graph-based or learning algorithms are also potentially more robust to noisy images.

The type of image and the image feature utilization was evaluated as well. On our analysis, 75% of the methods could be used for 2D stacks of images (3D) and approximately 74% uses grayscale image features instead of binary to extract or reconstruct the biological network. The first result is expected, as we stated in our methodology that our interest is in 3D images. Therefore, the majority of the methods can be applied to them. However, we still considered in the review some of the relevant methods suitable for 2D images only. Interestingly, part of these works (10% of the total) works for both 2D and 3D images. Ideally, the best option would be to have methods for images of any dimension (nD), but there are a few issues to solve related to the increase of image size as the number of dimensions increase. First, the computational cost of some methods increase rapidly as the size of the image increases and as the complexity of the network increases, making them impossible to use or requiring new implementation approaches such as parallel programming strategies in order to be performed within a reasonable time (from seconds to a few hours). In case of time-lapse images, new methods may take advantage of the tracing information of adjacent frames so computational cost is decreased.

With respect to the use of image features, the majority (75% of the total) of the methods used grayscale information of the images. The remaining 25% that use binary features of the image after some type of segmentation relate to mostly skeleton-based methods (14 out of the 22 that use binary features, comprising approximately 64%). Grayscale is more pronounced

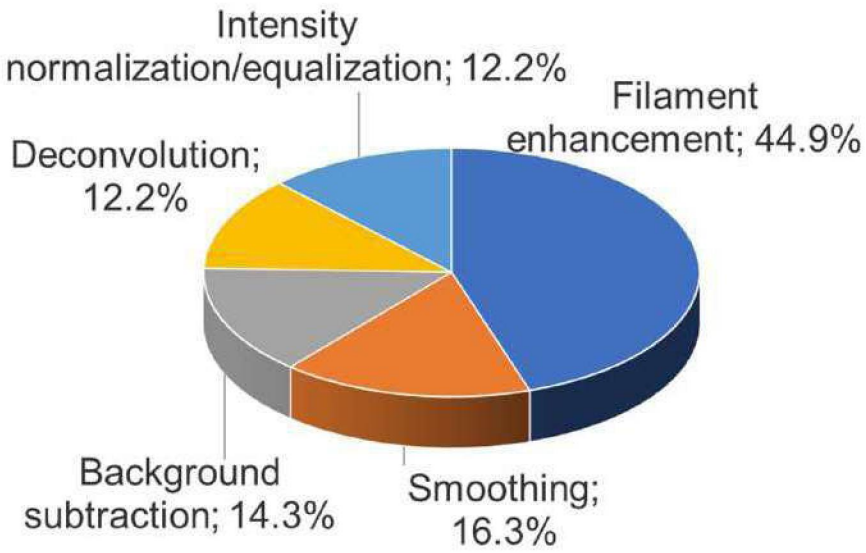

Figure 4.10: Pizza plot of the major pre-processing techniques used.

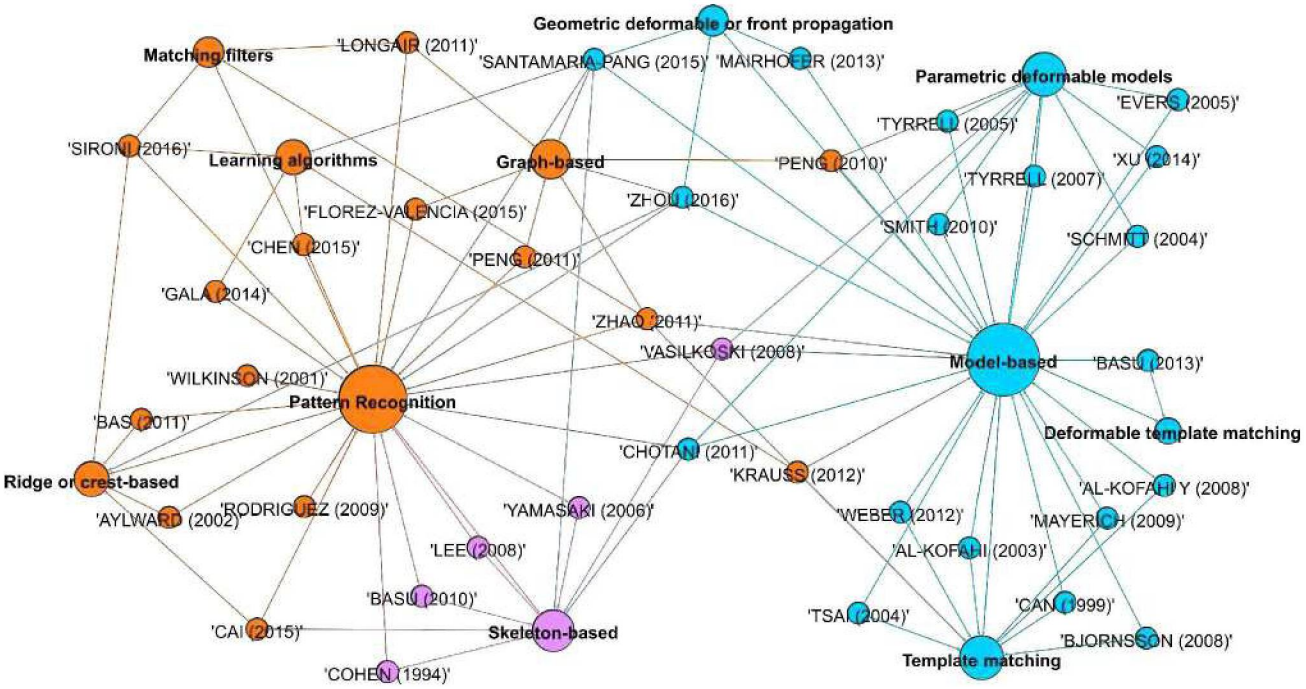

Figure 4.11: Sub-graph extracted from the complete classification graph of the methods that do not require pre-processing. The colours indicate the communities based on modularity measure Blondel et al. (2008)

compared to binary since most approaches require the complete intensity information of the image, such as most model based approaches.

The research field that stands out as having the majority of relevant methods is *Neuronal systems* (approx. 60%). This result was just confirmed since it could be already noted from the categories graph in Figure 4.8 and 4.9. The second and third relevant fields are *General* and *Blood vessels*, that amount to 13.8% and 12.6% each, and were not shown in the table due to their low node degree compared to *Neuronal systems*, although Figure 4.12(a) shows the relevance of each filament type in detail. The methods developed and tested for *General* images are more recent compared to the whole set of publications, 55% of them have the YOP of 2010 or later.

Within the selected publications, confocal microscopy imaging techniques were the most used (44,8%, see Figure 4.12(b)), especially laser scanning (CLSM comprised 54.8% of the confocal). Confocal techniques are suitable for the study of thick biological specimens and are capable of providing 3D images in high resolution, time-lapse 3D images (4D), and even in more than one color channel (5D or higher). As the image type results confirm, confocal is a consolidated technique in biological studies of 3D (2D stacks) biological filaments and it has been used for a long time (YOP of the works that used confocal microscopy spans our entire review from 1994 to 2016). On the other hand, another relevant node related to methods that were developed and tested for more than one imaging modality *Different modalities*, which comprise 32.2% of the publications. The methods developed for different modalities are not as common and also recent, with 80% of them being published in the last seven years. It is important to differentiate here the imaging technique and the filament type classifications. A method could have been developed for neuronal systems and considered datasets of different image modalities, as well as a general method, could have considered datasets of a single imaging technique, even though this is less common. We consider such methods suited for more than one imaging technique to be versatile. However, the versatility goes beyond the capability of a method to work on different imaging techniques, it depends on image quality, the scale of the filaments compared to the scale of the image as well as the filament type. The *General* methods considered in the class *Filament type* also contribute to this discussion. Only 10% of the methods were tested in more than one type of filament (e.g. neurons, pulmonary airways and blood vessels). Of course, there is a trade-off between the versatility of an image analysis method and its accuracy and precision. By narrowing the applications of the method, the method may provide more accurate and precise results. In contrast, if a method is tested for many different images, or better, different imaging techniques, the higher is the chance it will be more broadly used and approved by the bioimage analysis community. We believe that the bioimage analysis community needs both types of methods: The ones developed for a wider range of imaging techniques and the more specific ones. In the long-term, our opinion is that there should be image analysis methods capable of processing a wide range of imaging techniques and filament types but at the same time provide sufficiently accurate and precise results.

Out of the 87 publications analysed, 70% use at least one pattern recognition approach. Within the pattern recognition approaches, the most used are Matching / Steerable filters (25%) and Skeleton-based approaches (24%). The second major approach was the Model-based (39%), and within the model-based options, template matching (16%) and parametric deformable models (13%) are the most used. If one notes the percentage of the most used approaches, the sum of pattern recognition and model-based goes over 100%. This is another interesting observation: almost 60% of the methods used more than one theoretical approach. The combination of more than one approach is becoming more and more common in recent years, as researchers attempt to increase robustness and the accuracy and precision of the tracing results. This poses additional challenges to life scientists and image analysts, as the more complex methods become the more

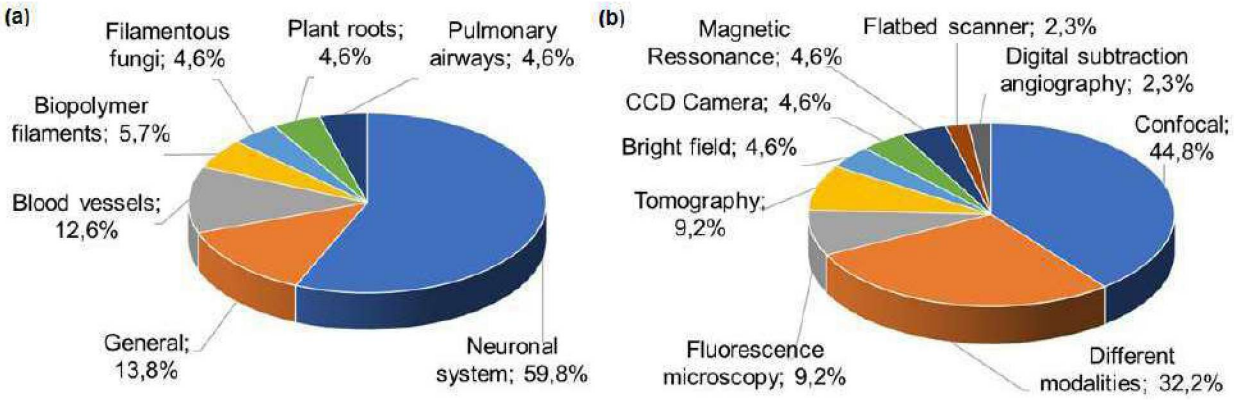

Figure 4.12: Plots showing the percentage of appearance of (a) filament types and (b) imaging techniques.

difficult it is to learn the theory behind them. However, such challenge can be overcome by proper documentation of the methods, accessibility to the source-code and the support of experienced image analysts and developers in the research facilities. Sironi et al. (2016); Santamaría-Pang et al. (2015); Yang et al. (2013) are examples of methods that use of many different theoretical approaches.

As two of the most critical aspects to be considered by intermediate and advanced users are the software name and the programming language. Unfortunately, a considerable fraction (almost 30%) of the publications either do not describe details of their implementation or do not provide access to it. This is more common in publications from journals of the computer science and related field, whereas in biosciences and bioengineering related fields the authors specify the software and provide access to their proposed method more often. Of course, the concept of open science and reliable and transparent research is growing every day and we expect an increase in availability of implementations and details about the algorithms. Luckily, the remaining 70% of the articles provide some details on their implementation and sometimes made them available. In those cases, the major software packages are Matlab®, Vaa3D, and ImageJ. They comprise 18.4%, 16% and 15% of the methods, respectively. It was expected that these would be the major software options since these accept plug-ins and user-written macros or scripts. ImageJ, Vaa3D and their plug-ins are open-source options and together their use surpasses the proprietary programming environment Matlab®. Open-source alternatives have active on-line communities and forums and such alternatives are built on transparency and collective efforts for improvement Cardona e Tomancak (2012). A great advantage of open-source approaches is to make it easier for a newcomer to the area of image analysis to start learning about it. The results of the software names and their dependencies are in line with the major software packages, with C++ (28,7%), Matlab (18.4%) and Java (13.8%) being the most commonly used. Evidently, the programming language aligns with the software options. Vaa3D and other standalone alternatives (FARSight, ORION, Neuromantic, among others) are mainly programmed in C++, ImageJ is Java-based and Matlab has its own language. Appendix A show two lists of software implementations available. There are at 40+ tools, from standalone applications to image processing libraries. With respect to the libraries, the publications cited ITK, VTK, OpenCV. These libraries are essential for the development of new filament tracing methods since they have been built by the community for quite some time and contribute to increasing reproducibility of the image processing methods and allow developers to save time in the development process by using the existing functions, classes, and algorithms.

Another subject we considered is user interaction. As for our and may run with default parameters, but also allow setting parameters. However, in some cases, the authors did not make

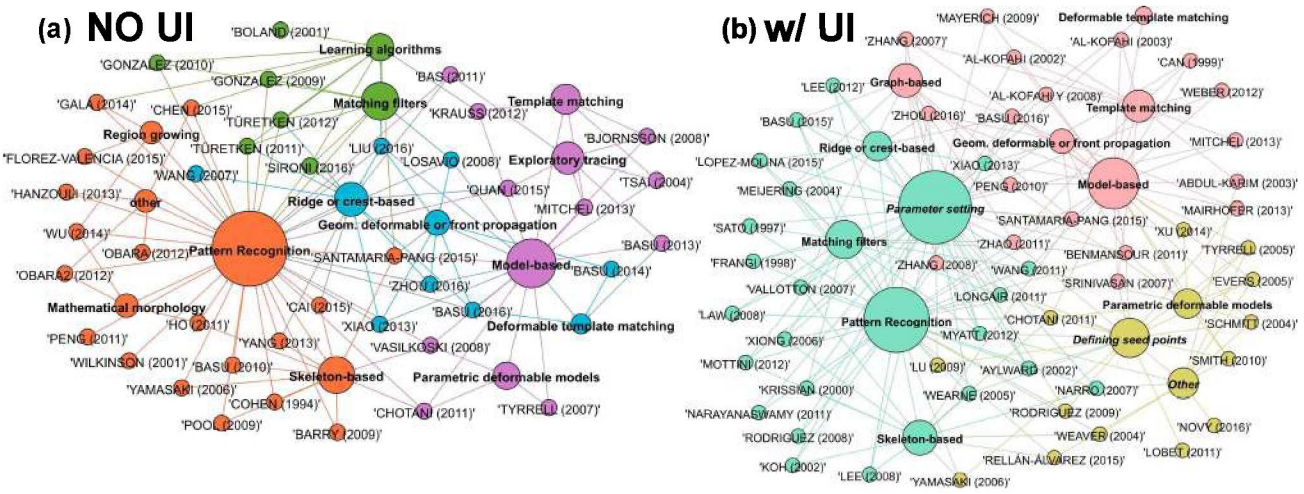

Figure 4.13: Sub-graphs extracted from the complete classification graph of the methods that (a) require some user interaction and (b) do not require user interaction. The colours indicate the communities based on modularity measure Blondel et al. (2008)

it clear whether parameter setting was possible or the parameters were fixed specifically for the use of their own images. Also, sometimes the implementation was not available to verify that. Other part of the publications require parameter setting (approximately 36%) or the definition of seed points (38%). Figure 4.13(a) and (b) shows the subgraphs of the publications that do not require any user interaction and the publications that require, respectively. Figure 4.13(a) shows no apparent major groups of approaches that do not require used interaction, but a small community of methods use learning algorithms are included. These methods are more recent and may be employed to either completely remove parameter setting by users or aid in parameter setting Sironi et al. (2016); Gala et al. (2014); Krauss et al. (2012); Türetken et al. (2012). On the other hand, Figure 4.13(b) show that Matching / Steerable filters comprise a community of methods that usually require parameter setting as well as the model based methods which require sometimes parameter setting and definition of seed points. We have evaluated a number of implementations Liu et al. (2016); Zhou et al. (2016); Quan et al. (2015); Xu et al. (2015); Xiao e Peng (2013); Peng et al. (2011); Chothani et al. (2011); Zhao et al. (2011); Wearne et al. (2005) and noted that there are cases in which a method allows the setting of far too many parameters (10 or more), from a user standpoint, theoretical approaches that allow the setting of too many parameters discourage their use by new users and requires an amount of learning that is significantly higher than methods that allow less parameters to be set.

4.5 Conclusion

The literature of biofilament tracing methods is very diverse with respect to the theoretical approach, and in recent years, most proposed methods take advantage of a combination of more than one single theoretical approach. In addition, graph-based strategies and learning algorithms are being used more often instead of the most classic techniques such as skeletonization and active contours (snakes). Learning algorithms may be used to help improving parameter setting or directly improve image segmentation.

Table 4.2: Most common classification of the selected publications

	Main Class and sub-class nodes *	Node degree	% of articles classified
Type of Work	**Workflow**	**43**	**49.4%**
	Worflow coupled with data analysis	**27**	**31.0%**
Filament type	**Neuronal systems**	**52**	**59.8%**
	General (tested in 2 or more filament types)	12	13.8%
Pre-processing	**Yes**	**41**	**47.1%**
	Filament enhancement	22	25.3%
	Smoothing	8	9.2%
Method classification**	**Pattern recognition**	**62**	**71.3%**
	Matching filters	22	25.3%
	Skeleton-based	21	24.1%
	Model-based	**34**	**39.1%**
	Template matching	14	16.1%
	Parametric deformable models	11	12.6%
Type of image	**2D stack**	**66**	**75.9%**
Image feature	**Grayscale**	**65**	**74.7%**

* Classifiers in bold font have degree equal or higher than the mean + standard deviation
** Methods that have theoretical approach degree ≥ 2 (combined more than one approach) = 50 (57.5%)

Table 4.2 Continuation: Most common classification of the selected publications

	Main Class and sub-class nodes *	Node degree	% of articles classified
Imaging Technique	**Confocal**	**39**	**44.8%**
	CLSM	21	24.1%
	Different modalities	23	26.4%
Software Prog. language	**Not Described**	23	26.4%
	Software		
	Matlab	16	18.4%
	Vaa3D	14	16.1%
	ImageJ	13	14.9%
	Programming language		
	C++	**25**	**28.7%**
	Matlab	16	18.4%
	Java	12	13.8%
User interaction	**None*** **	**41**	**47.1%**
	Parameter setting	**41**	**47.1%**

* Classifiers in bold font have degree equal or higher than the mean + standard deviation
*** Either fully automated or run using default parameters

The analysis presented hereby is useful to anyone working with biofilaments, because the biofilaments show similar features and characteristics, regardless of whether they are mycelia, neurons, plant roots or pulmonary airways. Our analysis also provides useful information for both users and developers: it helps users to understand the main principles behind the methods they use, and it may help developers to find gaps to improve existing methods.

Another aspect taken from our analysis is the fact that there is still a small number of biofilament tracing methods that were developed and tested for different filament types and different imaging techniques, in other words, more general methods. As a long-term goal, we think the bioimage analysis community should seek the development of more general biofilament tracing methods. One effort that could improve on that is the creation of a database of test datasets of images from various types of filaments obtained using different imaging techniques, along with relevant meta-data and ground truth annotations. Such database will contribute to benchmarking efforts, support the improvement of existing methods and the development of new methods as well as increase the communication between the different fields that make use of biofilament tracing methods.

The proposed classification provided sufficiently detailed information to obtain insights of the selected literature. However, we see this proposed classification as a first attempt to unify the biofilament tracing field of bioimage analysis and further discussions are needed so the methods are discussed and the theory behind them are understood by all researchers. The great heterogeneity and diversity of the literature and the known difficulty in classifying image analysis methods makes it necessary to participate actively in ongoing community efforts such as the development of the EDAM-Bioimaging ontology (Kalaš et al., 2018; Kalaš e from NEUBIAS Taggathons, 2018a,b). EDAM-Bioimaging is part of the EDAM project, a bigger

Table 4.3: List of publications considered in the analysis

Article #	Article Label	Authors	YOP	Journal or Event
1	SIRONI (2016)	Sironi et al. (2016)	2016	IEEE Trans. on Patt. Anal. and Mach. Intel.
2	NOVY (2016)	Novy et al. (2016)	2016	Biotechnology for Biofuels
3	BASU (2016)	Basu et al. (2016)	2016	IEEE Trans. Med. Imaging
4	LIU (2016)	Liu et al. (2016)	2016	Neuroinformatics
5	ZHOU (2016)	Zhou et al. (2016)	2016	Neuroinformatics
6	QUAN (2015)	Quan et al. (2015)	2015	Nat. Meth.
7	CAI (2015)	Cai et al. (2015)	2015	J. Exp. Botany
8	LOPEZ-MOLINA (2015)	Lopez-Molina et al. (2015)	2015	Signal Processing
9	FLOREZ-VALENCIA (2015)	Flórez-Valencia et al. (2015)	2015	GRETSI 2015
10	BASU (2015)	Basu et al. (2015)	2015	Journal of Microscopy
11	CHEN (2015)	Chen et al. (2015)	2015	Brain Informatics
12	RELLÁN-ÁLVAREZ (2015)	Rellán-Álvarez et al. (2015)	2015	Elife
13	SANTAMARIA-PANG (2015)	Santamaría-Pang et al. (2015)	2015	Neuroinformatics
14	BASU (2014)	Basu e Racoceanu (2014)	2014	IEEE ICIP 2014
15	XU (2014)	Xu et al. (2015)	2014	Scientific Reports
16	WU (2014)	Wu et al. (2014)	2014	Neuroimage
17	GALA (2014)	Gala et al. (2014)	2014	Frontiers in Neuroanatomy
18	BASU (2013)	Basu et al. (2013)	2013	MICCAI 2013
19	XIAO (2013)	Xiao e Peng (2013)	2013	Bioinformatics
20	HANZOULI (2013)	Hanzouli et al. (2013)	2013	IEEE Nuclear Science Symposium and Medical Imaging Conference (2013 NSS/MIC)
21	YANG (2013)	Yang et al. (2013)	2013	BMC Bioinformatics
22	MITCHEL (2013)	Mitchel et al. (2013)	2013	J. Neuroscience Methods
23	MAIRHOFER (2013)	Mairhofer et al. (2013)	2013	Plant Methods

Table 4.3 Continuation: List of publications considered in the analysis

Article #	Article Label	Authors	YOP	Journal or Event
24	OBARA (2012)	Obara et al. (2012b)	2012	Bioinformatics
25	KRAUSS (2012)	Krauss et al. (2012)	2012	PloS ONE
26	OBARA2 (2012)	Obara et al. (2012a)	2012	SPIE Medical Imaging: Image Processing Conference 2012
27	WEBER (2012)	Rigort et al. (2012)	2012	J. Structural Biol.
28	MOTTINI (2012)	Mottini et al. (2012)	2012	IEEE ISBI 2012
29	LEE (2012)	Lee et al. (2012)	2012	PLoS Comp. Biol.
30	TÜRETKEN (2012)	Türetken et al. (2012)	2012	IEEE Conference on CVPR 2012
31	MYATT (2012)	Myatt et al. (2012)	2012	Frontiers in Neuroinformatics
32	PENG (2011)	Peng et al. (2011)	2011	Bioinformatics
33	LOBET (2011)	Lobet et al. (2011)	2011	Plant Physiology
34	LONGAIR (2011)	Longair et al. (2011)	2011	Bioinformatics
35	CHOTHANI (2011)	Chothani et al. (2011)	2011	Neuroinformatics
36	NARAYANASWAMY (2011)	Narayanaswamy et al. (2011)	2011	Neuroinformatics
37	WANG (2011)	Wang et al. (2011)	2011	Neuroinformatics
38	BAS (2011)	Bas e Erdogmus (2011)	2011	Neuroinformatics
39	ZHAO (2011)	Zhao et al. (2011)	2011	Neuroinformatics
40	TÜRETKEN (2011)	Türetken et al. (2011)	2011	Neuroinformatics
41	HO (2011)	Ho et al. (2011)	2011	BMC Bioinformatics
42	BENMANSOUR (2011)	Benmansour e Cohen (2011)	2011	Int. J. Comp. Vis.
43	PENG (2010)	Peng et al. (2010a)	2010	Bioinformatics
44	GONZALEZ (2010)	Gonzalez et al. (2009)	2010	IEEE Computer Society Conference on CVPR 2010
45	BASU (2010)	Basu et al. (2010)	2010	IEEE ISBI 2010
46	SMITH (2010)	Smith et al. (2010)	2010	Cytoskeleton
47	RODRIGUEZ (2009)	Rodriguez et al. (2009)	2009	J. Neuroscience Methods

Table 4.3 Continuation: List of publications considered in the analysis

Article #	Article Label	Authors	YOP	Journal or Event
48	GONZALEZ (2009)	Gonzalez et al. (2009)	2009	IEEE Computer Society Conference on CVPR 2009
49	MAYERICH (2009)	(Mayerich e Keyser, 2009)	2009	IEEE Trans. Visualization and Computer Graphics
50	BARRY (2009)	Barry et al. (2009)	2009	Journal of industrial Microbiology and Biotechnology
51	LU (2009)	Lu et al. (2009)	2009	PLoS ONE
52	BJORNSSON (2008)	Bjornsson et al. (2008)	2008	J. Neuroscience Methods
53	AL-KOFAHI Y (2008)	Al-Kofahi et al. (2008)	2008	Cytometry Part A
54	RODRIGUEZ (2008)	Rodriguez et al. (2008)	2008	PLoS ONE
55	ZHANG (2008)	Zhang et al. (2008)	2008	Neural Computation
56	LEE (2008)	Lee et al. (2008)	2008	IEEE ISBI 2008
57	LOSAVIO (2008)	Losavio et al. (2008)	2008	Journal of Neurophysiology
58	VASILKOSKI (2008)	Vasilkoski e Stepanyants (2009).	2008	J. Neuroscience Methods
59	POOL (2008)	Pool et al. (2008)	2008	J. Neuroscience Methods
60	LAW (2008)	Law e Chung (2008)	2008	ECCV 2008
61	SRINIVASAN (2007)	Srinivasan et al. (2007)	2007	Neuroinformatics
62	ZHANG (2007)	Zhang et al. (2007)	2007	J. Neuroscience Methods
63	TYRRELL (2007)	Tyrrell et al. (2007)	2007	IEEE Trans. Med. Imaging
64	WANG (2007)	Wang et al. (2007)	2007	IEEE ISBI 2007
65	VALLOTTON (2007)	Vallotton et al. (2007)	2007	Cytometry Part A
66	NARRO (2007)	Narro et al. (2007)	2007	Brain Research
67	YAMASAKI (2006)	Yamasaki et al. (2006)	2006	Neurocomputing
68	XIONG (2006)	Xiong et al. (2006)	2006	Cytometry Part A
69	WEARNE (2005)	Wearne et al. (2005)	2005	Neuroscience
70	EVERS (2005)	Evers et al. (2005)	2005	Journal of Neurophysiology
71	TYRRELL (2005)	Tyrrell et al. (2005)	2005	Microvascular Research
72	MEIJERING (2004)	Meijering et al. (2004)	2004	Cytometry Part A

Table 4.3 Continuation: List of publications considered in the analysis

Article #	Article Label	Authors	YOP	Journal or Event
73	WEAVER (2004)	Weaver et al. (2004)	2004	Neural Computation
74	SCHMITT (2004)	Schmitt et al. (2004)	2004	NeuroImage
75	TSAI (2004)	Tsai et al. (2004)	2004	IEEE Transactions on Information Technology in Biomedicine
76	ABDUL-KARIM (2003)	Abdul-Karim et al. (2003)	2003	Microvascular Research
77	AL-KOFAHI (2003)	Al-Kofahi et al. (2003)	2003	IEEE Transactions on Information Technology in Biomedicine
78	AL-KOFAHI (2002)	Al-Kofahi et al. (2002)	2002	IEEE Transactions on Information Technology in Biomedicine
79	KOH (2002)	Koh et al. (2002)	2002	Neural Computation
80	AYLWARD (2002)	Aylward e Bullitt (2002)	2002	IEEE Transactions on Medical imaging
81	BOLAND (2001)	Boland e Murphy (2001)	2001	Bioinformatics
82	WILKINSON (2001)	Wilkinson e Westenberg (2001)	2001	MICCAI 2001
83	KRISSIAN (2000)	Krissian et al. (1997)	2000	Computer Vision and Image understanding
84	CAN (1999)	Can et al. (1999)	1999	IEEE Transactions on Information Technology in Biomedicine
85	FRANGI (1998)	Frangi et al. (1998)	1998	MICCAI 1998
86	SATO (1998)	Sato et al. (1998)	1998	Medical Image Analysis
87	COHEN (1994)	Cohen e Kimmel (1997)	1994	Journal of Microscopy

project in bioinformatics (Ison et al., 2013). We are now in collaboration with EDAM-bioimaging development team to discuss and support the creation of an ontology dedicated to bioimage analysis, bioimage informatics and bioimaging. This way, future exploratory literature research will become simpler, more reliable and transparent and be in line with FAIR principles (Findable, Accessible, Interoperable and Reusable) Wilkinson et al. (2016). If the use of ontologies is coupled with current data and text mining techniques, a greater number of publications may be explored and analysed. Another approach to be explored in the future is to search by software implementations instead of by publications and use the power of the whole bioimage analysis community to help finding these methods. The NEUBIAS COST action (CA15124) is currently developing a crowdsourced bioimage search engine webtool which will be become publicly available in the near future and authors are in collaboration with NEUBIAS to support the action and curate biofilament tracing methods.

5 The complex three-dimensional growth of a filamentous fungus is revealed through biofilament tracing methods

This chapter includes the results obtained throughout the Masters project and is the preliminary draft of an original article to be submitted to the Journal of Microscopy.

5.1 Summary

In research into the growth of filamentous fungi, analysing the morphology of the mycelium of a growing fungus is critical to understand heat and mass transfer phenomena in biotechnological applications of filamentous fungi. For example, interparticle nutrient uptake and extracellular enzyme secretion phenomena in a bioreactor that produces hydrolytic enzymes such as cellulases and pectinases. The morphology of a fungal mycelium can be analysed through microscopy techniques and the use of image processing and analysis techniques. In the present work, one of the objectives of the present work is to evaluate image enhancement techniques that are commonly used prior to biofilament tracing methods, which extract information of the mycelium from the image. We enhance sample images and evaluate the results by image quality parameters such as the structural similarity index (SSIM) and signal-to-noise ratio (SNR). After choosing the best combination of pre-processing techniques that provide images of increased quality, we used these pre-processed images as input to several existing biofilament tracing methods and evaluated the tracing results qualitatively. Finally, we chose the best filament tracing method and obtained morphometric parameters of the mycelium of a strain of *Aspergillus niger* growing on agar culture media with two different nutrient sources (glucose and polygalacturonate). The results show that the use of confocal laser scanning microscopy (CLSM) and filament tracing methods is a promising approach to better understand the complex three-dimensional growth of the mycelium: Biofilament tracing allows the acquisition of data from the complex fungal growth on an heterogeneous environment. Secondly, the scale of the images allow tracing a region larger than a few individual hyphae but a smaller than a complete colony, which is enough to observe how the spores germinate and the hyphae extend and form the mycelium.

5.2 Introduction

Understanding the complex morphology during the growth of the mycelium of a filamentous fungus is important because mycelial morphology relates to micro- and macroscopic phenomena of interest, for example, mass and heat transport phenomena in a large-scale bioreactor, physiological states that indicate the production of secondary metabolites, nutrient uptake and the secretion of

hydrolytic enzymes. Fungal morphology can be studied by using in-vivo microscopy techniques, for example Confocal Laser Scanning Microscopy (CLSM), and image analysis techniques. A representation of the mycelium is extracted from the image through biofilament tracing methods, which usually result in a graph representation of the mycelium detected in the image, with connectivity information and diameter of the traced filaments in a .swc file format. However, it is common to have images that contain undesired features or poor contrast and also other image quality issues that make it difficult to obtain quantitative measurements.

In some cases, the low-quality images are the only images one has. It might be the case that the sample preparation, microscopy technique and image acquisition settings were already set to maximize image quality but still they result in images of low quality. In contrast there might be cases in which the experiment and techniques are not well established yet and but the images acquired are still useful for research. Thus, it is common to enhance these images to remove the undesired features, correct and improve contrast or enhance the features of interest so the filament tracing algorithm of choice provides more accurate results. There are many image enhancement methods and, because of that, the choice of the proper pre-processing techniques may become significantly difficult. Existing biofilament tracing methods commonly involve one or more of the following enhancement methods: filament enhancement, smoothing (gaussian or median filter), intensity normalization or equalization, image deconvolution and background subtraction (Chapter 4). Another reason that makes choosing image enhancement methods difficult is that their order may also result in images of different qualities. One option for deciding which enhancement to use is to compute image parameters such as the signal-to-noise ratio (SNR), mean-squared error (MSE), and structural similarity index (SSIM) (Wang et al., 2004; Wang e Bovik, 2009). They help the researcher to make a better decision of which pre-processing methods to apply to their images, though the decision may still be a challenge considering that there are parameters to set in these enhancement methods and there is more than one technique that result in the same or very similar outputs. We propose a factorial design approach to evaluate a selection of pre-processing methods. Factorial designs are more efficient in finding optimal conditions of a desired outcome at no additional cost and allow the analysis of interactions between factors (combinations) compared to simpler one-factor-at-a-time approach or trial and error approach. We use a full factorial design to verify whether the enhancement methods or a combination of them would improve image quality. In addition, we also test the order in which the methods are applied to verify whether there is an impact in image quality or not. This factorial design approach was applied to two different confocal 3D sample images of a filamentous fungus growing on agar culture media.

Following the image enhancement tests come the biofilament tracing method itself. Again, the literature contains a great number of implementation options and algorithms. Thus, it is important to determine which biofilament tracing methods are more appropriate for the images and the research purpose based on criteria of interest: in biofilaments in general, it is common that the connectivity and the geometry of the biofilaments to be the most important features to be analysed Gillette et al. (2011); Mayerich et al. (2012). With the criteria defined the evaluation of the best methods may involve simple qualitative observations or quantitative detailed measurements such as diameter, topological and surface accuracy. Benchmarking filament tracing methods is yet a difficult task, since there are many issues involved with benchmarking. First, the availability of a sufficiently high number of annotated sample datasets (ground truth or gold standards) is a bottleneck and not always possible. Second, the reproducibility of the results of the biofilament tracing methods is difficult, because the implementations are not always fully and optimally developed or there are issues in the source code available. In the present work, we present a preliminary qualitative analysis of some of the most successful biofilament tracing

methods to our sample 3D images of filamentous fungi and discuss future directions to solve the problem of benchmarking filament tracing methods.

5.3 Materials and Methods

Construction of the fluorescent strains

Fluorescent strains were constructed from *Aspergillus niger* ATCC 1015 (CBS 113.46) by Maura Harumi Sugai-Guérios during her doctoral studies. The strains express enhanced green fluorescent protein (eGFP) and the expresion of which is controlled by the *gpd* promoter from *Aspergillus nidulans*, a strong constitutive promoter. The protein eGPF remains in the cytosol and allows visualisation of the specimen under CLSM. All plasmids were produced in *Escherichia coli* TOP10 cells (Sugai-Guérios, 2016).

Image acquisition

Two growth experiments were performed on agar culture media with glucose (Glu) and polygalacturonate (PGal) by Maura Harumi Sugai-Guérios . Synthetic complete media (SC) were used: 6.7 $g.L^{-1}$ yeast nitrogen base for microbiology (product code 51483; Sigma-Aldrich, Germany), 20 $g.L^{-1}$ agar, 120 $mmol.L^{-1}$ NaH_2PO_4 / Na_2HPO_4 buffer (pH 6) supplemented with the carbon source 20 $g.L^{-1}$ D-Glucose (SCD medium) or the same concentration, in $Cmol.L^{-1}$, for polygalacturonate (using the sodium salt; SCPgal medium). Spores were spread uniformly over the solidified medium and resulted in 40 $spores.mm^{-2}$. A small cube of the inoculated medium was excised and laid on a glass bottom petri dish with 4 chambers, with the inoculated surface perpendicular to the glass surface, before being transferred to the microscope. A cotton patch was put on one of the chambers of the glass bottom dish to ensure that the air in the dish remained saturated with water. The inoculated media were incubated at 30^oC (Sugai-Guérios, 2016).

A confocal laser scanning microscope (Nikon A1MP+, Nikon Instruments Inc., Japan) with a temperature-controlled chamber was used to obtain 3D images at different times during growth. A 20× (0.75 NA) lens was used and the eGFP present in the fluorescent strain was excited with a 488 nm wavelength laser and detected with a filter interval ("bandpass") of 500-550 nm. Images were acquired with 16-bit grayscale bit depth and converted to 8-bit grayscale. Glucose sample images were 973x973 px with 76 z stacks and 7 time frames and polygalacturonate sample were 948x1383 px with 76 z stacks and 7 time frames ($xyzt$). The xy resolution was and 1.2361 μm xy and 2 μm axial (z) resolution. The glucose sample was put under the microscope after 6 h of pre-incubation and polytaclaturonate sample after 10 h of pre-incubation. Image stacks (3D images) were acquired at every 4 h and 2.83 h for the Glucose and Polygalacturonate experiments, respectively. The times reported are the total times since inoculation.

Factorial design for the evaluation of the choice of pre-processing

The effect of four pre-processing techniques was tested: Deconvolution (*Deconv*), Background subtraction (*BS*), image intensity normalization (*Norm*), Frangi vessel enhancement method (*Fra*) and smoothing with median filter (*Med*). Only one out of the seven frames of each experiment was used to perform the pre-processing tests (Frame 5, representing the growth after 22,5 h). The order of these pre-processing techniques could also affect the image quality results, so the order of two pre-processing techniques was tested as well. As shown in Table 5.1, ORD_{median} and ORD_{Norm} relate to the order median filter and image intensity normalization in the tests.

Table 5.1 shows the seven factors considered in the factorial design and their levels and Table 5.2 shows a reduced 2^5 test table with coded factor levels. The experiments of the design shown in Table 5.2 were performed four times, two for ORD_{median} and two for ORD_{Norm} (for their low and high levels (-1, +1), with the order shown in Table 5.3. An ImageJ Fiji (Schindelin et al., 2012) macro script was written to execute the enhancement operations automatically.

Table 5.1: Factors considered in the factorial design and their levels

Factor	Description	Low level (−1)	1 High level (+1)
ORD_{median}	Position of the median filter in the order of pre-processing	Median is the first operation	Median is the last operation
ORD_{Norm}	Position of the normalization operation in the order of pre-processing	Normalization occurs before Frangi vesselness	Normalization occurs after Frangi vesselness
BS	Operation background subtraction with rolling ball method	Ball radius 5 px	Ball radius 20 px
Norm	Operation of image intensity normalization	Do not apply normalization	Apply normalization with 0.4% saturated px
Fra	Frangi vesselness multi-scale Hessian based filament enhancement	Do not apply Frangi vesselness	Apply Frangi vesselness 4 Levels, 2 px lower and 5px upper diameter
Med	Convolve image with median filter	Do not apply median filter	Apply median filter, kernel 2 px

Table 5.2: Full 2^4 factorial design excluding the *ORD* factors

Experiment Number	BS	Norm	Fra	Med
1	−1	−1	−1	−1
2	+1	−1	−1	−1
3	−1	+1	−1	−1
4	+1	+1	−1	−1
5	−1	−1	+1	−1
6	+1	−1	+1	−1
7	−1	+1	+1	−1
8	+1	+1	+1	−1
9	−1	−1	−1	+1
10	+1	−1	−1	+1
11	−1	+1	−1	+1
12	+1	+1	−1	+1
13	−1	−1	+1	+1
14	+1	−1	+1	+1
15	−1	+1	+1	+1
16	+1	+1	+1	+1

After applying the enhancement operations for each 64 test cases, we obtained the Structural similarity index (SSIM) and Signal-to-noise ratio (SNR) of each image with respect

Table 5.3: The order of computation of the pre-processing methods, referred as ORD_{median} and ORD_{Norm} factors

Experiment Number	Order			
1	BS	Norm	Fra	Med
2	BS	Fra	Norm	Med
3	Med	BS	Norm	Fra
4	Med	BS	Fra	Norm

to the original. Then fitted the factorial design model based on the effect of individual factors, pairwise factor interaction, three-factor interactions and four-factor interaction. The final result provides a Pareto plot for each *ORD* factor showing whether the effect of the factor on the outcome (SSIM and SNR) was significant. Four separate full 2^4 designs were done in order to make it easier to analyse the results. The chosen order for the enhancement operations was the one that provided the best outcome result for both the SSIM (the result that reached the value nearest to 1) and SNR (the highest possible value).

Tracing the mycelial network

The pre-processed sample images were used to evaluate eight automated filament tracing methods: (1) All-path pruning (APP) (Peng et al., 2011), (2) All-path pruning 2 (APP2) (Xiao e Peng, 2013), (3) NeuTube (Feng et al., 2015), (4) NeuroGPS Tree (Quan et al., 2015), (5) NeuronStudio (Wearne et al., 2005; Rodriguez et al., 2008, 2009), (6) Neural Circuit Tracer (Chothani et al., 2011; Gala et al., 2014), (7) FarSIGHT snake (Wang et al., 2011; Narayanaswamy et al., 2011), and (8) TreMAP (Zhou et al., 2016). All methods output files with a .swc file format, which comprises a graph representation of the filament extracted from the image. The .sec file provides a list of nodes, in which each row is a node and there are 7 columns of information: node identifier (an integer), its position in space (in Cartesian coordinates x,y, and z), a structure identifier (developed to identify neuronal structures), its radius and its parent node. The structure identifier was not used in the present work. The methods were run with default parameters whenever possible and some of their parameters were modified to verify changes in the results. Finally, results were evaluated qualitatively through visualization of the tracings and we defined the most promising tracing method to be used in our images for further computation of morphometric parameters, which was the method that provided the most accurate and complete tracings.

Calculating the growth and morphometric parameters

In order to compute the morphometric parameters, we developed a Matlab library named `Biofilament metrics`, which we have made available on Appendix F.

Biomass density - Biomass density (%), X_k/V_k, is the fraction of volume occupied by biomass in a certain volume region k of the sample multiplied by 100. For the purpose of understanding the biomass distribution as a function of the distance from the substrate surface, the function `biomass profiles` calculates the biomass densities as a function of a cartesian coordinate. We defined biomass profiles as a function of the y coordinate, since the surface of the substrate appears approximately as a line in y and a xz plane. To calculate biomass densities from the .swc file, `biomass profiles` calculates the Euclidean distances between every edge (the connection between a node and its parent) in the graph. The user may define the number of slices into which the image volume will be divided and the y coordinate limits of each bin k ($y_{k,min}$, $y_{k,max}$) are defined accordingly. After that, subgraphs are extracted for each slice volume and the total biomass volume is computed by summing the volumes of all edges in the subgraph.

The volume of each edge in the subgraph is calculated as the volume of a cylinder with the same length as the Euclidean distance of the corresponding edge L_{edge} and the estimated diameter of the hypha d_{hypha}. There are special cases of edges that cross the limits of the slice volume. To attribute the volumes appropriately to each slice, we detect how much of the edge volume lies out of the slice by calculating the Euclidean distance between the parent node and the $(y_{k,min}, y_{k,max})$ xz planes and define to which slice (upper bin, $k-1$, or lower bin, $k+1$) the volume should be added. The biomass volume for each bin k is computed as the sum of the volume of all edges within the slice that do not cross the slice volume and the partial volumes of edges that cross the limits of the slice volume.

$$X_k = \sum_{i=1}^{n_{edges}} L_{edge,i}.\frac{\pi.{d_{hypha}}^2}{4} + K_{cross,i}.L_{edge,i}.\frac{\pi.{d_{hypha}}^2}{4} \tag{5.1}$$

$K_{cross,i}$ is the fraction of the edge i ($0 \leq K_{cross} \leq 1$) that crosses either upper or lower xz planes ($y = y_{k,min}$ or $y = y_{k,max}$) and is located within the slice k volume.

Finally, the biomass density is computed by dividing the biomass volume X_k times 100 by the slice volume (V_k), calculated by

$$V_k = x.z.|(y_{k,min} - y_{k,max})| \tag{5.2}$$

where x is the length of the image in the x coordinate, in μm and z is the depth of the image, in μm.

Colony total length, extension rate and percentage increase in length - The total length of the colony at time t_i, $L_{total,i}$ (mm), was calculated by summing the Euclidean distances of all edges of the graph. The colony extension rate, dL/dt_i at time dt_i ($mm.h^{-1}$), was then calculated as below

$$dL_{total,i}/dt_i = (L_{total,i} - L_{total,i-1})/(t_i - t_{i-1}) \tag{5.3}$$

Number of tips, tip extension rate and HGU - The number of tips at time t_i, n_i, was calculated by determining how many nodes in the .swc file were not parents of any other node in the graph. The tip extension rate, $q_{tip,i}$ in $\mu m.h^{-1}$ at time t_i (Equation 5.4), was calculated by dividing the colony extension rate at time t_i by the number of tips n_i.

$$q_{tip,i} = (dL_{total,i}/dt_i)/n_i \tag{5.4}$$

This value underestimates the tip extension rate, since the number of tips may vary greatly from t_{i-1} to t_i and the calculation is performed with the number of tips at exactly the time t_i. With the total length and the number of tips, the Hyphal Growth unit was also calculated.

5.4 Results

The results are divided into three sections: section 5.4.1 presents the results of the analysis of image enhancement methods, then section 5.4.2 shows the qualitative analysis of the biofilament tracing methods and finally 5.4.3 shows the results of the morphometric parameters computed from the tracing results.

5.4.1 Pre-processing factorial design

For better analysis, the results in this section must be analysed along with tables 5.2 and 5.3. Figures 5.1 and 5.2 show the results of the 64 tests for each sample image, Glu and PGal, respectively and the SNR and SSIM outcomes. In the case of the Glu sample image (Figure 5.1) tests 1-4 and experiments 9-12 are the ones that give the best improvements in SNR. Test 2 give the best SNR outome followed by test 10. In test 2, only background subtraction *BS* operation (level +1, rolling ball radius 20 px) is applied. In experiment 10, both background subtraction and the median filter $BS(+1)$ and $Med(+1)$are applied. On the other hand, Frangi vesselness decreases image quality. This is observed in tests 5-8 and 13-16 for both SNR and SSIM outcomes, show $Fran$ has a negative impact on the outcomes. With respect to the SSIM outcome, again tests 1-4 and 9-12 give the best improvements. In contrast, tests 2-4, 10 and 12 have the highest SSIM values (SSIM>> 0.7). Tests with even numbers apply $BS(+1)$, so 2, 4 10 and 12 all use 20 px rolling ball radius and this factor improves both outcomes. In addition, test 4 applied intensity normalization *Norm* (level +1, 0.4% of saturated pixels) and experiment 12 applied image intensity normalization followed by median filter *Med*. Figures 5.3 and 5.4 show the magnitude of the effect of each factor in the outcomes, and it confirms that increasing the rolling ball radius of the background subtraction has a positive effect on the outcomes, regardless of the order in which it is applied within the enhancement operations. The second highest positive effects came from the pairwise interaction of the factors $Norm$ and Fra and the three-factor interaction $BS : Norm : Fra$, although such effects do not give the maximum possible outcome values (see the outcomes of experiments 7 and 8 in Figure 5.1, representing $Norm : FRA$ and $BS : Norm : Fra$).

The first experiments do not show differences in the outcomes when the order in which the enhancement operations applied changes. This occurs due to the nature of our experimental design, in which -1 factor levels indicate that certain operations are not applied to the image. When other factors are used (i.e. as indicated by level +1), the differences in the outcomes appear between tests that applied the enhancement operations in different order, however the orders do not have more significant effects than the factors themselves. In any case, orders 1 and 2 improve the outcomes compared to orders 3 and 4 (ORD_{median} is more significant than ORD_{Norm}). Therefore, if the median filter is used, it is better if it is the last operation to be applied to the image.

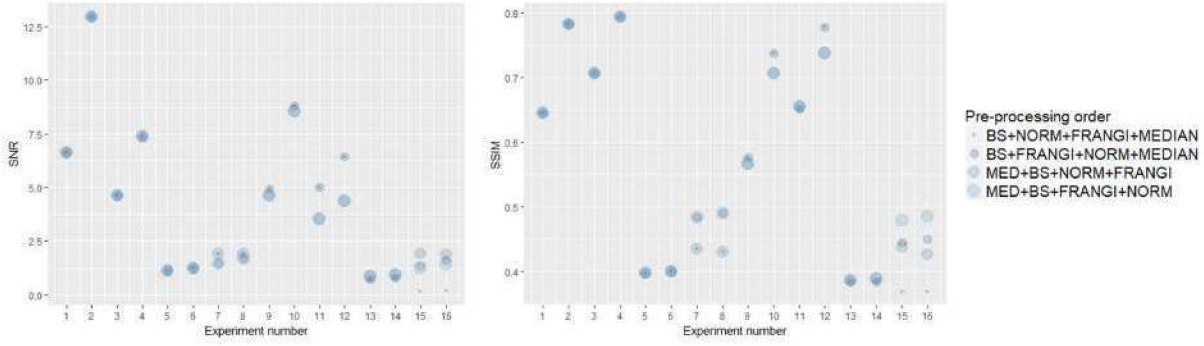

Figure 5.1: Result of the SNR and SSIM parameters after performing the factorial experiments for the Glu sample image.

The tests with the PGal sample image show that the enhancement operations have different effects on the image compared to the Glu sample image. Figure 5.2 shows that the outcomes of SNR and SSIM vary greatly, for example between experiments 1-2 and 3-4 or 11-12 and 13-14, at every two tests. This occurs exactly when the level of the factor $Norm$ varies.

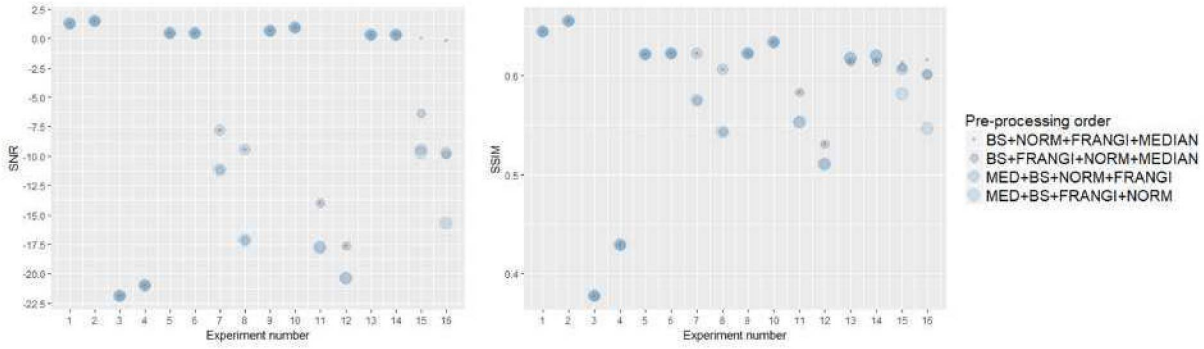

Figure 5.2: Result of the SNR and SSIM parameters after performing the factorial experiments for the PGal sample image.

Thus, it is clear that using $Norm$ has a negative impact on the SNR and SSIM outcomes. As was the case with the Glu image, background subtraction again improves the outcome, although the effect of increasing the rolling ball radius from 5 px to 20 px is less significant than it was for the Glu sample image. Other significant effects are of the pairwise combination of $Norm$ and Fra when Normalization is applied before Frangi vesselnes (Orders 1 and 3) and $Norm$ and Med, when the median filter is applied after normalization (Orders 2 and 4). Regardless of these significant effects, background subtraction alone still best result for both outcomes.

The order of the pre-processing operations is slightly more important for the PGal sample image than for the Glu sample image. It is not particularly clear whether one order is more important than the other, but it appears that ORD_{Norm} is more significant. In general, the outcomes of the tests 1-8 give higher outcomes than tests 9-16, which suggest that not using median in fact improves the outcomes on most cases. Outcomes of tests 11 and 12 and 15 and 16 also suggest that the normalization order is overall more important than the order of the median and also has higher impact in improving the outcomes.

Given the results of the factorial design tests, we decided that only background subtraction will be applied to both images (Glu and PGal) with a rolling ball radius of 20 px for further evaluation of the biofilament tracing methods.

5.4.2 Tracing results

All images of the glucose and polygalacturonate experiments (all frames) were pre-processed by Background subtraction and then submitted to the biofilament tracing methods. Based on the literature analysis of Chapter 4, we selected 8 methods for testing. However, upon preliminary tests, we have narrowed or method evaluation to only 5 different methods. We excluded Neural Circuit Tracer due to its elevated computational cost and memory issues due to the size of our filament network. As filament segments were traced with Neural Circuit Tracer, the speed of the method slowed down until the time taken to trace a short segment approximately 15 px was longer than a few minutes. FarSIGHT Snake and TreMAP were excluded due to issues on the implementation, bugs that crashed the implementation. Appendix B provides details about the parameters used in the testing of the 5 remainin methods and Appendix C shows snapshots of the tracing results of all the methods and the different parameters used. For the snapshots, Vaa3D visualizations were used (Peng et al., 2010b).

The APP (Peng et al., 2011) method, available as a Vaa3D implementation, managed to trace most of the mycelial network in the Glu experiment and a very small portion of the network in the PGal experiment. The tracing results show a great number of spurious short branches and, in some cases, and square-like filament paths, which did not exist in the real mycelium.

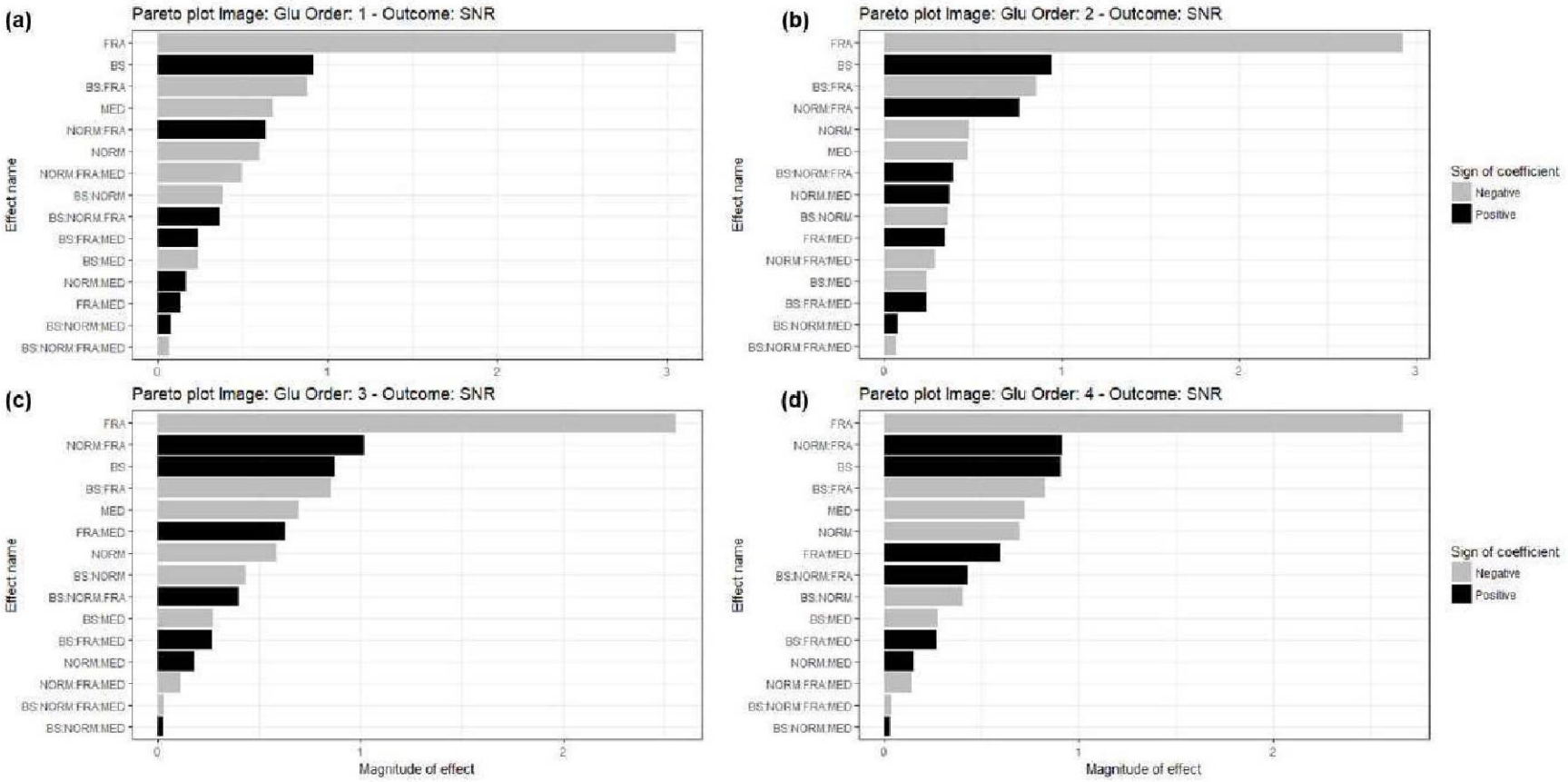

Figure 5.3: Pareto plot of the magnitude of the effects of each factor for the Glu sample image and SNR as outcome and order 1-4 (a-d).

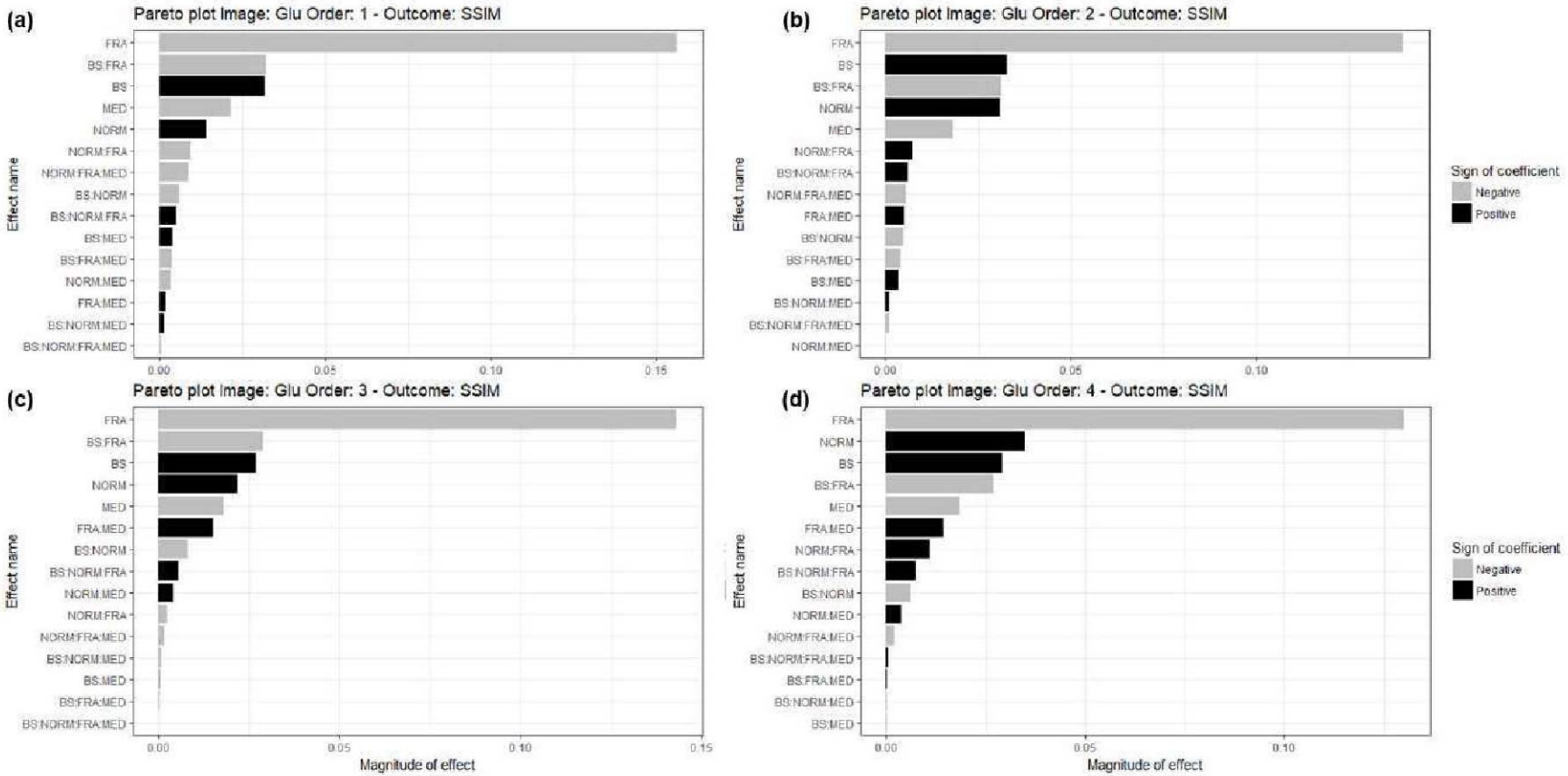

Figure 5.4: Pareto plot of the magnitude of the effects of each factor for the Glu sample image and SSIM as outcome and order 1-4 (a-d).

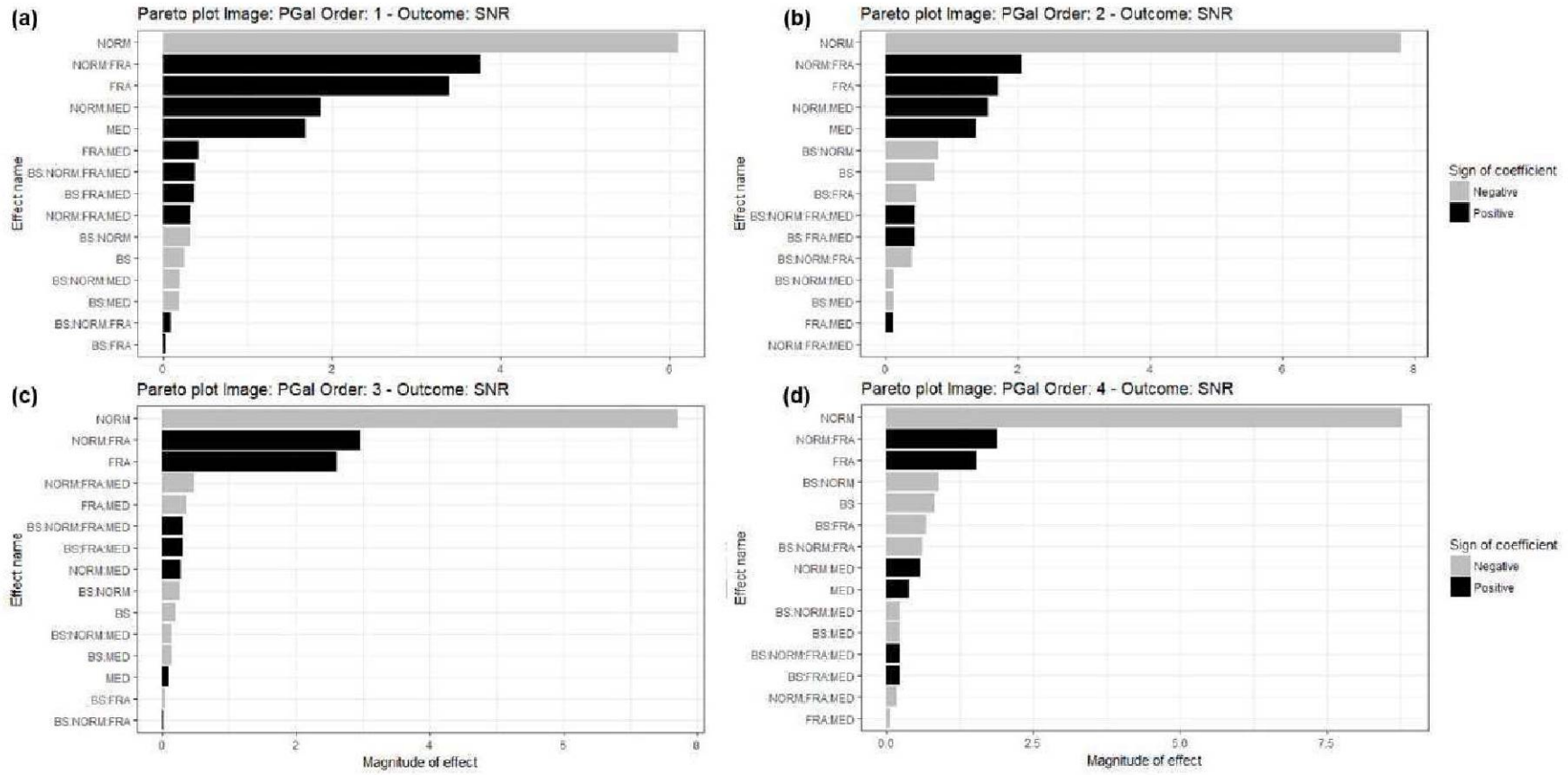

Figure 5.5: Pareto plot of the magnitude of the effects of each factor for the PGal sample image and SNR as outcome and order 1-4 (a-d).

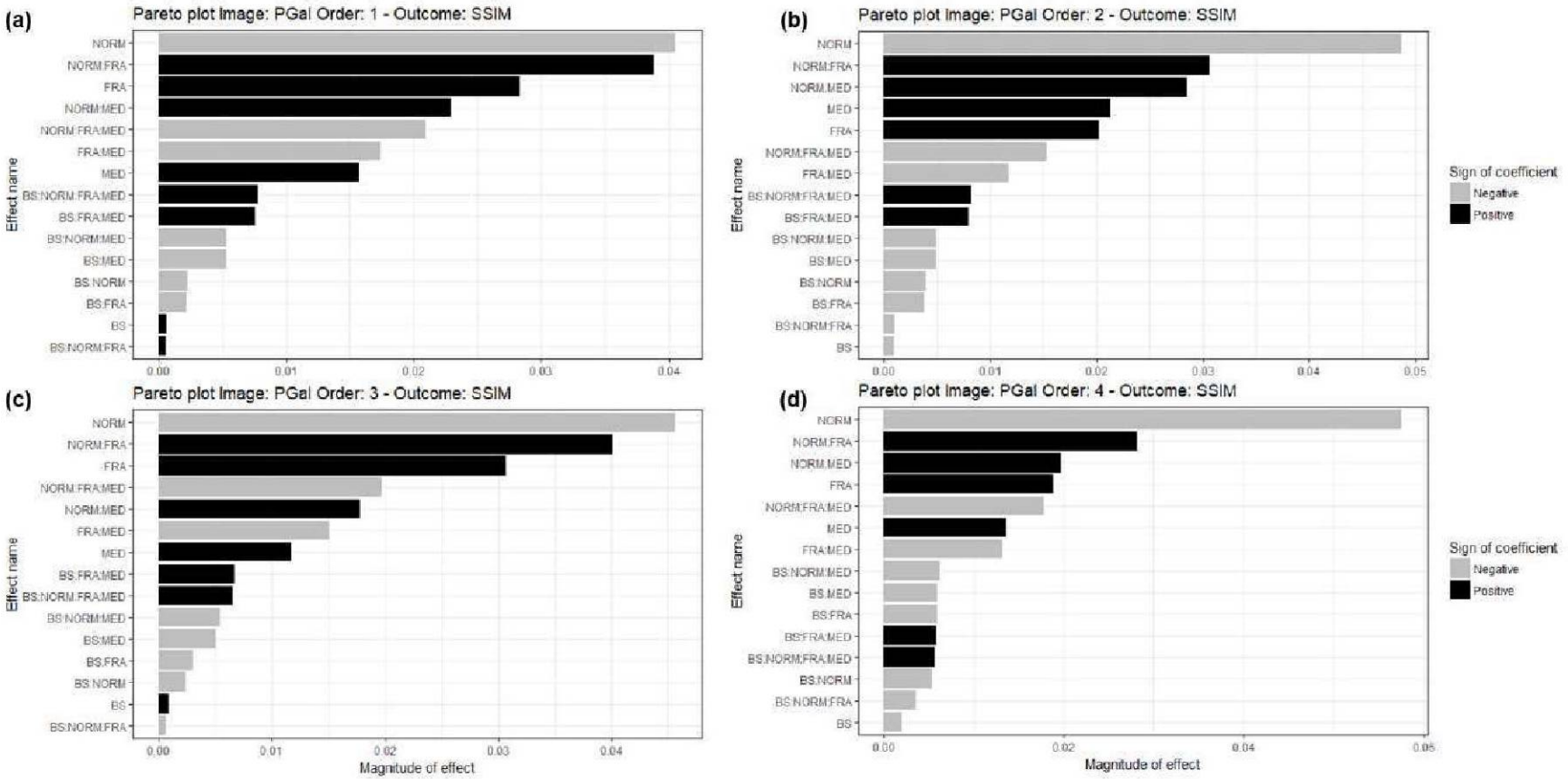

Figure 5.6: Pareto plot of the magnitude of the effects of each factor for the PGal sample image and SSIM as outcome and order 1-4 (a-d).

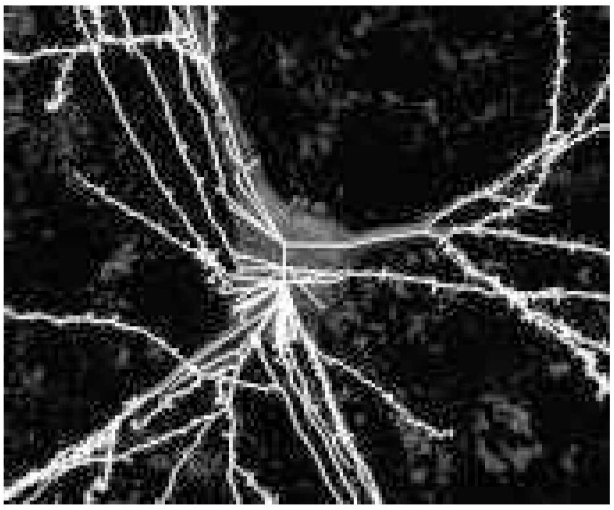

Figure 5.7: Sample of the final centrelines shown as white lines within a neuron volume-rendered dataset. Reprinted from Journal of Neuroscience Methods, 184/1, Rodriguez, A., Ehlenberger, D., Hof, P., Wearne, S. L., 2009, with permission from Elsevier.

However, the APP method was quite fast in performing the tracing and did not take longer than 2 minutes. APP could be the method of choice if the original image were of better quality or more robust post-processing methods were developed to remove the spurious branches and smooth the square-like filament sections.

The NeuronStudio method (Wearne et al., 2005; Rodriguez et al., 2008, 2009) also managed to detect and trace most of the mycelial network in the Glu experiment and only a small portion of the network in the PGal experiment. NeuronStudio did the tracing in less than 30 seconds. The problems with the tracing results are the irregular topology and disconnected filaments. In cases where the intensity of filaments was faint (specially in the PGal experiment) the tracing ceased and sometimes reinitiated a few micrometers further on as a new filament. In addition, in areas with dense population of filaments, the filaments were poorly detected. This issue could be difficult to solve since it is probably related to the theoretical approach used to trace the filaments, wich uses Voxel scooping from the thresholded image. The threshold on areas with dense population of filaments would cause the region to be identifies as a single 'blob' instead of a bundle of filaments, then the resulting traces would look like Figure 5.7, that shows the center of a neuron tracing.

APP2 (Xiao e Peng, 2013) did not trace the mycelial network properly and did not properly detect filaments in regions with densely packed filaments or regions with faint filaments (filaments with slightly lower voxel intensity). The diameter of the traced filaments varied more than the other methods, which shows that APP2 could be more sensitive to changes in the diameter of the filaments. Although such sensitivity could be good in some cases, it is known that the filament diameter or vegetative hyphae of *A. niger* does not vary greatly and is fairly homogeneous throughout the mycelium (4 pixels or 4.94 μm, based on our observations of high resolution images). Thus, this variation in the diameters is not expected. A potential reason that could have caused the variations is that our images show the hyphae almost at the resolution limit and the pixel intensities in the cross section of the hyphae vary significantly because there is only 3-5 pixels in a regular cross section. Also, it can be noted that the topology and path of the traced filaments do not follow what is expected: filaments leaving the surface of the solid substrate (region with highest density of hyphae) going either downwards to the solid substrate or upwards to the gas phase. We observed traced filaments that followed the opposite patterns. With respect processing time, APP2 provided the results always in less than a few seconds.

The NeuroGPS-Tree (Quan et al., 2015) did not manage to detect the complete mycelial network (we suggest via visualization that only about 30-40% of the network was traced for the Glu experiment and 5-10% for the PGal experiment). However, we performed the tracing without defining any seed point and the method allows the definition of a list of seed points from which the tracing initiates. The lack of seeding could be responsible (at least in part) for the poor tracing. By default, if no seed points are given, NeuroGPS-Tree detects a starting point. The topology of the network appears to be fairly correct in the dense areas, but in extremities the tracing becomes unlike what would occur naturally. Finally, the diameter appear to be overestimated, but the quality of our image may have made it difficult to determine the diameter with accuracy since the filament diameters range from 3-5 voxels. NeuroGPS-Tree is still a potential candidate method if the parameters are tested more exhaustively and a list seed points is provided. NeuroGPS-Tree appears to be useful due to its simple parameters: threshold value, trace value and linear enhance value.

The method that provided the most promising and visually accurate results was NeuTube (Feng et al., 2015) for both experiments and it was the only one capable of detecting the greater part of the mycelial network in both images. In addition, the time to perform the tracing was usually less than 5 minutes. Figure 5.8 show two examples of the tracing results provided by NeuTube. Although parts of the tracing indicate filaments that are slightly straighter than those visible in the original images and some dense regions that show the tracing did not quite overlap the filaments in the original image, the topology and the diameter of the traced filaments also suggest that this is the most accurate method for our images. Thus, we selected NeuTube for the computation of the morphometric parameters.

5.4.3 Morphometric parameters

Based on the qualitative evaluation of filament tracing methods, we used the Neutube method (Build 1.0z.2017.01 Windows 64-bit) to obtain graph representations of our sample images. The parameters used as input in NeuTube to extract the filament network can be found in Appendix D. With the .swc files of each experiment and its frames, we obtained the morphometric parameters presented in section 5.3

The growth and morphometric parameters were computed only for the frames that contained hyphae: four frames for Glucose (14.25, 18.25, 22.25, and 26.25 h) and 5 frames for Polygalacturonate (12.5, 15.33, 18.17, 21.00, and 23.83 h). Figures 5.9 and 5.10 show the biomass density profiles for growth on glucose and for growth on Polygalacturonate, respectively. For growth on glucose, the peak biomass density is located exactly at the substrate surface and in PGal the peak biomass density is below the substrate surface. Throughout the experiments, the fungus occupied more volume on glucose than on polygalacturonate. The distribution of biomass in space was distinctively different: On glucose, the fungus grew both in the gas phase and the solid (agar) phase, whereas on PGal the fungus grew mainly within the solid phase. This different behaviour of the fungus on PGal is unusual.

Aerial biomass and penetrative biomass density profiles of the growth on glucose show that mainly aerial hyphae grow in the first moment, as observed at the 14.25 h profile. Later, penetrative hyphae grow and the density of penetrative biomass increases significantly from 18.25 to 22.25 h. The last measurement at 26.25 h indicates that penetrative biomass has reached its final value because there is only a small increase in its volume fraction in specific regions, for example from 10 to 100 μm. There are also areas that show a decrease of biomass density. This is not caused by any biological activity of the fungus, such as autolysis, but rather by errors of the filament tracing method. In some cases, the filament tracing method may have failed to detect

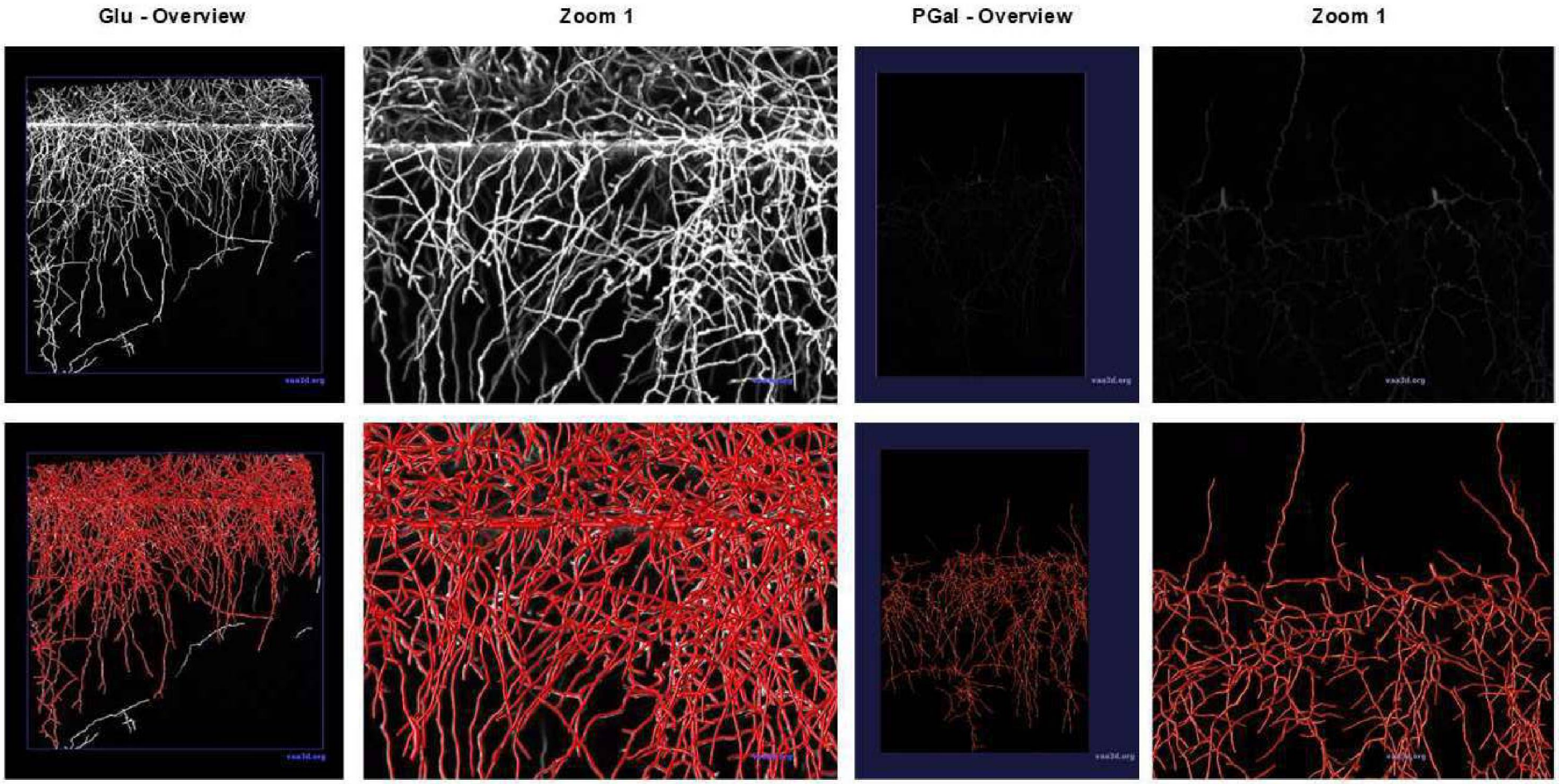

Figure 5.8: Two examples of the tracing results provided by the Neutube method.

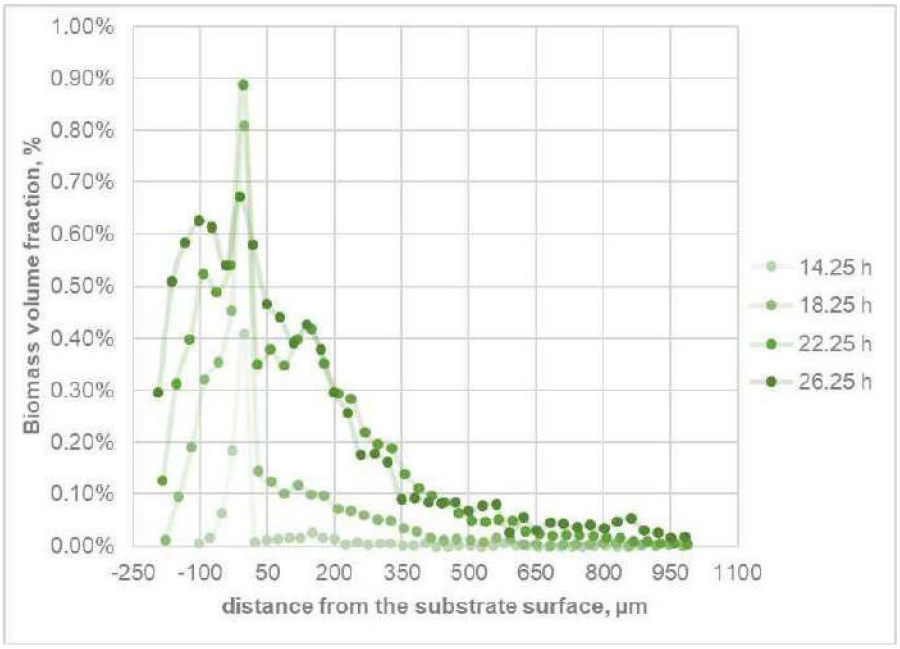

Figure 5.9: Biomass density profiles as a function of the distance from the substrate surface for *A. niger* on glucose. The negative sign indicates positions above the substrate surface, whereas positive signs indicate positions below the substrate surface.

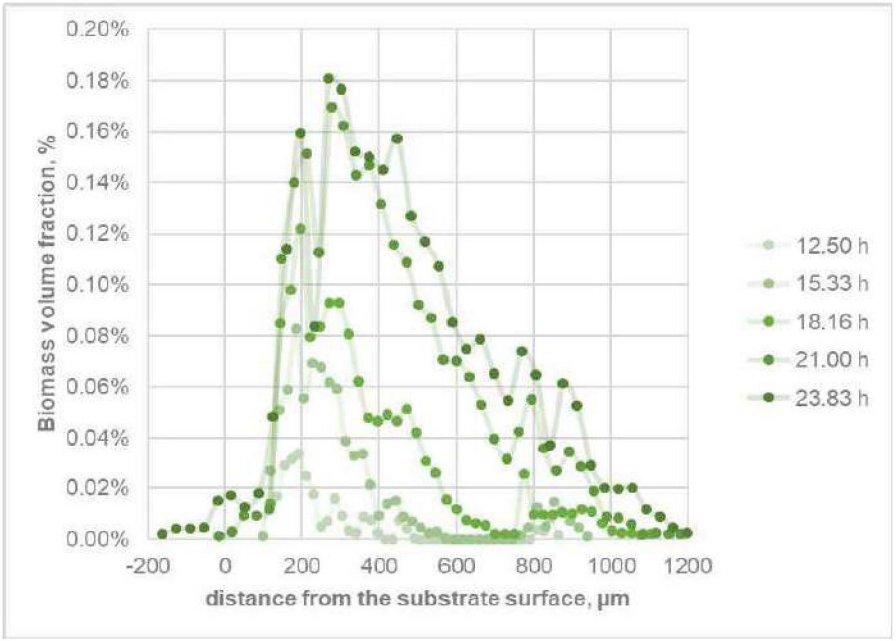

Figure 5.10: Biomass density profiles as a function of the distance from the substrate surface for *A. niger* on polygalacturonate. The negative sign indicates positions above the substrate surface, whereas positive signs indicate positions below the substrate surface.

some of the single hyphae (see section 5.5 and Figure 5.11) In the PGal experiment, the results of the first hours of growth show a growth behaviour similar to fungal growth on glucose. Later, the

growth of penetrative biomass increases greatly. However, it appears that the penetrative biomass could still grow, because the differences in biomass density existed on all durations, as opposed to the growth on glucose at 22.25 and 26.25 h, which had a somewhat stable penetrative biomass density profile.

With respect to the maximum depth and height that biomass reached in the experiments, the mycelium reached depths up to 950-1000 μm on Glucose and 1200 μm on Polygalacturonate.

There is significantly more biomass on Glucose than on PGal. On glucose, biomass densities ranged from 0.0% to 0.9%, whereas on PGal they ranged from 0.0% to 0.2%. The major reason for that is the initial number of spores in the field of view. In the Glucose experiment, at least 54 spores were visible at the beginning of the experiment. On the other hand, there were only 20 spores (or fewer) at the beginning of the PGal experiment. For this reason, it is not yet worthwhile to draw any conclusions from the data about the effect of the carbon source on biomass density. In order to do this, one would need to ensure a similar inoculation density. Other differences are better seen with the computed parameters on Table 5.4 and Table 5.5.

The total length of the colony reached a maximum of 141.52 mm on glucose at 26.25 h and 47.52 mm on polygalacturonate at 23.83 h. By simple linear interpolation, at 23.83 h the mycelium on glucose would show approximately 81 mm total length. The increased total length of the colony might be explained by the increased number of spores at the beginning of the experiment. However, observing the total length during the whole experiment, it is difficult to define whether the spores first develop hyphae on polygalacturonate or glucose, as significant number hyphae is already visible in the first frame taken during growth on PGal (at 12.5 h) and between 10.25 (first frame, where no hyphae ware detected) and 14.25 h on Glucose. Glucose can be readily uptaken by the microorganism and is considered a better carbon source than polysaccharides such as starch and polygalacturonate (Sati e Bisht, 2006; Jonathan e Fasidi, 2001), so the spores would first develop in the glucose medium as opposed to polygalacturonate. In order to absorb the galacturonic acid derived from the polygalacturonate, the fungus would require to produce and secrete specific hydrolytic enzymes to the environment, and then these enzymes would catalyse the reaction of hydrolysis of polygalacturonate to galacturonic acid. Then, finally the fungus would be able to absorb these nutrients and grow. Further investigation is required in order to obtain the kinetics of polygalacturonase secretion and the kinetics of polygalacturonate hydrolysis and absorption of galacturonic acid or glucose by the fungus.

The highest colony extension rate on glucose, of 30-35 $mm.h^{-1}$, was 10-fold higher than that obtained on polygalactutonate. In contrast, the average tip extension rate indicates that the fungus has fewer tips on polygalacturonate, but these tips extend at higher rates on glucose. On glucose, the first and last measurements of the number of tips were 199 and 1899, and 5.18 and 18.63 μm.h^{-1} for tip extension rates. For the PGal experiment, the first and last measurements of the number of tips were 25 and 533 and 6.40 and 31.46 μm.h^{-1} for tip extension rates. The first measurement of tip extension rate for the Glu experiment (10;25 h) is low but the real value might be greater, because the previous frame at 10.25 h does not show spore swelling and the appearance of germ tubes. So it is probably the case that the first hyphae appear later, and the actual time difference is smaller. The same occurred with the first measurement of tip extension rate of the PGal experiment, and the value might be even more underestimated since the first frame was obtained at 12.5 h, so the hyphae could appear any time between a few hours growth and 12.5 h. It is impossible to determine the exact time the first hyphae appear with our images, because of the long time interval between image acquisition.

Table 5.4: Growth and morphometric parameters for the growth of *A. niger* on Glucose.

Growth duration, h	14.25	18.25	22.25	26.25
Colony total length, mm	10.31	52.85	125.04	141.52
Colony extension rate, $mm.h^{-1}$	1.03	13.21	31.26	35.38
Colony length percent incrase, %	NA	412%	137%	13%
Number of tips	199	574	1522	1899
Tip extension rate, $\mu m.h^{-1}$	5.18	23.02	20.54	18.63
Hyphal Growth Unit (HGU), µm	51.82	92.07	82.16	74.52

Table 5.5: Growth and morphometric parameters for the growth of *A. niger* on Polygalacturonate.

Growth duration, h	12.50	15.33	18.17	21.00	23.83
Colony total length, mm	2.00	7.74	16.57	34.91	47.515
Colony extension rate, $mm.h^{-1}$	0.16	0.50	0.91	1.66	1.99
Colony length percent increase, %	NA	287%	114%	111%	36%
Number of Tips	25	53	126	346	533
Tip extension rate, $\mu m.h^{-1}$	6.40	51.59	46.37	35.60	31.46
Hyphal Growth Unit (HGU), µm	80.06	146.01	131.52	100.90	89.15

5.5 Discussion

5.5.1 Using factorial design to evaluate pre-processing methods

This work represents the first time that a factorial design has been used to evaluate image enhancement methods. Such factorial design approach is useful when there are images of poor quality and it is necessary to choose a set of image enhancement operations and the order in which they are applied to improve the quality of the image or improve the quality of the image analysis results. The methodology can test various enhancement methods, their combination and order of application.

Despite the usefulness of our methodology, there is room for improvement. For example, the tests were evaluated based on the SNR and SSIM values, although they may not always reflect in actual improvement of the final tracing results. One example is the specific case of the Frangi vessel enhancement method, where the structure of the mycelial network changes, since Frangi results do not enhance branching points in the image. Therefore, such structural change in the image of the mycelium will provoke a reduction in the SSIM value. It is necessary to verify whether this change of the structure affects the biofilament tracing methods, and this will depend on the theoretical approach of each method. SNR is a measure of how noisy the image is. Then, an enhancement operation will be evaluated by enhancement method that is not used to reduce noise is image intensity normalization. In image intensity normalization, the result of normalization in a noisy image will be another noisy image with the noise potentially intensified. For this reason, other potential improvement would be to have ground truth annotations of the final tracing results and test the pre-processing approaches followed by filament tracing and actually evaluate the effects of each enhancement operation on the real outcome (accuracy and precision): the final tracing results.

Apart from full factorial experimental designs, other types of screening factorial designs are possible and allow the testing of as many enhancement operations as one likes, for instance the Plackett-Burman factorial design for factor screening. The Plackett-Burman factorial design

of 12 tests allow screening of up to 11 factor with only 12 tests. Another possibility would be to add a second factorial design to optimize the parameters of the enhancement operations, after an initial factorial design like the one undertaken in the current work.

5.5.2 The first detailed tracing of the three-dimensional growth of a mycelial filament network in a complex heterogeneous environment

The results presented here show that biofilament tracing methods can be used to extract morphometric data from images of the growth of filamentous fungi in complex environments. However, the sample preparation, image acquisition and capabilities of the biofilament tracing methods need to improve before results could help drawing more concrete conclusions about the growth and morphology of the fungus. These three aspects are discussed below.

- *Sample preparation* - The results show that the mycelium that grew in PGal has peak biomass density below the substrate surface: The irregular surface of the substrate may have been the cause of this result. With an irregular substrate surface, it is difficult to define a clear boundary between the air phase and the solid phase.

  During the experiments, it was difficult to maintain the surface of the substrate perfectly even and perpendicular to the glass dish. It is important to keep the substrate surface perpendicular to the glass dish to have the surface of substrate lying in the xz plane of the image. Otherwise, it would be necessary perform additional operations such as image rotation. Another difficulty during the sample preparation was keeping the other surfaces sterile and not moving spores to undesired areas (even pushing them within the solid substrate) and avoiding the growth of spores in regions that were no the surface of the substrate of interest. If other surfaces have spores and they develop during the experiment, the measurements of biomass density profiles will be affected. In order to have proper estimation of biomass density profiles, the spores must grow on one surface only.

- *Image acquisition* Our datasets were challenging because of the image characteristics (see Appendix E for details). For example, the low contrast of the images (part of it due to the nature of the fluorescence imaging techniques), which make the filaments have voxel intensities near the background intensities, and the unimodal voxel intensity distribution.

  In addition to the low contrast and unimodal intensity distribution, three issues come with the limitations of the CLSM microscope and the size of our sample. First the length covered by the images in the z axis was of approximately 150 μm, which is at the limit of the confocal capabilities. Second, the image intensities decrease as the z stack increases (the objects are farther away from the glass dish and the microscope detector). This is visible when visualizing the 3D volume in the yz or xz planes and is potentially due to the axial limitations of the microscopy and the opacity of solid substrate region and the dense population of hyphae as growth occurs. The last issue is that the filament sizes, in voxels, are close to the voxel resolution and this makes the filament detection potentially more difficult and, in addition, will result in higher errors in the computation of the filament diameters (visually, there is no great change in diameter, but due to problems with resolution, the filament tracing method attributes diameters that vary from 3 to 5 voxels).

Finally, we obtained images at times that were quite distant (2.83 h and 4 h). In order to increase accuracy of the morphometric calculations and the number of data points of a single experiment, it would be better to decrease the time between the acquisition of each frame.

Although we improved the image quality to some extent through background subtraction, image quality could be further improved by making changes to the image acquisition settings. We suggest the following modifications:

- a slight reduction in the field of view, say, of 10-20% in the xy plane, to cover an area of 0.9 mm^2 to 1 mm^2 (our experiments covered 1.44 mm^2 area in the xy plane). This reduction still would show several hyphae and would reduce the time of the frame acquisition. This is an initial suggestion, but a more detailed study can be done on the trade-off between the size of the field of view and the number of detected hyphae that is sufficient to compute comprehensive morphometric measurements;
- an increase in pixel resolution from 1.2361 μm/px to <1.000 μm/px. This modification would increase the time of the frame acquisition but it is important to facilitate filament detection and reduce errors in the diameter estimation.
- an experiment only with only one or two fungus samples each time (the experiments we performed were run with 3 samples at each time. this will will make it possible to acquire more frames per sample(by 66% or 33%);
- a decrease in axial resolution to 1.000 mum/px or near, but at the same time a reduction in the number of axial stacks in the image from 76 to 50 or less. This will reduce image anisotropy by making z resolution similar to the xy resolution and also minimize the effects of the faint axial stacks.

- *Biofilament tracing capabilities* errors in filament detection need to be solved to increase the accuracy of the results. Figure 5.11 indicates three potential cases of filament detection errors.

  We suggest that the analysis of the tracing results must involve complete benchmarking efforts and quantitative metrics. In order to achieve that, a collective effort to annotate and obtain ground truth datasets is needed. The fungal biology community and also the other research areas that use biofilament tracing methods could create a sample dataset database to be used for benchmarking the filament tracing methods. In addition, filament metrics such as DIADEM metrics (Gillette et al., 2011) or Netmets (Mayerich et al., 2012) must be used to evaluate the tracing results against the data annotated by specialists.

5.6 Conclusion

The present work presents the first attempt to perform a detailed three-dimensional time-lapsed tracing of the growth of a filamentous fungus in a complex growth environment. Our approach shows great potential for the acquisition of morphometric and growth dynamics data of the fungus at the scale of the mycelium that will support research in fungal growth. Our work provides a base for further developments in the study of fungal growth in complex environments and our suggestions may guide other research groups to use our approach as a whole or parts of it (image acquisition procedures, factorial design to test enhancement operations, preliminary tests of

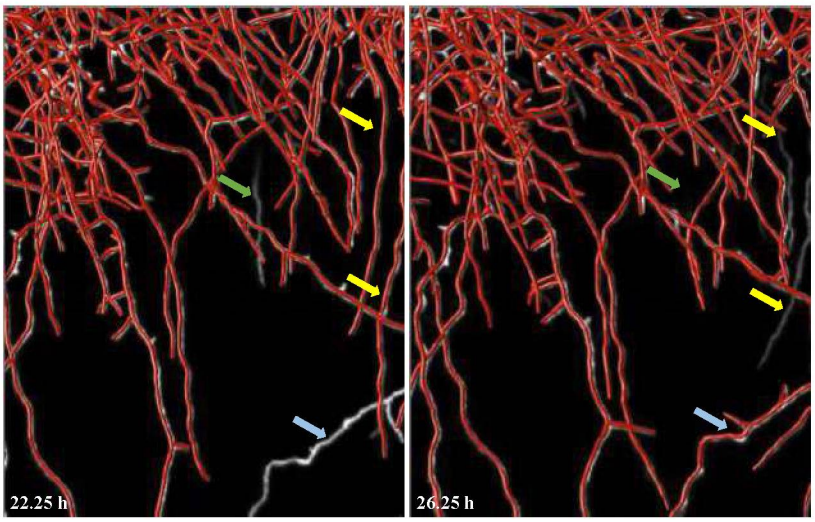

Figure 5.11: Filament detection errors in the glucose experiment. The images shown are of the maximum intensity projections (MIP) of the image stacks (filaments in white/grey) overlaid with the filaments detected by the Neutube method. There are three cases of filament detection errors: (i) If the filament tracing method fails to detect filaments that existed in previous frames (yellow arrows), the measured biomass density may decrease. (ii) In case the filament detection fails to detect a filament in a previous frame but detects it in the next frame (blue arrows), there will be a higher difference in biomass density between frames, where the difference is lower, but the biomass still increases over time. (iii) There may be a filament that appeared in the image in one frame that did not appear in the next frame (green arrow). In this case, there are two possibilities, it was either detected then undetected (because it did not appear) or undetected (when it should have been detected) in both frames.

biofilament tracing methods and our library to calculate morphometric parameters) and develop more advanced microscopy techniques coupled with image analysis with biofilament tracing methods to extract morphometric and growth dynamics data.

6 General discussion

In this chapter we discuss some of the main contributions of this work, the visibility of the project and future prospects.

6.1 Improving sample preparation and image acquisition set-up

In chapter 5 a discussion was presented about the fact that the sample preparation technique and image acquisition set-up could be improved in order to obtain images with better quality for further image analysis. With respect to the sample preparation technique, the methodology used during the doctoral works of Sugai-Guérios (2016) needs to be improved since the technique requires a high level of skill during the step in which the sample needs to be excised and positioned with the inoculated surface of the solid substrate perpendicular to the glass dish. Nopharatana (1999) used a different sample preparation technique in her study. However, when she analysed the growth of the mycelium above the substrate surface (aerial hyphae), a different sample preparation technique was proposed. She prepared the culture medium and inoculated it within a small *plastic box* (type or brand not specified by the author). For observation under the microscope, there was no need to excise the sample and place it in another dish, the plastic box was just positioned in the microscope such that the surface was perpendicular to the microscope sample stage. Another problem the effect of the gravitational forces on the hyphae growing above the substrate surface must be taken into consideration. The spatial position of the hyphae on all experiments performed by Sugai-Guérios (2016) and Nopharatana (1999) may be affected by gravity and interfere with the analysis of their spatial distribution. The spatial distribution of the hyphae might not reflect the spatial distribution that one would expect for aerial hyphae of a mycelium cultivated on a substrate surface that is parallel to the ground. In this work, this may not have a severe impact on our results as our analysis of the biomass spatial distribution was performed as a function of y coordinate (in a system in which the gravitational force acts along the direction of the z coordinate), but this issue must be solved in case more complete studies are to be performed. Apart from the proposed techniques of these doctoral studies of Sugai-Guérios (2016) and (Nopharatana, 1999), it is possible that other areas, plant imaging for example, may have already developed sample preparation techniques that take into account that the gravitational forces in the sample.

Apart from the discussion on the improvements of the sample preparation, we also suggested four main changes in the image acquisition stage (detailed in chapter 5). Apart from the suggestions on Chapter 5, another possibility for improvement is to test other microscopy techniques, such as 2-photon confocal microscopy (Denk et al., 1990) and light sheet fluorescence microscopy (LSCM) (Reynaud et al., 2008). They are more appropriate techniques for *in vivo* imaging. Given the quality of the final tracing results of this project, a decision was made not to draw any concrete conclusions about the growth of *A. niger* on solid substrates. However, with any slight improvements on image quality, the tracing results will potentially improve and make

the analysis of the results more reliable, therefore having more impact on the research results. Also,it will be important to obtain quantitative measurements such as ground truth annotations to validate the results. This way, we may acquire more quantitative morphometric and growth dynamics data of the growth of filamentous fungi to support our experimental research as well as the development of mathematical and computational models of the growth of filamentous fungi.

6.2 Efforts towards extensive benchmarking of biofilament tracing methods

The present work could be the beginning of an effort to perform an extensive benchmarking work of biofilament tracing methods. The literature of these different research areas (neurons, blood vessels, cytoskeletal structures, among others) provides many image analysis methods for biofilament tracing, as our literature analysis showed 4. From our point of view, it made sense to analyse of the literature of biofilament tracing methods that included some of these areas together, because the filamentous structures have similar features regardless of what it is. This way, it was possible to have a better overview of what are the actual the state-of-the-art biofilament tracing methods and noticed that there has to be more communication and data exchange between these different research areas working with biofilaments, since there were differences between what were the state-of-the-art methods in each area.

6.3 Future prospects

6.3.1 Proposal of future academic projects

Chemical Engineering / Biochemical engineering

- Evaluation of morphometric and growth dynamics parameters and their relevance for the development of mathematical and computational models that describe fungal growth. Explore the literature of fungal growth models and identify the most used parameters for their development. Observe what type of parameter is used for each type of model based on the model classification from the literature review of Sugai-Guérios et al. (2015).

- Experimental study for the evaluation of the effect of the nutrient source, the culture medium hardness and the inoculum concentration on the growth and morphology of filamentous fungi using advanced microscopy techniques and biofilament tracing methods. The study could involve testing fungal growth on glucose, galacturonic acid, polygalacturonate and starch in different concentrations. For each nutrient source and concentration, different spore inoculum concentrations could be tested: low, with only one spore in the image, medium, from 5 to 15 spores and high, more than 15. Additionally, for all experiments it would be very important to develop a technique to determine the hardness of the culture medium, since it could vary with each nutrient source as well as vary with the concentration of the nutrient source. It appears that the hardness of the culture medium may affect the maximum possible depth of the growth of penetrative hyphae as Sugai-Guérios et al. (2016) suggest. This study would be a valuable source of insights into the growth and the morphometric and growth dynamics data extracted from all the images would be capable of serving as input for many fungal growth models.

Microscopy and experimental biology

- Evaluation of sample preparation techniques and different microscopy techniques (2-photon and light sheet fluorescence microscopy) to improve experiment execution time and discover the trade-off between high-quality image acquisition and the size of the detected mycelium that is sufficient for further image analysis of filamentous fungi growing on solid substrates. Upon a quick search in the literature, a few potential sample preparation protocols were found (von Wangenheim et al., 2017; Maizel et al., 2011). These protocols are simpler than the one used by Sugai-Guérios (2016) and allow samples of plants to be put vertically in the microscope, in a way such that the gravitational forces acting in the plant are in the same direction as they would be in a real environment. Other improvements would come from testing the capabilities of the 2-photon and light sheet fluorescence microscopy, which are more suitable techniques for *in vivo* imaging of thick specimens (Denk et al., 1990; Reynaud et al., 2008).

Computer Science

- Development of a new biofilament tracing method. The aim would be to propose an improved biofilament tracing method based on previous literature analysis and our preliminary evaluation of filament tracing methods. In order for the method to have high impact and be visible, relevant and accessible to the community, source code in open repositories and implementations available for the most widely used packages (for example ImageJ, matlab, itk and openCV). The method should be exhaustively tested on sample images and have a user-friendly implementation with detailed documentation on its use. Suggestions of potential methods as starting points to improve upon are NeuTube(Feng et al., 2015), Tubular Geodesics (Sironi et al., 2016; Türetken et al., 2012; Benmansour e Cohen, 2011) and Neural Circuit Tracer (Gala et al., 2014; Chothani et al., 2011). For the latter, major improvements in memory allocation and computational speed are required.

Interdisciplinary and potentially interinstitutional projects

- Computational simulations of the growth of filamentous fungi. Many approaches are possible as soon as reliable and accurate results are available:
  - Obtain a mesh file format of a section of the mycelial network and use it to simulate internal fluid flows with Computational Fluid Dynamics, further modifications on the strain may be needed to provide additional information about objects of interest within the cytosol/cytoplasm, for example vesicle transport or nutrient absorption. A model that can reproduce a mycelium in 3D in a complex environment based on considerations of mass transfer and hyphal growth would be a big step towards the simulation of the key phenomena involved in fungal growth and the real three-dimensional complexity of the growth.
  - Develop a more specific computational model to represent the real growth of the fungus in 3D space over time. A potential direction to take would be to develop a graph generation model. Some preliminary work has been done towards that: our research group is improving the layer model developed by Sugai-Guérios et al. (2016) to make it possible to represent the hyphal segments as edges of a graph. However, the project would benefit from a collaboration with computer science researchers because of their expertise in the field of graph theory.

- Develop a strategy for the benchmarking biofilament tracing methods. Activities could involve: (i) creation of a database of ground truth datasets, (ii) specification of the metrics to be used for benchmarking, (iii) development of an ontology or use of existing ontologies to describe meta-data of the datasets, (iv) development of a web-based implementation or standalone implementation to execute the biofilament tracing methods to be benchmarked and (v) execution of the detailed analysis and comparison of the methods.

7 Conclusions

It was possible to achieve all the objectives defined for this masters project. We managed to evaluate the quality of our images and suggest that modifications in sample preparation and in the set-up of the image acquisition are needed. In addition, the results and discussions in this document indicate many possibilities of future projects and research improvements in the many aspects that this highly interdisciplinary research touches: chemical/biochemical engineering, microscopy and bioimage analysis (computer science).

We developed a classification methodology to better understand the literature of biofilament tracing methods (Chapter 4. This classification was expanded from existing and well known reviews and was useful for the purpose of understanding the patterns and combinations of the theoretical approaches used to solve the filament tracing problem, although that is true, in order to make the ontology to be more useful and precise, its development require the input and discussion of many researchers in the area so a common ground of terms and definitions can be defined.

Our literature analysis approach using graph theory and a structured classification methodology proved to be simple and useful to deal with great amounts of publications. Despite the fact the selection of article was made manually based on our research interests, this approach to a literature analysis has the potential to be executed in a more automated manner and with greater amounts of data if such approach is implemented using ontology structures and a crowdsourced web-based database of bioimage analysis methods. This, beyond being a step towards a crowdsourced living review of biofilament tracing methods, it is also a step towards dissemination of FAIR (Findable, Accessible, Interoperable and Reusable) data and its principles.

In chapter 5 we evaluated the most common image enhancement methods and initiated an evaluation of existing biofilament tracing methods. Again, our approach to the evaluation of image enhancement methods was different than anything existing in the literature. The use of factorial experimental designs to guide our evaluation and select the image enhancement methods was quite an improvement compared to the common trial and error approach. Although the use of general image quality parameters such as the SNR and SSIM was useful, the results could have shown an ever better outcome if the whole workflow of *image enhancement + filament tracing* was evaluated against ground truth datasets, since the SNR and SSIM outcomes may not necessarily reflect in an improvement in the final tracing results.

The last contribution, also found in chapter 5, relates to evaluating the potential of using existing biofilament tracing methods to obtain detailed tracing results of the complex three-dimensional morphology of the mycelium of a fungus growing in the surface of a solid substrate. Even though our evaluation was still preliminary and qualitative, it can be seen clearly that it is not necessary for researchers in fungal biology and biotechnology to develop a biofilament tracing method from the beginning. Researchers could use existing methods from the other areas and improve and adapt to their specific needs. Regardless of this last argument, we judge that the bioimage analysis community should continue and improve the efforts on

benchmarking of biofilament tracing methods and start building a common database of ground truth data sets of the many different images of biofilaments.

References

Abdul-Karim, M.-A., Al-Kofahi, K., Brown, E. B., Jain, R. K. e Roysam, B. (2003). Automated tracing and change analysis of angiogenic vasculature from in vivo multiphoton confocal image time series. *Microvascular Research*, 66(2):113–125.

Adams, H. L. e Thomas, C. R. (1987). The use of Image Analysis for Morphological Measurements on Filamentous Microorganisms. *Biotechnology and Bioengineering*, 32:707–712.

Al-Kofahi, K., Can, A., Lasek, S., Szarowski, D., Dowell-Mesfin, N., Shain, W., Turner, J. e Roysam, B. (2003). Median-based robust algorithms for tracing neurons from noisy confocal microscope images. *IEEE Transactions on Information Technology in Biomedicine*, 7(4):302–317.

Al-Kofahi, K., Lasek, S., Szarowski, D., Pace, C., Nagy, G., Turner, J. e Roysam, B. (2002). Rapid automated three-dimensional tracing of neurons from confocal image stacks. *IEEE Transactions on Information Technology in Biomedicine*, 6(2):171–187.

Al-Kofahi, Y., Dowell-Mesfin, N., Pace, C., Shain, W., Turner, J. N. e Roysam, B. (2008). Improved detection of branching points in algorithms for automated neuron tracing from 3D confocal images. *Cytometry Part A*, 73A(1):36–43.

Alexopoulos, C., Mims, C. e Blackwell, M. (1996). *Introductory Mycology*. Wiley, 4 edition.

Aylward, S. e Bullitt, E. (2002). Initialization, noise, singularities, and scale in height ridge traversal for tubular object centerline extraction. *IEEE Transactions on Medical Imaging*, 21(2):61–75.

Balmant, W., Sugai-Guérios, M. H., Coradin, J. H., Krieger, N., Furigo, A. e Mitchell, D. A. (2015). A model for growth of a single fungal hypha based on well-mixed tanks in series: Simulation of nutrient and vesicle transport in aerial reproductive hyphae. *PLoS ONE*, 10(3):1–22.

Barry, D. (2010). *Development of novel image analysis methods for the morphological quantification of filamentous fungi*. Tese de doutorado, Dublin Institute of Technology.

Barry, D. J., Chan, C. e Williams, G. A. (2009). Morphological quantification of filamentous fungal development using membrane immobilization and automatic image analysis. *Journal of Industrial Microbiology and Biotechnology*, 36:787–800.

Bas, E. e Erdogmus, D. (2011). Principal Curves as Skeletons of Tubular Objects. *Neuroinformatics*, 9(2-3):181–191.

Bastian, M., Heymann, S., Jacomy, M. et al. (2009). Gephi: an open source software for exploring and manipulating networks. *Icwsm*, 8:361–362.

Basu, S., Aksel, A., Condron, B. e Acton, S. T. (2010). Tree2Tree: Neuron segmentation for generation of neuronal morphology. Em *2010 IEEE International Symposium on Biomedical Imaging: From Nano to Macro*, páginas 548–551. IEEE.

Basu, S., Kulikova, M., Zhizhina, E., Ooi, W. T. e Racoceanu, D. (2013). A Stochastic Model for Automatic Extraction of 3D Neuronal Morphology. Em Mori, K., Sakuma, I., Sato, Y., Barillot, C. e N., N., editores, *Medical Image Computing and Computer-Assisted Intervention – MICCAI 2013.*, páginas 396–403. Springer Berlin Heidelberg.

Basu, S., Liu, C. e Rohde, G. K. (2015). Localizing and extracting filament distributions from microscopy images. *Journal of Microscopy*, 258(1):13–23.

Basu, S., Ooi, W. T. e Racoceanu, D. (2016). Neurite Tracing With Object Process. *IEEE Transactions on Medical Imaging*, 35(6):1443–1451.

Basu, S. e Racoceanu, D. (2014). Reconstructing neuronal morphology from microscopy stacks using fast marching. Em *2014 IEEE International Conference on Image Processing (ICIP)*, páginas 3597–3601. IEEE.

Benmansour, F. e Cohen, L. D. (2011). Tubular Structure Segmentation Based on Minimal Path Method and Anisotropic Enhancement. *International Journal of Computer Vision*, 92(2):192–210.

Bhargav, S., Panda, B. P., Ali, M. e Javed, S. (2008). Solid-state fermentation systems-an overview. *Critical reviews in biotechnology*, 25(1-2):1–30.

Bjornsson, C. S., Lin, G., Al-Kofahi, Y., Narayanaswamy, A., Smith, K. L., Shain, W. e Roysam, B. (2008). Associative image analysis: A method for automated quantification of 3D multi-parameter images of brain tissue. *Journal of Neuroscience Methods*, 170(1):165–178.

Blondel, V. D., Guillaume, J.-L., Lambiotte, R. e Lefebvre, E. (2008). Fast unfolding of communities in large networks. *Journal of Statistical Mechanics: Theory and Experiment*, 2008(10):P10008.

Boland, M. V. e Murphy, R. F. (2001). A neural network classifier capable of recognizing the patterns of all major subcellular structures in fluorescence microscope images of HeLa cells. *Bioinformatics*, 17(12):1213–1223.

Bondy, A. e Murty, U. (2011). *Graph Theory*. Graduate Texts in Mathematics. Springer London.

Cai, J., Zeng, Z., Connor, J. N., Huang, C. Y., Melino, V., Kumar, P. e Miklavcic, S. J. (2015). RootGraph: a graphic optimization tool for automated image analysis of plant roots. *Journal of Experimental Botany*, 66(21):6551–6562.

Can, A., Shen, H., Turner, J. N., Tanenbaum, H. e Roysam, B. (1999). Rapid automated tracing and feature extraction from retinal fundus images using direct exploratory algorithms. *IEEE Transactions on Information Technology in Biomedicine*, 3(2):125–138.

Cannell, M. B., McMorland, A. e Soeller, C. (2006). Image Enhancement by Deconvolution. Em *Handbook Of Biological Confocal Microscopy*, páginas 488–500. Springer US, Boston, MA.

Cardona, A. e Tomancak, P. (2012). Current challenges in open-source bioimage informatics. *Nature Methods*, 9(7):661–665.

Carlile, M., Watkinson, S. e Gooday, G. (2001). *The Fungi*. Academic Press.

Casselton, L. e Zolan, M. (2002). The art and design of genetic screens: filamentous fungi. *Nature Reviews Genetics*, 3(9):683–697.

Chen, H., Xiao, H., Liu, T. e Peng, H. (2015). SmartTracing: self-learning-based Neuron reconstruction. *Brain Informatics*, 2(3):135–144.

Chenouard, N., Smal, I., de Chaumont, F., Maška, M., Sbalzarini, I. F., Gong, Y., Cardinale, J., Carthel, C., Coraluppi, S., Winter, M., Cohen, A. R., Godinez, W. J., Rohr, K., Kalaidzidis, Y., Liang, L., Duncan, J., Shen, H., Xu, Y., Magnusson, K. E. G., Jaldén, J., Blau, H. M., Paul-Gilloteaux, P., Roudot, P., Kervrann, C., Waharte, F., Tinevez, J.-Y., Shorte, S. L., Willemse, J., Celler, K., van Wezel, G. P., Dan, H.-W., Tsai, Y.-S., de Solórzano, C. O., Olivo-Marin, J.-C. e Meijering, E. (2014). Objective comparison of particle tracking methods. *Nature Methods*, 11(3):281–289.

Chothani, P., Mehta, V. e Stepanyants, A. (2011). Automated Tracing of Neurites from Light Microscopy Stacks of Images. *Neuroinformatics*, 9(2-3):263–278.

Claxton, N. S., Fellers, T. J. e Davidson, M. W. (2006). Confocal Microscopy. Em Webster, J. G., editor, *Encyclopedia of Medical Devices and Instrumentation*, páginas 1–37. John Wiley & Sons, 2 edition.

Cohen, L. D. e Kimmel, R. (1997). Global Minimum for Active Contour Models: A Minimal Path Approach. *International Journal of Computer Vision*, 24(1):57–78.

Coradin, J. H., Braun, A., Viccini, G., LUZ JR., L. F. d. L., Krieger, N. e Mitchell, D. A. (2011). A three-dimensional discrete lattice-based system for modeling the growth of aerial hyphae of filamentous fungi on solid surfaces: A tool for investigating micro-scale phenomena in solid-state fermentation. *Biochemical Engineering Journal*, 54(3):164–171.

Cox, P. W. e Thomas, C. R. (1992). Classification and measurement of fungal pellets by automated image analysis. *Biotechnology and Bioengineering*, 39(9):945–952.

Cuntz, H., Forstner, F., Borst, A. e Häusser, M. (2011). The TREES Toolbox—Probing the Basis of Axonal and Dendritic Branching. *Neuroinformatics*, 9(1):91–96.

Denk, W., Strickler, J. H. e Webb, W. W. (1990). Two-photon laser scanning fluorescence microscopy. *Science (New York, N.Y.)*, 248(4951):73–6.

Diestel, R. (2010). *Graph theory*. Springer, 4 edition.

Donohue, D. E. e Ascoli, G. A. (2011). Automated reconstruction of neuronal morphology: An overview. *Brain Research Reviews*, 67(1):94–102.

Evers, J. F., Schmitt, S., Sibila, M. e Duch, C. (2005). Progress in Functional Neuroanatomy: Precise Automatic Geometric Reconstruction of Neuronal Morphology From Confocal Image Stacks. *Journal of Neurophysiology*, 93(4).

Feng, L., Zhao, T. e Kim, J. (2015). neuTube 1.0: a New Design for Efficient Neuron Reconstruction Software Based on the SWC Format. *eNeuro*.

Flórez-Valencia, L., Pinzón, A. M., Richard, J.-C., Hoyos, M. H. e Orkisz, M. (2015). Simultaneous skeletonization and graph description of airway trees in 3D CT images. Em *XXVème Colloque GRETSI*, Lyon, France.

Forsyth, D. e Ponce, J. (2003). *Computer Vision: A Modern Approach*. An Alan R. Apt book. Prentice Hall.

Frangi, A. F., Niessen, W. J., Vincken, K. L. e Viergever, M. A. (1998). Multiscale vessel enhancement filtering. Em WELLS, W. M., COLCHESTER, A. e DELP, S., editores, *Medical Image Computing and Computer-Assisted Intervention — MICCAI'98. MICCAI 1998. Lecture Notes in Computer Science, vol 1496*, páginas 130–137. Springer Berlin Heidelberg.

Gala, R., Chapeton, J., Jitesh, J., Bhavsar, C. e Stepanyants, A. (2014). Active learning of neuron morphology for accurate automated tracing of neurites. *Frontiers in neuroanatomy*, 8:37.

Gillette, T. A., Brown, K. M. e Ascoli, G. A. (2011). The DIADEM metric: comparing multiple reconstructions of the same neuron. *Neuroinformatics*, 9(2-3):233–45.

Gonzalez, G., Fleurety, F. e Fua, P. (2009). Learning rotational features for filament detection. Em *2009 IEEE Conference on Computer Vision and Pattern Recognition*, páginas 1582–1589. IEEE.

Gonzalez, R. e Woods, R. (2011). *Digital Image Processing*. Pearson Education.

Grimm, L. H., Kelly, S., Krull, R. e Hempel, D. C. (2005). Morphology and productivity of filamentous fungi. *Applied Microbiology and Biotechnology*, 69(4):375–384.

Hamad, B. (2010). The antibiotics market. *Nature Reviews Drug Discovery*, 9(9):675–676.

Hamarneh, G. e Jassi, P. (2010). Vascusynth: Simulating vascular trees for generating volumetric image data with ground truth segmentation and tree analysis. *Computerized Medical Imaging and Graphics*, 34(8):605–616.

Hanzouli, H., Lapuyade-Lahorgue, J., Monfrini, E., Delso, G., Pieczynski, W., Visvikis, D. e Hatt, M. (2013). PET/CT image denoising and segmentation based on a multi observation and a multi scale Markov tree model. Em *2013 IEEE Nuclear Science Symposium and Medical Imaging Conference (2013 NSS/MIC)*, páginas 1–4. IEEE.

Heaton, L., Obara, B., Grau, V., Jones, N., Nakagaki, T., Boddy, L. e Fricker, M. D. (2012). Analysis of fungal networks. *Fungal Biology Reviews*, 26(1):12–29.

Hille, A., Neu, T. R., Hempel, D. C. e Horn, H. (2005). Oxygen profiles and biomass distribution in biopellets of *Aspergillus niger*. *Biotechnology and Bioengineering*, 92(5):614–623.

Ho, S.-Y., Chao, C.-Y., Huang, H.-L., Chiu, T.-W., Charoenkwan, P. e Hwang, E. (2011). NeurphologyJ: An automatic neuronal morphology quantification method and its application in pharmacological discovery. *BMC Bioinformatics*, 12(1):230.

INSPQ, Institut national de santé publique du Québec, G. d. Q. (2010). *Aspergillus niger*. `https://www.inspq.qc.ca/es/node/484`. Accessed: November 8th 2017.

Ison, J., Kalaš, M., Jonassen, I., Bolser, D., Uludag, M., McWilliam, H., Malone, J., Lopez, R., Pettifer, S. e Rice, P. (2013). EDAM: An ontology of bioinformatics operations, types of data and identifiers, topics, and formats. *Bioinformatics*, 29(10):1325–1332.

Ito, K., Kimizuka, A., Okazaki, N. e Kobayashi, S. (1989). Mycelial distribution in rice *koji*. *Journal of Fermentation and Bioengineering*, 68(1):7–13.

Jähne, B. (1997). *Digital Image Processing: Concepts, Algorithms, and Scientific Applications*. Número v. 1 em Digital Image Processing: Concepts, Algorithms, and Scientific Applications. Berlin.

Jähne, B., Haussecker, H. e Geissler, P. (1999). *Handbook of Computer Vision and Applications: Signal processing and pattern recognition*. Número v. 2 em Handbook of Computer Vision and Applications. Academic Press.

Jonathan, S. e Fasidi, I. (2001). Effect of carbon, nitrogen and mineral sources on growth of Psathyerella atroumbonata (Pegler), a Nigerian edible mushroom. *Food Chemistry*, 72(4):479–483.

Junker, B. e Schreiber, F. (2011). *Analysis of Biological Networks*. Wiley Series in Bioinformatics. Wiley.

Kalaš, M. e from NEUBIAS Taggathons, C. (2016-2018a). edamontology/edam-bioimaging. `https://github.com/edamontology/edam-bioimaging`. Software (all versions).

Kalaš, M. e from NEUBIAS Taggathons, C. (2018b). edamontology/edam-bioimaging: alpha03. `https://github.com/edamontology/edam-bioimaging/releases/tag/alpha03`. Software version.

Kalaš, M., Plantard, L., Kirschmann, M. A., Lindblad, J., Chessel, A., Sladoje-Matić, N., Scholz, L. A., Zhang, C., Rössler, F., Dufour, A., Bogovic, J. A., Jones, M., Moore, J., Gaignard, A., Paavolainen, L., Hörl, D., Golani, O., Participants in the NEUBIAS Taggathons, Paul-Gilloteaux, P., the EDAM dev team, Miura, K., Colombelli, J. e welcoming contributors (2018). EDAM-bioimaging: the ontology of bioimage informatics operations, topics, data, and formats [version 1; not peer reviewed]. *F1000Research*, 7(ELIXIR):180. Poster.

Kass, M., Witkin, A. e Terzopoulos, D. (1988). Snakes: Active contour models. *International Journal of Computer Vision*, 1(4):321–331.

Kirbas, C. e Quek, F. K. H. (2003). Vessel extraction techniques and algorithms : A survey. *Proceedings - 3rd IEEE Symposium on BioInformatics and BioEngineering, BIBE 2003*, 36(2):238–245.

Kirshner, H., Aguer, F., Sage, D. e Unser, M. (2013). 3-D PSF fitting for fluorescence microscopy: implementation and localization application. *Journal of Microscopy*, 249(1):13–25.

Koh, I. Y. Y., Lindquist, W. B., Zito, K., Nimchinsky, E. A. e Svoboda, K. (2002). An Image Analysis Algorithm for Dendritic Spines. *Neural Computation*, 14(6):1283–1310.

Krauss, P., Metzner, C., Lange, J., Lang, N. e Fabry, B. (2012). Parameter-Free Binarization and Skeletonization of Fiber Networks from Confocal Image Stacks. *PLoS ONE*, 7(5):1–8.

Krissian, K., Malandain, G. e Ayache, N. (1997). Directional anisotropic diffusion applied to segmentation of vessels in 3D images. Em HAAR ROMENY, B., FLORACK, L., KOENDERINK, K. e VIERGEVER, M., editores, *Scale-Space Theory in Computer Vision. Scale-Space 1997. Lecture Notes in Computer Science, vol 1252*, páginas 345–348. Springer, Berlin, Heidelberg.

Krissian, K., Malandain, G., Ayache, N., Vaillant, R. e Trousset, Y. (2000). Model-Based Detection of Tubular Structures in 3D Images. *Computer Vision and Image Understanding*, 80(2):130–171.

Krull, R., Wucherpfennig, T., Esfandabadi, M. E., Walisko, R., Melzer, G., Hempel, D. C., Kampen, I., Kwade, A. e Wittmann, C. (2013). Characterization and control of fungal morphology for improved production performance in biotechnology. *Journal of Biotechnology*, 163(2):112–123.

Kües, U. e Fischer, R. (2006). *Growth, Differentiation and Sexuality*. The Mycota. Springer Berlin Heidelberg.

Law, M. W. K. e Chung, A. C. S. (2008). Three Dimensional Curvilinear Structure Detection Using Optimally Oriented Flux. Em FORSYTH, D., TORR, P. e ZISSERMAN, A., editores, *Computer Vision – ECCV 2008. ECCV 2008. Lecture Notes in Computer Science, vol 5305*, páginas 368–382, Berlin, Heidelberg. Springer Berlin Heidelberg.

Lee, P. C., Ching, Y., Chang, H. M. e Chiang, A. (2008). A semi-automatic method for neuron centerline extraction in confocal microscopic image stack. Em *2008 5th IEEE International Symposium on Biomedical Imaging: From Nano to Macro*, páginas 959–962. IEEE.

Lee, P.-C., Chuang, C.-C., Chiang, A.-S., Ching, Y.-T., Hsieh, C., Noda, H., Fukami, K., Sakaue-Sawano, A. e Miyawaki, A. (2012). High-throughput Computer Method for 3D Neuronal Structure Reconstruction from the Image Stack of the Drosophila Brain and Its Applications. *PLoS Computational Biology*, 8(9):e1002658.

Lesage, D., Angelini, E. D., Bloch, I. e Funka-Lea, G. (2009). A review of 3D vessel lumen segmentation techniques: Models, features and extraction schemes. *Medical Image Analysis*, 13(6):819–845.

Liu, S., Zhang, D., Liu, S., Feng, D., Peng, H. e Cai, W. (2016). Rivulet: 3D Neuron Morphology Tracing with Iterative Back-Tracking. *Neuroinformatics*, 14(4):387–401.

Lobet, G., Draye, X. e Périlleux, C. (2013). An online database for plant image analysis software tools. *Plant Methods*, 9(1):38.

Lobet, G., Pages, L. e Draye, X. (2011). A Novel Image-Analysis Toolbox Enabling Quantitative Analysis of Root System Architecture. *Plant Physiology*, 157(1):29–39.

Longair, M. H., Baker, D. A. e Armstrong, J. D. (2011). Simple neurite tracer: Open source software for reconstruction, visualization and analysis of neuronal processes. *Bioinformatics*, 27(17):2453–2454.

Lopez-Molina, C., Vidal-Diez de Ulzurrun, G., Baetens, J., Van den Bulcke, J. e De Baets, B. (2015). Unsupervised ridge detection using second order anisotropic Gaussian kernels. *Signal Processing*, 116:55–67.

Losavio, B. E., Liang, Y., Santamaria-Pang, A., Kakadiaris, I. A., Colbert, C. M. e Saggau, P. (2008). Live Neuron Morphology Automatically Reconstructed From Multiphoton and Confocal Imaging Data. *Journal of Neurophysiology*, 100(4):2422–2429.

Lu, J., Fiala, J. C. e Lichtman, J. W. (2009). Semi-Automated Reconstruction of Neural Processes from Large Numbers of Fluorescence Images. *PLoS ONE*, 4(5):e5655.

Mairhofer, S., Zappala, S., Tracy, S., Sturrock, C., Bennett, M. J., Mooney, S. J. e Pridmore, T. P. (2013). Recovering complete plant root system architectures from soil via X-ray μ-Computed Tomography. *Plant Methods*, 9(1):8.

Maizel, A., Von Wangenheim, D., Federici, F., Haseloff, J. e Stelzer, E. H. K. (2011). High-resolution live imaging of plant growth in near physiological bright conditions using light sheet fluorescence microscopy. *Plant Journal*, 68(2):377–385.

Maška, M., Ulman, V., Svoboda, D., Matula, P., Matula, P., Ederra, C., Urbiola, A., España, T., Venkatesan, S., Balak, D. M., Karas, P., Bolcková, T., Štreitová, M., Carthel, C., Coraluppi, S., Harder, N., Rohr, K., Magnusson, K. E. G., Jaldén, J., Blau, H. M., Dzyubachyk, O., Křížek, P., Hagen, G. M., Pastor-Escuredo, D., Jimenez-Carretero, D., Ledesma-Carbayo, M. J., Muñoz-Barrutia, A., Meijering, E., Kozubek, M. e Ortiz-de Solorzano, C. (2014). A benchmark for comparison of cell tracking algorithms. *Bioinformatics*, 30(11):1609–1617.

Mayerich, D., Bjornsson, C., Taylor, J. e Roysam, B. (2012). NetMets: software for quantifying and visualizing errors in biological network segmentation. *BMC Bioinformatics 2012 13:8*, 13(8):1–19.

Mayerich, D. e Keyser, J. (2009). Hardware Accelerated Segmentation of Complex Volumetric Filament Networks. *IEEE Transactions on Visualization and Computer Graphics*, 15(4):670–681.

Meijering, E. (2010). Neuron tracing in perspective. *Cytometry Part A*, 77A(7):693–704.

Meijering, E., Jacob, M., Sarria, J.-C., Steiner, P., Hirling, H. e Unser, M. (2004). Design and validation of a tool for neurite tracing and analysis in fluorescence microscopy images. *Cytometry*, 58A(2):167–176.

Metz, B., de Bruijn, E. W. e VAN SUIJDAM, J. C. (1981). Methods for quantitative representation of the morphology of molds. *Biotechnology and Bioengineering*, 23(1):149–162.

Mitchel, J. A., Martin, I. S. e Hoffman-Kim, D. (2013). Neurient: an algorithm for automatic tracing of confluent neuronal images to determine alignment. *Journal of neuroscience methods*, 214(2):210–22.

Miura, K. (2013). *Basics of Image Processing and Analysis*.

Miura, K., editor (2016). *Bioimage Data Analysis*. Wiley-VCH Verlag.

Moore-Landecker, E. (2001). *Fungal Spores*. John Wiley and Sons, Ltd.

Mottini, A., Descombes, X. e Besse, F. (2012). Axon extraction from fluorescent confocal microscopy images. Em *2012 9th IEEE International Symposium on Biomedical Imaging (ISBI)*, páginas 764–767. IEEE.

Murtey, M. D. e Ramasamy, P. (2016). Sample Preparations for Scanning Electron Microscopy – Life Sciences. Em *Modern Electron Microscopy in Physical and Life Sciences*. InTech.

Myatt, D. R., Hadlington, T., Ascoli, G. A. e Nasuto, S. J. (2012). Neuromantic – from Semi-Manual to Semi-Automatic Reconstruction of Neuron Morphology. *Frontiers in Neuroinformatics*, 6:4.

Narayanaswamy, A., Wang, Y. e Roysam, B. (2011). 3-D Image Pre-processing Algorithms for Improved Automated Tracing of Neuronal Arbors. *Neuroinformatics*, 9(2-3):219–231.

Narro, M. L., Yang, F., Kraft, R., Wenk, C., Efrat, A. e Restifo, L. L. (2007). NeuronMetrics: Software for semi-automated processing of cultured neuron images. *Brain Research*, 1138:57–75.

Nopharatana, M. (1999). *Microscale studies of fungal growth in solid state fermentation / by Montira Nopharatana.* Tese de doutorado, University of Queensland, St.Lucia, Qld.

Nopharatana, M., Mitchell, D. A. e Howes, T. (2003). Use of confocal scanning laser microscopy to measure the concentrations of aerial and penetrative hyphae during growth of *Rhizopus oligosporus* on a solid surface. *Biotechnology and Bioengineering*, 84(1):71–77.

Novy, V., Schmid, M., Eibinger, M., Petrasek, Z. e Nidetzky, B. (2016). The micromorphology of *Trichoderma reesei* analyzed in cultivations on lactose and solid lignocellulosic substrate, and its relationship with cellulase production. *Biotechnology for Biofuels*, 9(1):169.

Obara, B., Fricker, M. e Grau, V. (2012a). Contrast independent detection of branching points in network-like structures. Em Haynor, D. R. e Ourselin, S., editores, *Medical Imaging 2012: Image Processing. Procedings of SPIE Vol. 8314*, página 83141L. International Society for Optics and Photonics.

Obara, B., Grau, V. e Fricker, M. D. (2012b). A bioimage informatics approach to automatically extract complex fungal networks. *Bioinformatics (Oxford, England)*, 28(18):2374–81.

Packer, H. L., Keshavarz-Moore, E., Lilly, M. D. e Thomas, C. R. (1992). Estimation of cell volume and biomass of penicillium chrysogenum using image analysis. *Biotechnology and Bioengineering*, 39(4):384–391.

Packer, H. L. e Thomas, C. R. (1990). Morphological measurements on filamentous microorganisms by fully automatic image analysis. *Biotechnology and Bioengineering*, 35(9):870–881.

Paddock, S. W., Fellers, T. J. e Davidson, M. W. (2018). Introductory confocal concepts. `https://www.microscopyu.com/techniques/confocal/introductory-confocal-concepts`. Accessed: July 20th 2018.

Papagianni, M. (2004). Fungal morphology and metabolite production in submerged mycelial processes. *Biotechnology Advances*, 22(3):189–259.

Paul, G. C., Kent, C. A. e Thomas, C. R. (1994). Hyphal vocuolation and fragmentation in *Penicillium chrysogenum*. *Biotechnology and Bioengineering*, 44(5):655–660.

Pel, H. J., de Winde, J. H., Archer, D. B., Dyer, P. S., Hofmann, G., Schaap, P. J., Turner, G., de Vries, R. P., Albang, R., Albermann, K., Andersen, M. R., Bendtsen, J. D., Benen, J. A. E., van den Berg, M., Breestraat, S., Caddick, M. X., Contreras, R., Cornell, M., Coutinho, P. M., Danchin, E. G. J., Debets, A. J. M., Dekker, P., van Dijck, P. W. M., van Dijk, A., Dijkhuizen, L., Driessen, A. J. M., D'Enfert, C., Geysens, S., Goosen, C., Groot, G. S. P., de Groot, P. W. J., Guillemette, T., Henrissat, B., Herweijer, M., van den Hombergh, J. P. T. W., van den Hondel, C. A. M. J. J., van der Heijden, R. T. J. M., van der Kaaij, R. M., Klis, F. M., Kools, H. J., Kubicek, C. P., van Kuyk, P. A., Lauber, J., Lu, X., van der Maarel, M. J. E. C., Meulenberg, R., Menke, H., Mortimer, M. A., Nielsen, J., Oliver, S. G., Olsthoorn, M., Pal, K., van Peij, N. N. M. E., Ram, A. F. J., Rinas, U., Roubos, J. A., Sagt, C. M. J., Schmoll, M., Sun, J., Ussery, D., Varga, J., Vervecken, W., van de Vondervoort, P. J. J., Wedler, H., Wösten, H. A. B., Zeng, A.-P., van Ooyen, A. J. J., Visser, J. e Stam, H. (2007). Genome sequencing and analysis of the versatile cell factory Aspergillus niger CBS 513.88. *Nature Biotechnology*, 25(2):221–231.

Peng, H., Long, F. e Myers, G. (2011). Automatic 3D neuron tracing using all-path pruning. *Bioinformatics*, 27(13):i239–i247.

Peng, H., Ruan, Z., Atasoy, D. e Sternson, S. (2010a). Automatic reconstruction of 3D neuron structures using a graph-augmented deformable model. *Bioinformatics*, 26(12):i38–i46.

Peng, H., Ruan, Z., Long, F., Simpson, J. H. e Myers, E. W. (2010b). V3D enables real-time 3D visualization and quantitative analysis of large-scale biological image data sets. *Nature Biotechnology*, 28(4):348–353.

Pitol, L. O., Finkler, A. T. J., Dias, G. S., Machado, A. S., Zanin, G. M., Mitchell, D. A. e Krieger, N. (2017). Optimization studies to develop a low-cost medium for production of the lipases of Rhizopus microsporus by solid-state fermentation and scale-up of the process to a pilot packed-bed bioreactor. *Process Biochemistry*, 62:37–47.

Pool, M., Thiemann, J., Bar-Or, A. e Fournier, A. E. (2008). NeuriteTracer: A novel ImageJ plugin for automated quantification of neurite outgrowth. *Journal of Neuroscience Methods*, 168(1):134–139.

Quan, T., Zhou, H., Li, J., Li, S., Li, A., Li, Y., Lv, X., Luo, Q., Gong, H. e Zeng, S. (2015). NeuroGPS-Tree: automatic reconstruction of large-scale neuronal populations with dense neurites. *Nature Methods*, 13(1):51–54.

Rahardjo, Y. S., Tramper, J. e Rinzema, A. (2006). Modeling conversion and transport phenomena in solid-state fermentation: A review and perspectives. *Biotechnology Advances*, 24(2):161–179.

Rahardjo, Y. S. P. (2005). *Fungal mats in solid-state fermentation*. Tese de doutorado, Wageningen University.

Reichl, U., Buschulte, T. K. e Gilles, E. D. (1990). Study of the early growth and branching of *Streptomyces tendae* by means of an image processing system. *Journal of Microscopy*, 158(1):55–62.

Rellán-Álvarez, R., Lobet, G., Lindner, H., Pradier, P.-L., Sebastian, J., Yee, M.-C., Geng, Y., Trontin, C., LaRue, T., Schrager-Lavelle, A., Haney, C. H., Nieu, R., Maloof, J., Vogel, J. P. e Dinneny, J. R. (2015). GLO-Roots: an imaging platform enabling multidimensional characterization of soil-grown root systems. *eLife*, 4.

Reynaud, E. G., Krzic, U., Greger, K. e Stelzer, E. H. K. (2008). Light sheet-based fluorescence microscopy: more dimensions, more photons, and less photodamage. *HFSP journal*, 2(5):266–75.

Rigort, A., Günther, D., Hegerl, R., Baum, D., Weber, B., Prohaska, S., Medalia, O., Baumeister, W. e Hege, H.-C. (2012). Automated segmentation of electron tomograms for a quantitative description of actin filament networks. *Journal of Structural Biology*, 177(1):135–144.

Riquelme, M., Reynaga-Peña, C. G., Gierz, G. e Bartnicki-Garcia, S. (1998). What Determines Growth Direction in Fungal Hyphae? *Fungal Genetics and Biology*, 24(1-2):101–109.

Rodriguez, A., Ehlenberger, D. B., Dickstein, D. L., Hof, P. R. e Wearne, S. L. (2008). Automated Three-Dimensional Detection and Shape Classification of Dendritic Spines from Fluorescence Microscopy Images. *PLoS ONE*, 3(4):1–12.

Rodriguez, A., Ehlenberger, D. B., Hof, P. R. e Wearne, S. L. (2009). Three-dimensional neuron tracing by voxel scooping. *Journal of Neuroscience Methods*, 184(1):169–175.

Sage, D., Donati, L., Soulez, F., Fortun, D., Schmit, G., Seitz, A., Guiet, R., Vonesch, C. e Unser, M. (2017). DeconvolutionLab2: An open-source software for deconvolution microscopy. *Methods*, 115:28–41.

Samson, R., Noonim, P., Meijer, M., Houbraken, J., Frisvad, J. e Varga, J. (2007). Diagnostic tools to identify black aspergilli. *Studies in Mycology*, 59:129–145.

Santamaría-Pang, A., Hernandez-Herrera, P., Papadakis, M., Saggau, P. e Kakadiaris, I. A. (2015). Automatic Morphological Reconstruction of Neurons from Multiphoton and Confocal Microscopy Images Using 3D Tubular Models. *Neuroinformatics*, 13(3):297–320.

Sati, S. e Bisht, S. (2006). Utilization of various carbon sources for the growth of waterborne conidial fungi. *Mycologia*, 98(5):678–681.

Sato, Y., Nakajima, S., Shiraga, N., Atsumi, H., Yoshida, S., Koller, T., Gerig, G. e Kikinis, R. (1998). Three-dimensional multi-scale line filter for segmentation and visualization of curvilinear structures in medical images. *Medical Image Analysis*, 2(2):143–168.

Sazak, C., Nelson, C. J. e Obara, B. (2018). The Multiscale Bowler-Hat Transform for Vessel Enhancement in 3D Biomedical Images.

Schindelin, J., Arganda-Carreras, I., Frise, E., Kaynig, V., Longair, M., Pietzsch, T., Preibisch, S., Rueden, C., Saalfeld, S., Schmid, B., Tinevez, J.-Y., White, D. J., Hartenstein, V., Eliceiri, K., Tomancak, P. e Cardona, A. (2012). Fiji: an open-source platform for biological-image analysis. *Nature Methods*, 9(7):676–682.

Schmitt, S., Evers, J. F., Duch, C., Scholz, M. e Obermayer, K. (2004). New methods for the computer-assisted 3-D reconstruction of neurons from confocal image stacks. *NeuroImage*, 23(4):1283–1298.

Schneider, C. A., Rasband, W. S. e Eliceiri, K. W. (2012). NIH Image to ImageJ: 25 years of image analysis. *Nature Methods*, 9(7):671–675.

Schutyser, M. A. I. (2003). *Mixed solid-state fermentation : numerical modeling and experimental validation*. Tese de doutorado, Wageningen University.

Serra, J. (1984). *Image Analysis and Mathematical Morphology*. Número v. 1 em Image Analysis and Mathematical Morphology. Academic Press.

Sethian, J. A. (1998). Fast marching methods and level set methods for propagating interfaces.

Shapiro, L. e Stockman, G. (2001a). *Computer Vision*. Prentice Hall.

Shapiro, L. G. e Stockman, G. C. (2001b). *Computer vision*. Prentice Hall.

Sheppard, C. J. R., Gan, X., Gu, M. e Roy, M. (2006). Signal-to-Noise Ratio in Confocal Microscopes. Em *Handbook Of Biological Confocal Microscopy*, páginas 442–452. Springer US, Boston, MA.

Sheppard, C. J. R., Gu, M. e Roy, M. (1992). Signal-to-noise ratio in confocal microscope systems. *Journal of Microscopy*, 168(3):209–218.

Singh, R., Kumar, M., Mittal, A. e Mehta, P. K. (2016). Microbial enzymes: industrial progress in 21st century. *3 Biotech*, 6(2):174.

Sironi, A., Turetken, E., Lepetit, V. e Fua, P. (2016). Multiscale Centerline Detection. *IEEE Transactions on Pattern Analysis and Machine Intelligence*, 38(7):1327–1341.

Smith, M. B., Li, H., Shen, T., Huang, X., Yusuf, E. e Vavylonis, D. (2010). Segmentation and tracking of cytoskeletal filaments using open active contours. *Cytoskeleton*, 67(11):693–705.

Srinivasan, R., Zhou, X., Miller, E., Lu, J., Litchman, J. e Wong, S. T. C. (2007). Automated Axon Tracking of 3D Confocal Laser Scanning Microscopy Images Using Guided Probabilistic Region Merging. *Neuroinformatics*, 5(3):189–203.

Sternberg, S. (1983). Biomedical Image Processing. *Computer*, 16(1):22–34.

Sugai-Guérios, M. H. (2016). *Understanding the growth of hyphae of filamentous fungi on the surfaces of solid media through computational models and confocal microscopy*. Tese de doutorado, Federal University of Santa Catarina.

Sugai-Guérios, M. H., Balmant, W., Furigo, A., Krieger, N., Mitchell, D. A. e Balmant, W. (2015). Modeling the growth of filamentous fungi at the particle scale in solid - State fermentation systems. *Advances in Biochemical Engineering/Biotechnology*, 149:171–221.

Sugai-Guérios, M. H., Balmant, W., Krieger, N., Furigo Junior, A. e Mitchell, D. A. (2016). Colonization of solid particles by *Rhizopus oligosporus* and Aspergillus oryzae in solid-state fermentation involves two types of penetrative hyphae: A model-based study on how these hyphae grow. *Biochemical Engineering Journal*, 114:173–182.

Te Biesebeke, R., Record, E., van Biezen, N., Heerikhuisen, M., Franken, A., Punt, P. J. e van den Hondel, C. A. M. J. J. (2005). Branching mutants of Aspergillus oryzae with improved amylase and protease production on solid substrates. *Applied Microbiology and Biotechnology*, 69(1):44–50.

The MathWorks Inc. (2015). Matlab version 8.5.0.197613 (r2015a).

Thomas, C. R. (1992). Image analysis: putting filamentous microorganisms in the picture. *Trends in Biotechnology*, 10:343–348.

Trinci, A. P. J. (1971). Influence of the Width of the Peripheral Growth Zone on the Radial Growth Rate of Fungal Colonies on Solid Media. *Journal of General Microbiology*, 67(3):325–344.

Trinci, A. P. J. (1974). A Study of the Kinetics of Hyphal Extension and Branch Initiation of Fungal Mycelia. *Journal of General Microbiology*, 81(1):225–236.

Tsai, C.-L., Stewart, C., Tanenbaum, H. e Roysam, B. (2004). Model-Based Method for Improving the Accuracy and Repeatability of Estimating Vascular Bifurcations and Crossovers From Retinal Fundus Images. *IEEE Transactions on Information Technology in Biomedicine*, 8(2):122–130.

Tucker, K. G., Kelly, T., Delgrazia, P. e Thomas, C. R. (1992). Fully-automatic measurement of mycelial morphology by image analysis. *Biotechnology Progress*, 8(4):353–359.

Türetken, E., Benmansour, F. e Fua, P. (2012). Automated reconstruction of tree structures using path classifiers and Mixed Integer Programming. Em *2012 IEEE Conference on Computer Vision and Pattern Recognition*, páginas 566–573. IEEE.

Türetken, E., González, G., Blum, C. e Fua, P. (2011). Automated Reconstruction of Dendritic and Axonal Trees by Global Optimization with Geometric Priors. *Neuroinformatics*, 9(2-3):279–302.

Tyrrell, J. A., di Tomaso, E., Fuja, D., Tong, R., Kozak, K., Jain, R. K. e Roysam, B. (2007). Robust 3-D Modeling of Vasculature Imagery Using Superellipsoids. *IEEE Transactions on Medical Imaging*, 26(2):223–237.

Tyrrell, J. A., Mahadevan, V., Tong, R. T., Brown, E. B., Jain, R. K. e Roysam, B. (2005). A 2-D/3-D model-based method to quantify the complexity of microvasculature imaged by in vivo multiphoton microscopy. *Microvascular Research*, 70(3):165–178.

Uylings, H. B. e Van Pelt, J. (2002). Measures for quantifying dendritic arborizations. *Network: Computation in Neural Systems*, 13(3):397–414.

Vallotton, P., Lagerstrom, R., Sun, C., Buckley, M., Wang, D., De Silva, M., Tan, S.-S. e Gunnersen, J. M. (2007). Automated analysis of neurite branching in cultured cortical neurons using HCA-Vision. *Cytometry Part A*, 71A(10):889–895.

Van Suijdam, J. C. e Metz, B. (1981). Influence of Engineering Variables upon the Morphology of Filamentous Molds. *Biotechnology and Bioengineering*, 23:111–148.

Vanhoutte, B., Pons, M. N., Thomas, C. R., Louvel, L. e Vivier, H. (1995). Characterization of *Penicillium chrysogenum* physiology in submerged cultures by color and monochrome image analysis. *Biotechnology and Bioengineering*, 48(1):1–11.

Vasilkoski, Z. e Stepanyants, A. (2009). Detection of the optimal neuron traces in confocal microscopy images. *Journal of Neuroscience Methods*, 178(1):197–204.

von Wangenheim, D., Hauschild, R. e Friml, J. (2017). Light Sheet Fluorescence Microscopy of Plant Roots Growing on the Surface of a Gel. *Journal of Visualized Experiments*, (119).

Wang, J., Zhou, X., Lu, J., Lichtman, J., Chang, S.-f. e Wong, S. (2007). Dynamic local tracing for 3D axon curvilinear structure detection from microscopic image stack. Em *2007 4th IEEE International Symposium on Biomedical Imaging: From Nano to Macro*, páginas 81–84. IEEE.

Wang, Y., Narayanaswamy, A., Tsai, C.-L. e Roysam, B. (2011). A Broadly Applicable 3-D Neuron Tracing Method Based on Open-Curve Snake. *Neuroinformatics*, 9(2-3):193–217.

Wang, Z. e Bovik, A. (2009). Mean squared error: Love it or leave it? A new look at Signal Fidelity Measures. *IEEE Signal Processing Magazine*, 26(1):98–117.

Wang, Z., Bovik, A., Sheikh, H. e Simoncelli, E. (2004). Image Quality Assessment: From Error Visibility to Structural Similarity. *IEEE Transactions on Image Processing*, 13(4):600–612.

Wearne, S., Rodriguez, A., Ehlenberger, D., Rocher, A., Henderson, S. e Hof, P. (2005). New techniques for imaging, digitization and analysis of three-dimensional neural morphology on multiple scales. *Neuroscience*, 136(3):661–680.

Weaver, C. M., Hof, P. R., Wearne, S. L. e Lindquist, W. B. (2004). Automated Algorithms for Multiscale Morphometry of Neuronal Dendrites. *Neural Computation*, 16(7):1353–1383.

Wilkinson, M. D., Dumontier, M., Aalbersberg, I. J., Appleton, G., Axton, M., Baak, A., Blomberg, N., Boiten, J.-W., da Silva Santos, L. B., Bourne, P. E., Bouwman, J., Brookes, A. J., Clark, T., Crosas, M., Dillo, I., Dumon, O., Edmunds, S., Evelo, C. T., Finkers, R., Gonzalez-Beltran, A., Gray, A. J., Groth, P., Goble, C., Grethe, J. S., Heringa, J., 't Hoen, P. A., Hooft, R., Kuhn, T., Kok, R., Kok, J., Lusher, S. J., Martone, M. E., Mons, A., Packer, A. L., Persson, B., Rocca-Serra, P., Roos, M., van Schaik, R., Sansone, S.-A., Schultes, E., Sengstag, T., Slater, T., Strawn, G., Swertz, M. A., Thompson, M., van der Lei, J., van Mulligen, E., Velterop, J., Waagmeester, A., Wittenburg, P., Wolstencroft, K., Zhao, J. e Mons, B. (2016). The FAIR Guiding Principles for scientific data management and stewardship. *Scientific Data*, 3:160018.

Wilkinson, M. H. F. e Westenberg, M. A. (2001). Shape Preserving Filament Enhancement Filtering. Em Niessen, W. e Viergever, M., editores, *Medical Image Computing and Computer-Assisted Intervention – MICCAI 2001. MICCAI 2001. Lecture Notes in Computer Science, vol 2208.*, páginas 770–777. Springer Berlin Heidelberg.

Wu, J., He, Y., Yang, Z., Guo, C., Luo, Q., Zhou, W., Chen, S., Li, A., Xiong, B., Jiang, T. e Gong, H. (2014). 3D BrainCV: Simultaneous visualization and analysis of cells and capillaries in a whole mouse brain with one-micron voxel resolution. *NeuroImage*, 87:199–208.

Xiao, H. e Peng, H. (2013). APP2: automatic tracing of 3D neuron morphology based on hierarchical pruning of a gray-weighted image distance-tree. *Bioinformatics*, 29(11):1448–1454.

Xiong, G., Zhou, X., Degterev, A., Ji, L. e Wong, S. T. C. (2006). Automated neurite labeling and analysis in fluorescence microscopy images. *Cytometry Part A*, 69A(6):494–505.

Xu, C., Pham, D. L. e Prince, J. L. (2000). *Handbook of Medical Imaging, Volume 2. Medical Image Processing and Analysis*, volume 2, capítulo: Image segmentation using deformable models, páginas 129–174. Bellingham, WA: SPIE Press.

Xu, T., Vavylonis, D., Tsai, F. C., Koenderink, G. H., Nie, W., Yusuf, E., Lee, I. J., Wu, J. Q. e Huang, X. (2015). SOAX: A software for quantification of 3D biopolymer networks. *Scientific Reports*, 5:9081.

Yamasaki, T., Isokawa, T., Matsui, N., Ikeno, H. e Kanzaki, R. (2006). Reconstruction and simulation for three-dimensional morphological structure of insect neurons. *Neurocomputing*, 69(10-12):1043–1047.

Yang, H., Reichl, U., King, R. e Gilles, E. D. (1992). Measurement and simulation of the morphological development of filamentous microorganisms. *Biotechnology and Bioengineering*, 39(1):44–48.

Yang, J., Gonzalez-Bellido, P. T. e Peng, H. (2013). A distance-field based automatic neuron tracing method. *BMC Bioinformatics*, 14(1):93.

Yoo, T. S. (2004). *Insight into Images*. A K Peters/CRC Press.

Zhang, Y., Zhou, X., Degterev, A., Lipinski, M., Adjeroh, D., Yuan, J. e Wong, S. T. (2007). A novel tracing algorithm for high throughput imaging. *Journal of Neuroscience Methods*, 160(1):149–162.

Zhang, Y., Zhou, X., Lu, J., Lichtman, J., Adjeroh, D. e Wong, S. T. C. (2008). 3D Axon Structure Extraction and Analysis in Confocal Fluorescence Microscopy Images. *Neural Computation*, 20(8):1899–1927.

Zhao, T., Xie, J., Amat, F., Clack, N., Ahammad, P., Peng, H., Long, F. e Myers, E. (2011). Automated Reconstruction of Neuronal Morphology Based on Local Geometrical and Global Structural Models. *Neuroinformatics*, 9(2-3):247–261.

Zhou, Z., Liu, X., Long, B. e Peng, H. (2016). TReMAP: Automatic 3D Neuron Reconstruction Based on Tracing, Reverse Mapping and Assembling of 2D Projections. *Neuroinformatics*, 14(1):41–50.

Appendix A: Lists of image analysis and filament tracing softwares, plug-ins and libraries

Table A.1: List of software for image analysis and biofilament tracing - Part 1

Software name	Openness*	Organization / Maintained by	Main language	Library / Toolkit?	Allows customization? **
Matlab - Image Processing toolbox	P, C	Mathworks®	Matlab	Yes	Yes
ImageJ Fiji	O, F	ImageJ2, Fiji Distribution	Java	No	Yes
Vaa3D	O, F	HHMI - Janelia Research Campus, Allen Institute for Brain Science	C/C++	No	Yes
SOAX	O, F	Lehigh University	C++	No	No
NeuronStudio	F	CNIC at Icahn School of Medicine at Mount Sinai	C/C++	No	No
Neural Circuit Tracer	O	Northeastern University	Java, Matlab	No	No
Neuromantic	O,F	University of Reading	C++	No	No
NeuTube	O,F	HHMI - Janelia Research Campus and Korea Institute of Science and Technology (KIST)	C/C++	No	No
ORION	O, F	University of Houston	C/C++	No	No
FARSight	O, F	University of Houston	C/C++	Yes	NA
Reconstruct	F	University of Texas at Austin	-	No	No
Tree2Tree	O, F	University of Virginia	Matlab	No	No

* P - proprietary, C- commercially available, O - Open-source, F - Free

** Plug-ins, add-ins, scripts

Table A.1 continuation: List of software for image analysis and biofilament tracing - Part 1

Software name	Openness*	Organization / Maintained by	Main language	Library / Toolkit?	Allows customization? **
RooTrak	O, F	University of Nottingham	C++	No	No
IMOD	O, F	University of Colorado	C/C++	No	No
OpenCV	O, F	Intel Inc.	C++	Yes	NA
VIAS	O, F	CNIC at Icahn School of Medicine at Mount Sinai	C/C++	No	No
ITK	O, F	Kitware Inc.	C/C++	Yes	No
ImgLib	O, F	-	Java	Yes	NA
ImgLib2	O, F	MPI-CBG, EMBL, LOCI	Java	Yes	NA
VTK	O, F	Kitware Inc.	C/C++	Yes	NA
ilastik	O, F	HCI Unversity of Heidelberg, HHMI Janelia Farm Research Campus, CellNetworks	Python	No	Yes
Scikit-image	O, F	SciPy.org	Python	Yes	NA
3DMA Neuron (ExFact® Analysis for Fiber)	P, C	Nihon Visual Science, Inc.	Unkown	No	No
HCA-Vision	P, C	CSIRO	Unkown	No	No
Amira	P, C	FEI	Unkown	No	Yes
Imaris	P, C	Bitplane	Unkown	No	Yes
Neurolucida	P, C	MBF Bioscience	Unkown	No	No

* P - proprietary, C- commercially available, O - Open-source, F - Free

** Plug-ins, add-ins, scripts

Table A.2: List of software for image analysis and biofilament tracing - Part 2

Software name	Initially intended for	Publication number (Table 4.3) that uses or has implementation in it	Status*** / Last release	Supported OS
Matlab - Image Processing toolbox	General purpose image processing and analysis	1, 2, 4, 10, 13, 17, 22, 24, 35, 38, 45, 53, 60, 62, 63, 81	Active / Sep 2017	Win, MacOS, Linux
ImageJ Fiji	General purpose image processing and analysis	23, 30, 33, 34, 35, 40, 41, 46, 50, 51, 59, 66, 72	Active / Monthly	Win, MacOS, Linux
Vaa3D	Neuronal systems	1, 4, 5, 6, 11, 16, 19, 21, 29, 32, 36, 37, 39, 43	Active / May 2016	Win, MacOS, Linux
SOAX	Biopolymer Networks	15	Active / Apr 2016	Win, MacOS, Linux
NeuronStudio	Neuronal systems	47, 54, 69	Inactive / Nov 2009	Win
Neural Circuit Tracer	Neuronal systems	17, 35	Unknown / May 2014	Win
Neuromantic	Neuronal systems	31	Unknown / Apr 2008	Win
NeuTube	Neuronal systems	39		Win, MacOS, Linux
ORION	Neuronal systems	13, 57	Unkown	Win
FARSight	Quantification of multiple parameters in images of brain tissue	36, 37, 52	Inactive	Win, MacOS, Linux
Reconstruct	segmentation of serial section electron microscopy	51	Inactive / Aug 2007	Win
Tree2Tree	Neuronal systems	45	Inactive / Aug 2015	Matlab scripts
RooTrak	Plant roots	23		Win

***Active - had recent updates (jan 2016 or later) and web sources (Git or other) active
NA - Not applicable
Inactive - Not updated in the past year and web sources appear to be Inactive
Unknown - Not updated recently (dec 2015 or earlier) but may still be supported by the maintainer

Table A.3: Table A.2 continuation: List of software for image analysis and biofilament tracing - Part 2

Software name	Initially intended for	Publication number (Table) that uses or has implementation in it	Status*** / Last release	Supported OS
IMOD	Tomographic reconstruction and for 3D reconstruction of EM sections	27	Active / Jun 2017	Win, MacOS, Linux
OpenCV	General purpose image processing and analysis	7	Active / Dec 2016	NA
VIAS	Integration and alignments of multiple stacks of tiled opcital sections	47, 69, 73	Inactive / Jan 2009	Win
ITK	General purpose image prcessing and analysis toolkit	13, 36, 37	Active / Aug 2017	NA
ImgLib	Segmentation and registration of images	-	Actine / May 2017	NA
ImgLib2	Segmentation and registration of images	-	Active	NA
VTK	Image processing and visualisation toolkit	36, 37	Active / Jun 2017	NA
ilastik	General purpose learning and segmentation for biological images	-	Active / Jun 2017	Win, MacOS, Linux
Scikit-image	General purpose image processing and analysis	-	Active	NA
3DMA Neuron (ExFact® Analysis for Fiber)	Neuronal systems	73	Unknown	Win
HCA-Vision	Neuronal systems	65	Active / Apr 2016	Win
Amira	General purpose bioimage and biomedical image processing and analysis	27, 70, 74	Active	Win
Imaris	General purpose analysis of microscopy images	-	Active	Win
Neurolucida	Neuronal systems	-	Active	Unkown

***Active - had recent updates (jan 2016 or later) and web sources (Git or other) active
NA - Not applicable
Inactive - Not updated in the past year and web sources appear to be Inactive
Unknown - Not updated recently (dec 2015 or earlier) but may still be supported by the maintainer

Table A.4: List of plug-ins

Plug-in/Add-on name	Platform	Organization / Maintained by	Initially intended for	Publication number (Table) that uses or has implementation in it
Simple Neurite Tracer	ImageJ	Unknown	Neuronal networks	30, 40
Simple Neurite Tracer	ImageJ	Unknown	Neuronal networks	34
Simple Neurite Tracer, Tubular Geodesics	ImageJ	EPFL CVLAB	Neuronal networks	1
Anamorf	ImageJ	David Barry	Filamentous Fungi networks	50
SmartRoot	ImageJ	Université Catholique de Louvain	Root Architecture	33
Jfilament	ImageJ	Lehigh University	Biopolymer networks	46
NeuronJ	ImageJ	Erasmus University	Neuronal networks	72
NeuronMetrics	ImageJ	University of Arizona	Neuronal networks	66
Neurphology	ImageJ	National Chiao Tung University, Taiwan	Neuronal networks	41
NeuriteTracer	ImageJ	McGill University	Neuronal networks	59
GLO-RIA	ImageJ	Carnegie Institution for Science - Dinneny Lab	Soil-grown root systems	12
APP	Vaa3D	BigNeuron project	Neuronal networks	32
APP2	Vaa3D	BigNeuron project	Neuronal networks	19
TreMAP	Vaa3D	BigNeuron project	Neuronal networks	5
Rivulet	Vaa3D	BigNeuron project	Neuronal networks	4
NeuroGPS	Vaa3D	BigNeuron project	Neuronal networks	6
SmarTracing	Vaa3D	BigNeuron project	Neuronal networks	11
MOST-Raytracer	Vaa3D	BigNeuron project	Neuronal networks	16
Simple Tracing	Vaa3D	BigNeuron project	Neuronal networks	21
Neutube	Vaa3D	BigNeuron project	Neuronal networks	39
nctuTW	Vaa3D	BigNeuron project	Neuronal networks	29
FarSIGHT Snake	Vaa3D	BigNeuron project	Neuronal networks	36,37

Appendix B: Parameters used as input for testing the filament tracing methods

Table B.1: Parameters used as input in each filament tracing method for the Glu experiment

	Image		RAW	Pre-processed (BS)
Methods	APP v2.621	Parameters	1A background_threshold: -1 (auto) visibility threshold: 30 downsample factor: 2	1A background_threshold: -1 (auto) visibility threshold: 30 downsample factor: 2
		Time (s)	1076.28	497.422
		Comments	-	-
	APP v2.621	Parameters	1B background_threshold: -1 (auto) visibility threshold: 30 downsample factor: 0 (auto)	1B background_threshold: -1 (auto) visibility threshold: 30 downsample factor: 0 (auto)
		Time (s)	444.594	275.328
		Comments	-	-
	NeuronStudio	Parameters	2A Coordinates: (783,156) Voxel dimensions (1x1x2 um) Attach ratio: 1.3 Discretization ratio: 1.0 min length: 3um realign junctions: Yes Use dynamic threshold: Y Use scattered sampling: Y	2A Coordinates: (783,156) Voxel dimensions (1x1x2 um) Attach ratio: 1.3 Discretization ratio: 1.0 min length: 3um realign junctions: Yes Use dynamic threshold: Y Use scattered sampling: Y
		Time (s)	-	-
		Comments	-	-
	NeuronStudio	Parameters	2B Coordinates: (783,156) Voxel dimensions (1x1x2 um) Attach ratio: 1.3 Discretization ratio: 1.3 min length: 3um realign junctions: Yes Use dynamic threshold: Y Use scattered sampling: Y	2B Coordinates: (783,156) Voxel dimensions (1x1x2 um) Attach ratio: 1.3 Discretization ratio: 1.3 min length: 3um realign junctions: Yes Use dynamic threshold: Y Use scattered sampling: Y
		Time (s)	-	-
		Comments	-	-

Table B.1 continuation: Parameters used as input in each filament tracing method for the Glu experiment

Image		RAW	Pre-processed (BS)
	Comments	-	-
Neutube	Parameters	3A Voxel size: 1.2361 x 1.2361 x 2 um Tracing settings: Normal masked: no minimal tracing score: 0.3 Reconstruction settings: Normal Scales: x-y x1; z x1 Neighbor range: 10 Detect crossover: No Remove overshoot: No Resample structure after tracing: Yes	3A Voxel size: 1.2361 x 1.2361 x 2 um Tracing settings: Normal masked: no minimal tracing score: 0.3 Reconstruction settings: Normal Scales: x-y x1; z x1 Neighbor range: 10 Detect crossover: No Remove overshoot: No Resample structure after tracing: Yes
	Time (s)	-	-
	Comments	Didn't work	Didn't work
Neutube	Parameters	3B Voxel size: 1.2361 x 1.2361 x 2 um Tracing settings: Hard masked: no minimal tracing score: 0.3 Reconstruction settings: Normal Scales: x-y x1; z x1 Neighbor range: 10 Detect crossover: No Remove overshoot: No Resample structure after tracing: Yes	3B Voxel size: 1.2361 x 1.2361 x 2 um Tracing settings: Hard masked: no minimal tracing score: 0.3 Reconstruction settings: Normal Scales: x-y x1; z x1 Neighbor range: 10 Detect crossover: No Remove overshoot: No Resample structure after tracing: Yes
	Time (s)	-	-
	Comments	Didn't work	-

Table B.1 continuation: Parameters used as input in each filament tracing method for the Glu experiment

Image		RAW	Pre-processed (BS)
APP2 v2.621	Parameters	4A background_threshold: -1 (auto) auto-downsample: Y use GSDT: N allow gap: N Radius from 2D: Y Auto-resample SWC: Y high intensity background: N brightfield: N cnn_type: 3 length_thres: 5 SR_ratio: 0.333333	4A background_threshold: -1 (auto) auto-downsample: Y use GSDT: N allow gap: N Radius from 2D: Y Auto-resample SWC: Y high intensity background: N brightfield: N cnn_type: 3 length_thres: 5 SR_ratio: 0.333333
	Time (s)	14.296	9.375
	Comments	-	-
APP2 v2.621	Parameters	4B background_threshold: -1 (auto) auto-downsample: Y use GSDT: Y allow gap: N Radius from 2D: Y Auto-resample SWC: Y high intensity background: N brightfield: N cnn_type: 3 length_thres: 5 SR_ratio: 0.333333	4B background_threshold: -1 (auto) auto-downsample: Y use GSDT: Y allow gap: N Radius from 2D: Y Auto-resample SWC: Y high intensity background: N brightfield: N cnn_type: 3 length_thres: 5 SR_ratio: 0.333333
	Time (s)	13.421	8.875
	Comments	-	-
NeuroGPSTRee	Parameters	5A 1.2361 1.2361 2.000 10 10 150	5A 1.2361 1.2361 2.000 10 10 150
	Time (s)	-	-
	Comments	Didn't work	-
NeuroGPSTRee	Parameters	5B 1.2361 1.2361 2.000 10 10 100	5B 1.2361 1.2361 2.000 10 10 100
	Time (s)	-	-
	Comments	Didn't work	-

Table B.2: Parameters used as input in each filament tracing method for the PGal experiment

	Images		Pre-processed (BS)
Methods	APP v2.621	Parameters	1A background_threshold: -1 (auto) visibility threshold: 30 downsample factor: 2
		Time (s)	63.266
		Comments	
	APP v2.621	Parameters	1B background_threshold: -1 (auto) visibility threshold: 30 downsample factor: 0 (auto)
		Time (s)	21.75
		Comments	-
	NeuronStudio	Parameters	2A Coordinates: (773,916) Voxel dimensions (1x1x2 um) Attach ratio: 1.3 Discretization ratio: 1.0 min length: 3um realign junctions: Yes Use dynamic threshold: Y Use scattered sampling: Y
		Time (s)	-
		Comments	Done
	NeuronStudio	Parameters	2B Coordinates: (773,916) Voxel dimensions (1x1x2 um) Attach ratio: 1.3 Discretization ratio: 1.3 min length: 3um realign junctions: Yes Use dynamic threshold: Y Use scattered sampling: Y
		Time (s)	-
		Comments	-
	Neutube	Parameters	3A Voxel size: 1.2361 x 1.2361 x 2 um Tracing settings: Normal masked: no minimal tracing score: 0.3 Reconstruction settings: Normal Scales: x-y x1; z x1 Neighbor range: 15 Detect crossover: yes Remove overshoot: yes Resample structure after tracing: Yes
		Time (s)	-
		Comments	-

Table B.2 continuation: Parameters used as input in each filament tracing method for the PGal experiment

Neutube	Parameters	3B Voxel size: 1.2361 x 1.2361 x 2 um Tracing settings: Normal masked: no minimal tracing score: 0.3 Reconstruction settings: Normal Scales: x-y x1; z x1 Neighbor range: 10 Detect crossover: No Remove overshoot: No Resample structure after tracing: Yes
	Time (s)	-
	Comments	-
APP2 v2.621	Parameters	4A background_threshold: -1 (auto) auto-downsample: Y use GSDT: N allow gap: N Radius from 2D: Y Auto-resample SWC: Y high intensity background: N brightfield: N cnn_type: 3 length_thres: 5 SR_ratio: 0.333333
	Time (s)	1
	Comments	-
APP2 v2.621	Parameters	4B background_threshold: -1 (auto) auto-downsample: Y use GSDT: Y allow gap: N Radius from 2D: Y Auto-resample SWC: Y high intensity background: N brightfield: N cnn_type: 3 length_thres: 5 SR_ratio: 0.333333
	Time (s)	1.016
	Comments	-
NeuroGPSTRee	Parameters	5A 1.2361 1.2361 2.000 10 10 150
	Time (s)	-
	Comments	-

Appendix C: Screenshots of tracing results of various biofilament tracing methods

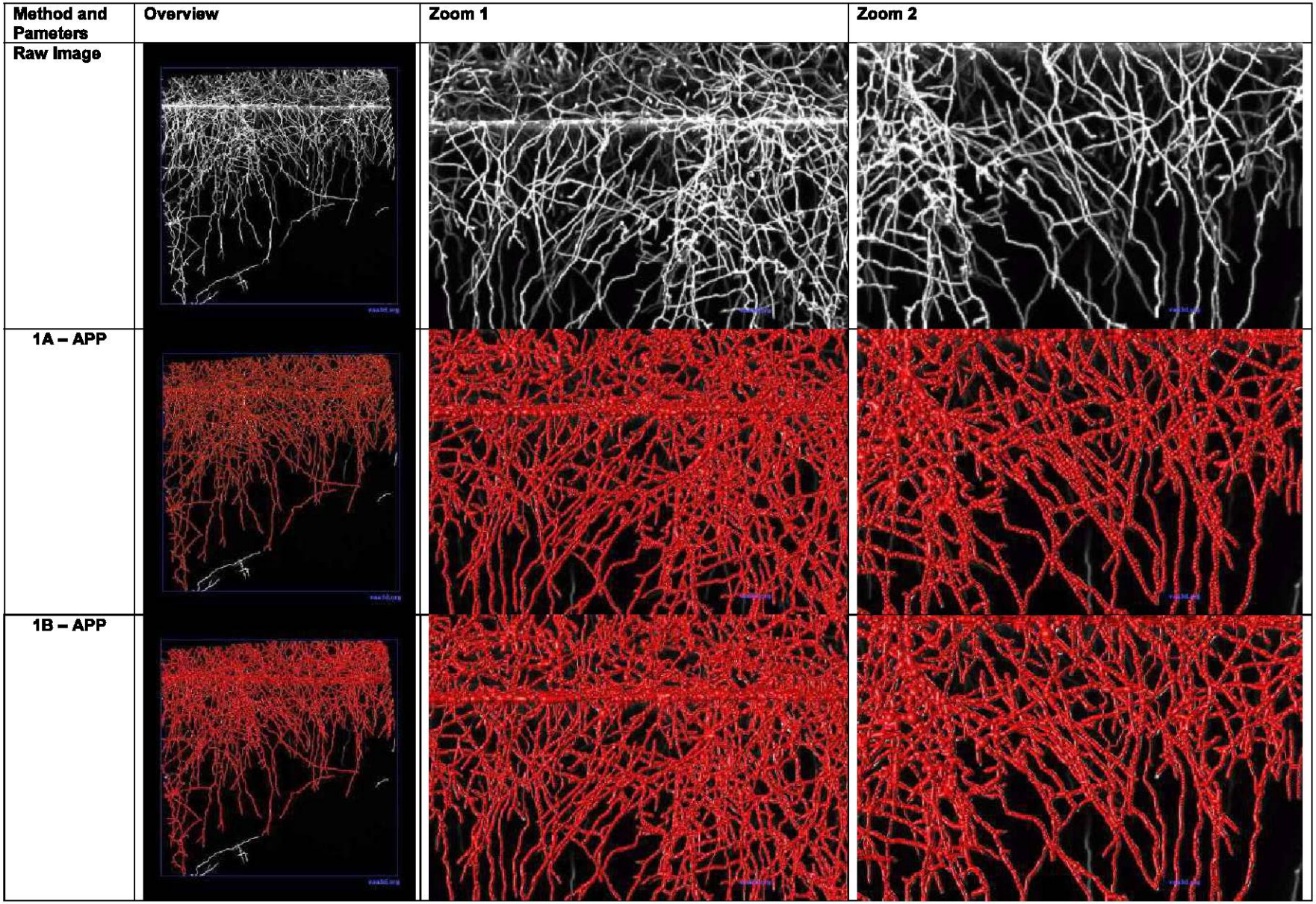

Figure C.1: Screenshots of the results of filament tracing methods for Glu experiment.

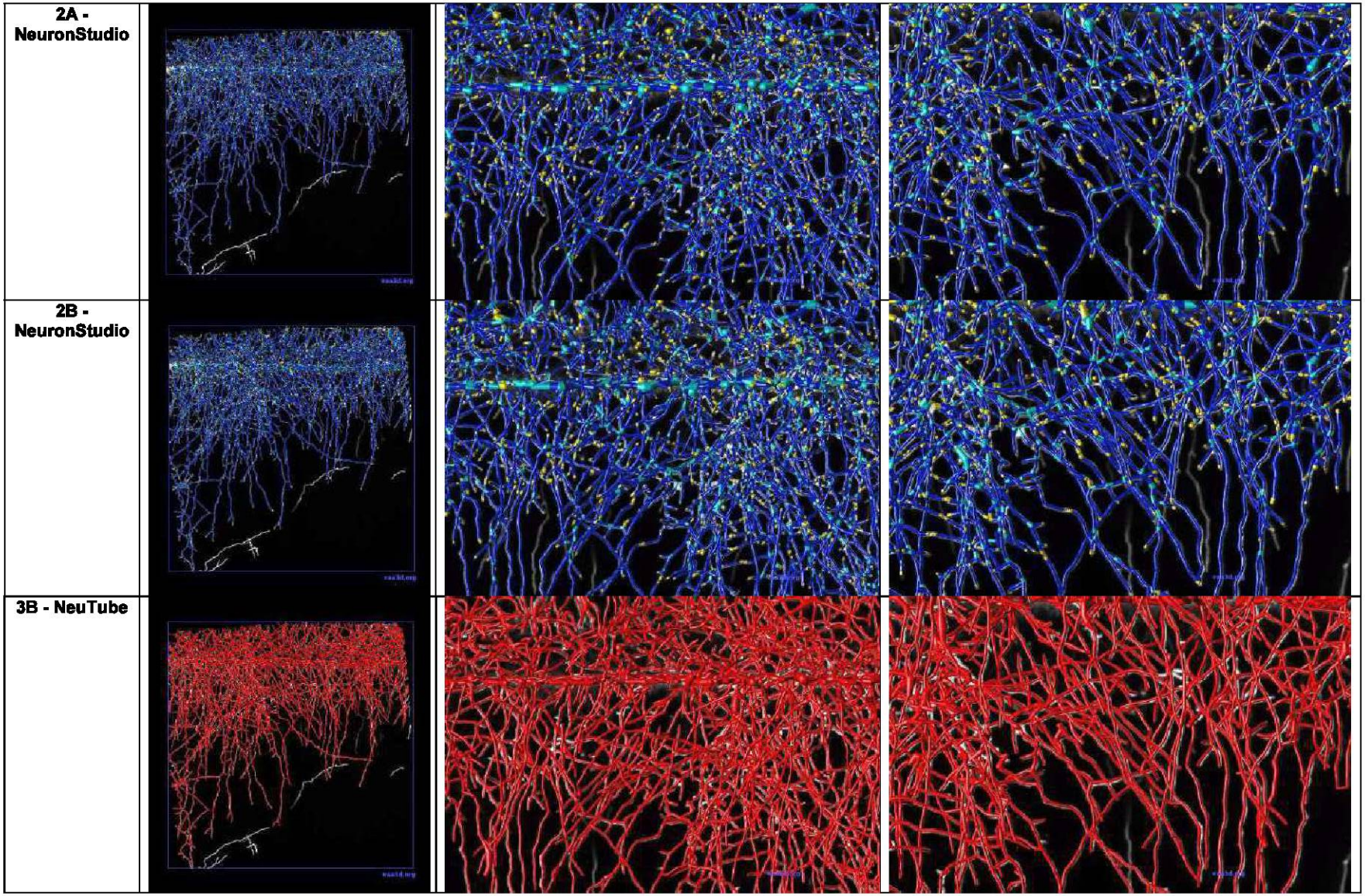

Figure C.2: Screenshots of the results of filament tracing methods for Glu experiment.

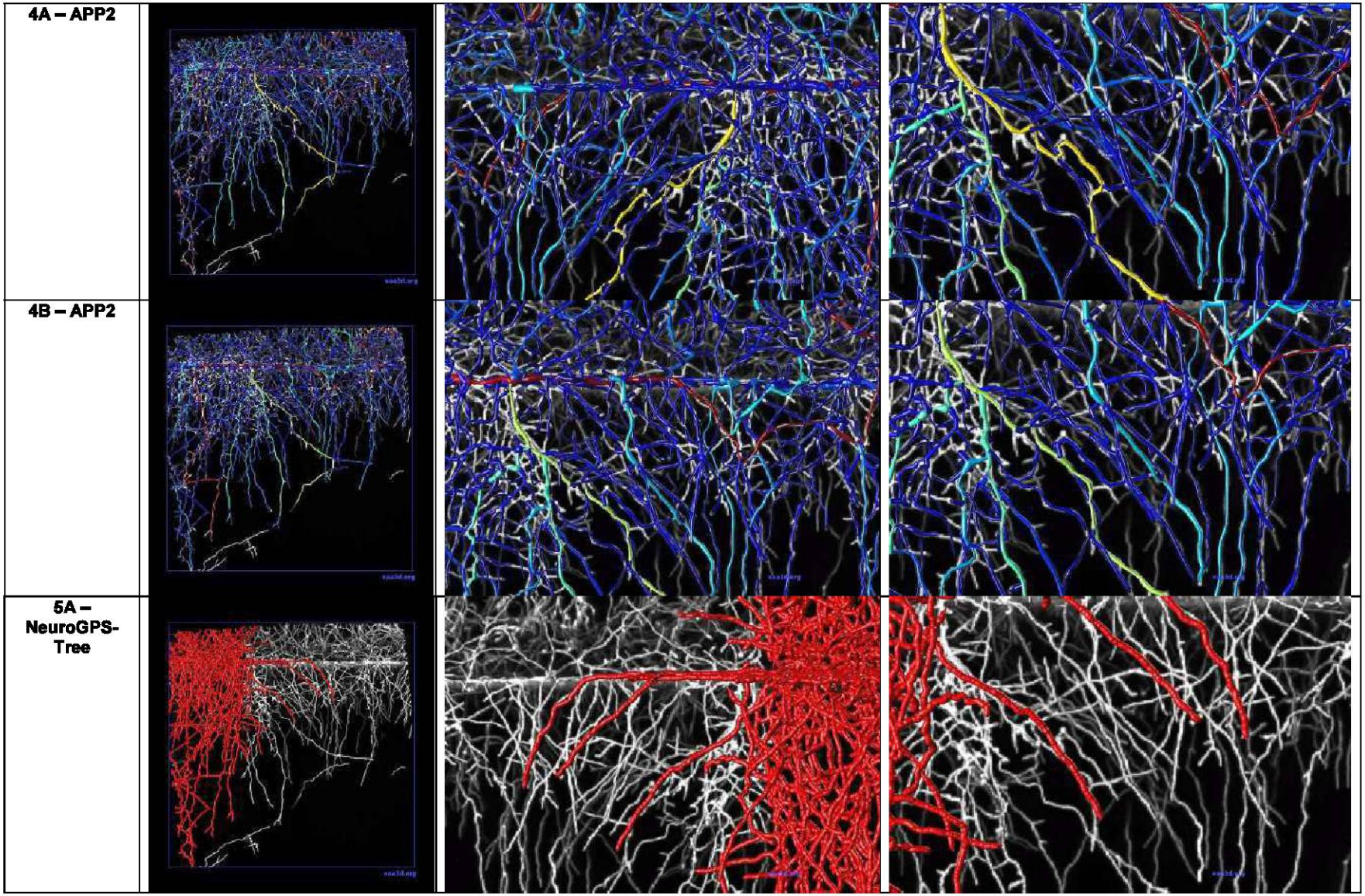

Figure C.3: Screenshots of the results of filament tracing methods for Glu experiment.

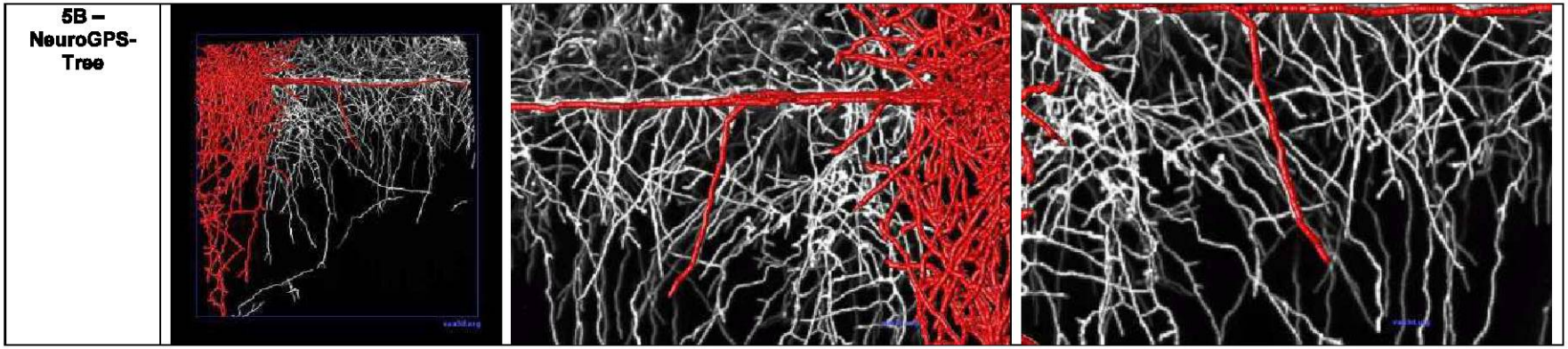

Figure C.4: Screenshots of the results of filament tracing methods for Glu experiment.

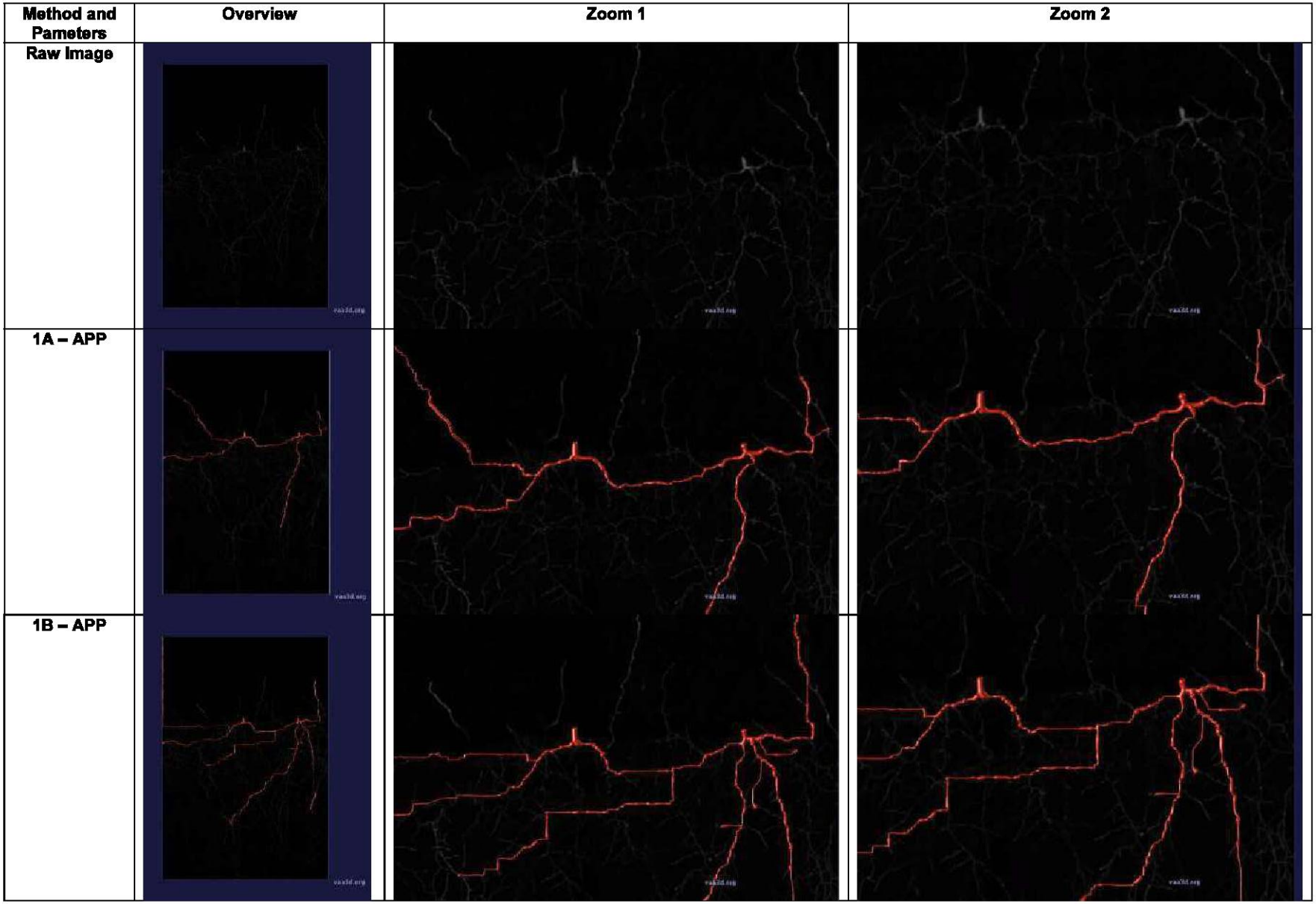

Figure C.5: Screenshots of the results of filament tracing methods for PGal experiment.

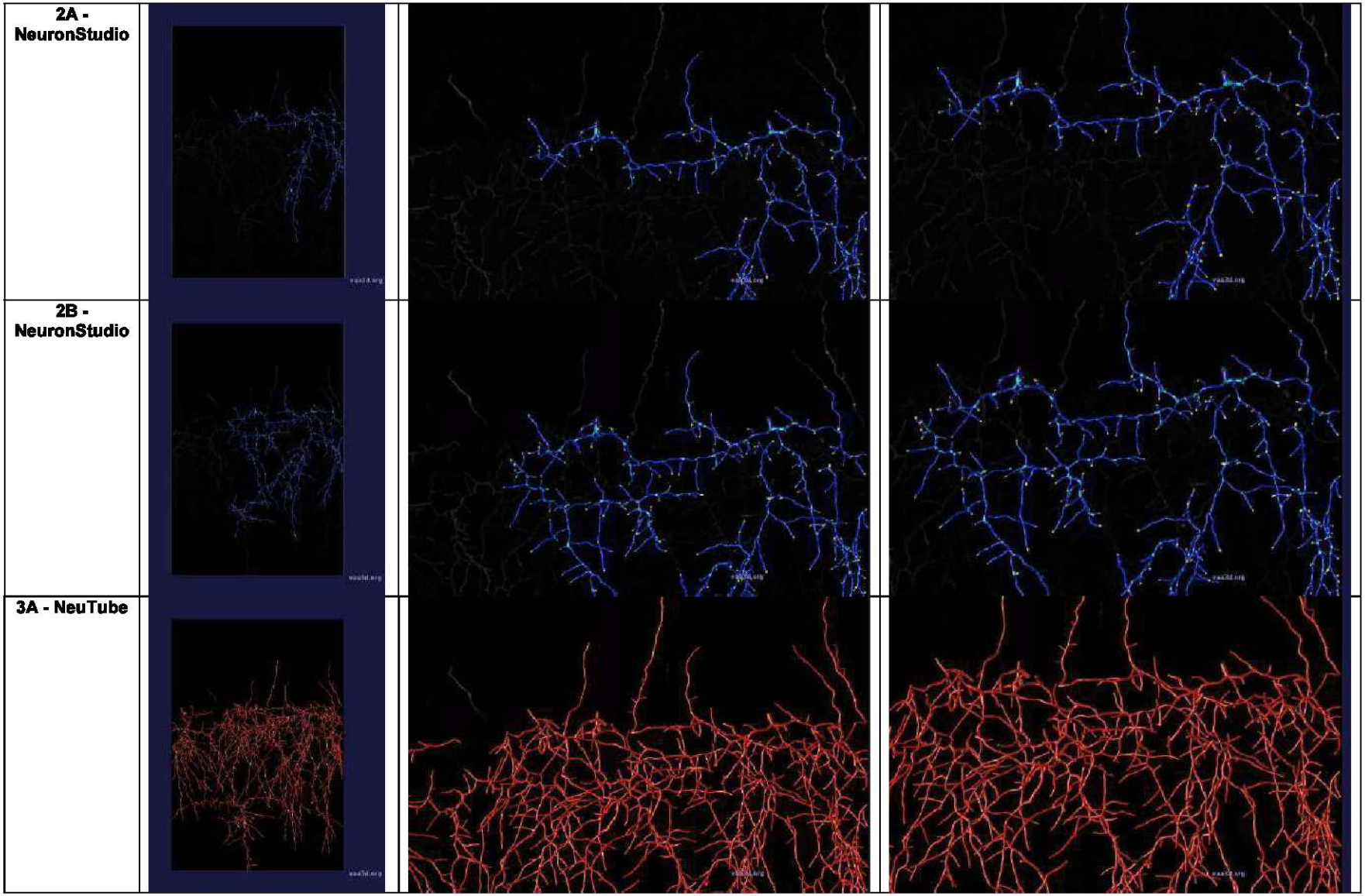

Figure C.6: Screenshots of the results of filament tracing methods for PGal experiment.

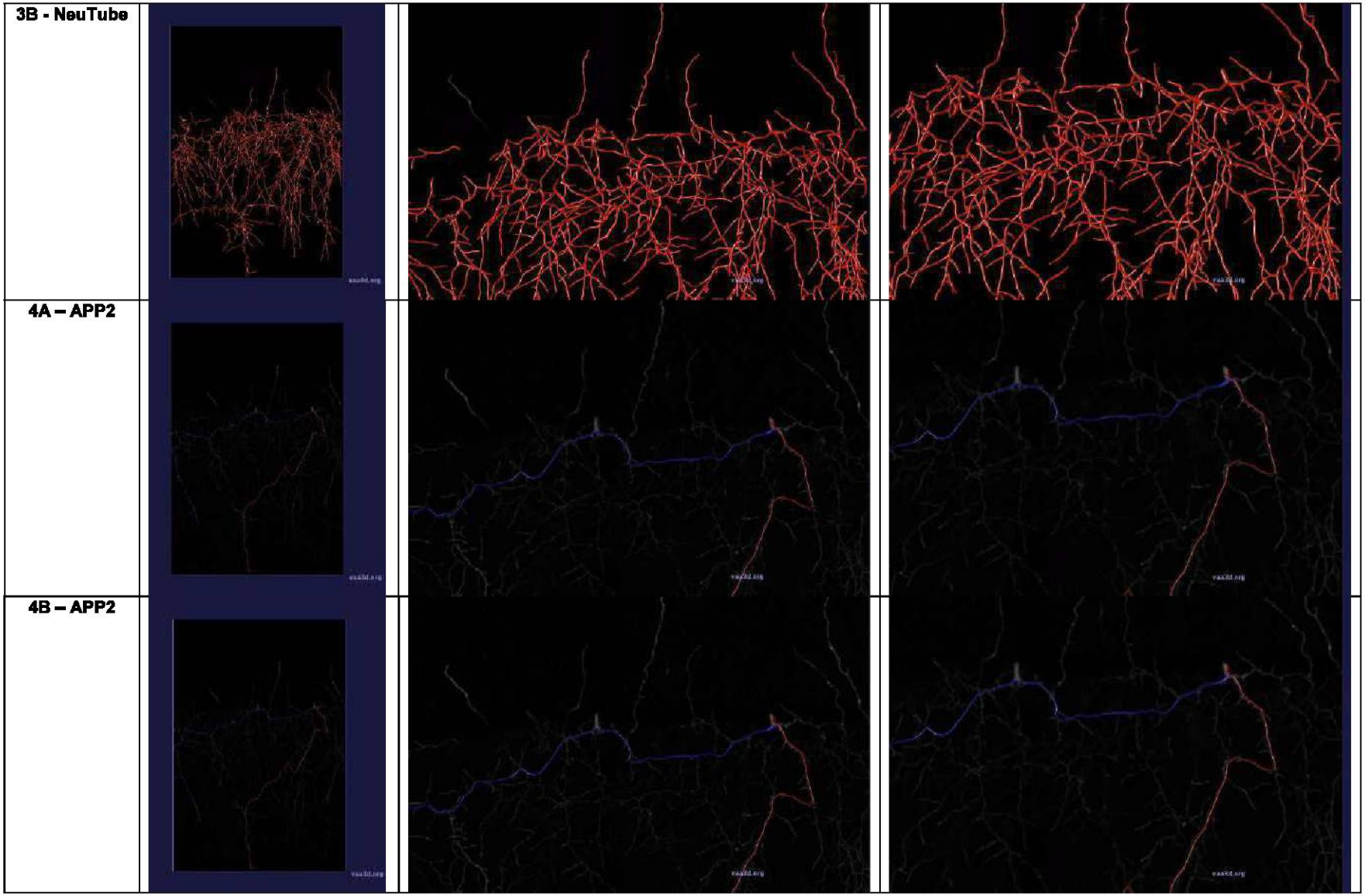

Figure C.7: Screenshots of the results of filament tracing methods for PGal experiment.

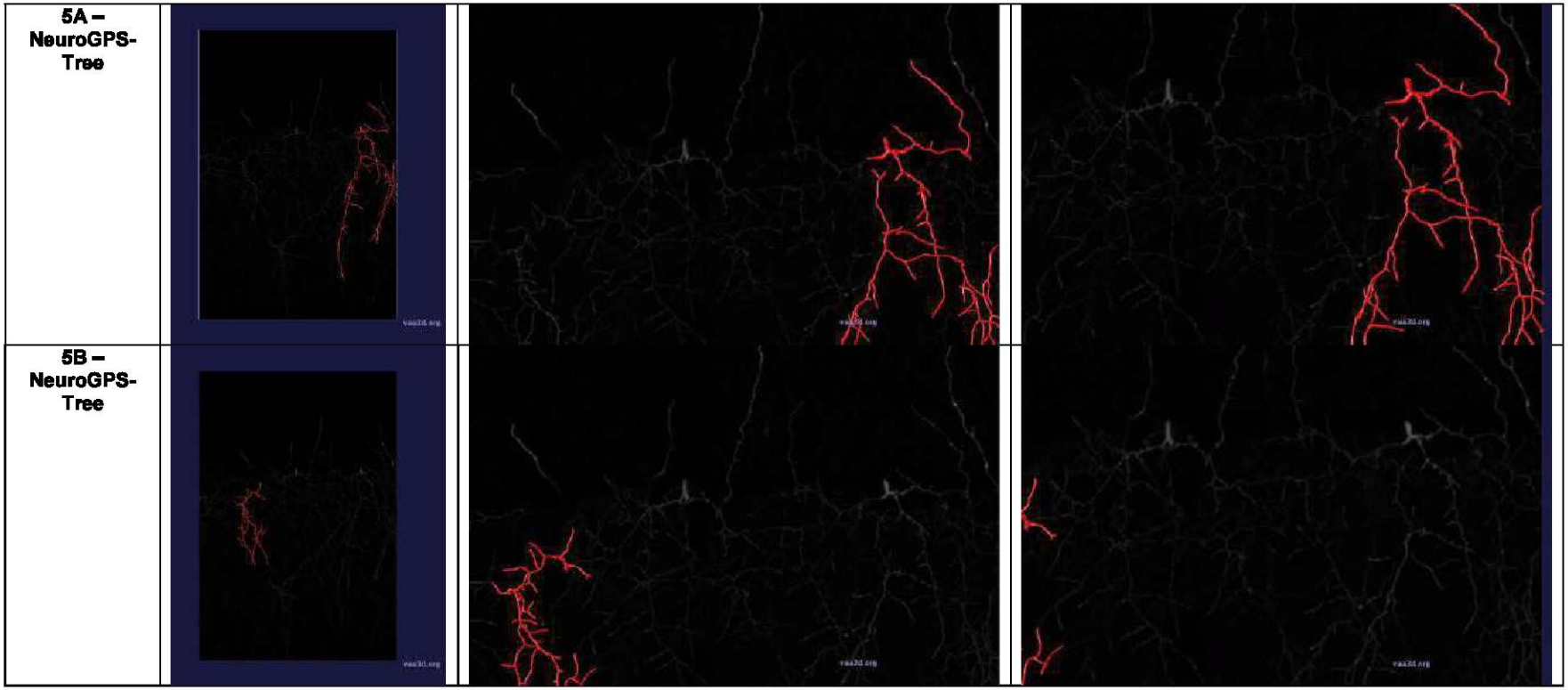

Figure C.8: Screenshots of the results of filament tracing methods for PGal experiment.

Appendix D: Parameters used for NeuTube method to extract graph representation of all frames of the Glucose and Polygalacturonate experiments

Table D.1: Parameters used in Glucose experiment

Frame	1	2	3	4	5	6	7
Glu	Not submitted to filament tracing	Voxel size: 1.2361 x 1.2361 x 2 um Tracing settings: Hard masked: no minimal tracing score: 0.3 Reconstruction settings: Normal Scales: x-y x1; z x1 Neighbor range: 5 Detect crossover: No Remove overshoot: Yes Resample structure after tracing: Yes	Voxel size: 1.2361 x 1.2361 x 2 um Tracing settings: Hard masked: no minimal tracing score: 0.3 Reconstruction settings: Hard Scales: x-y x1; z x1 Neighbor range: 10 Detect crossover: No Remove overshoot: yes Resample structure after tracing: Yes	Voxel size: 1.2361 x 1.2361 x 2 um Tracing settings: Hard masked: no minimal tracing score: 0.3 Reconstruction settings: Hard Scales: x-y x1; z x1 Neighbor range: 10 Detect crossover: No Remove overshoot: Yes Resample structure after tracing: Yes	Voxel size: 1.2361 x 1.2361 x 2 um Tracing settings: Hard masked: no minimal tracing score: 0.3 Reconstruction settings: Hard Scales: x-y x1; z x1 Neighbor range: 10 Detect crossover: No Remove overshoot: Yesw Resample structure after tracing: Yes	Voxel size: 1.2361 x 1.2361 x 2 um Tracing settings: Hard masked: no minimal tracing score: 0.3 Reconstruction settings: Hard Scales: x-y x1; z x1 Neighbor range: 10 Detect crossover: yes Remove overshoot: yes Resample structure after tracing: Yes	Not submitted to filament tracing. Densely packed filaments

Table D.2: Parameters used in Polygalacturonate experiment

Frame	1	2	3	4	5
Pgal	Voxel size: 1.2361 x 1.2361 x 2 um Tracing settings: Hard masked: no mimimal tracing score: 0.3 Reconstruction settings: Hard Scales: x-y x1; z x1 Neighbor range: 5 Detect crossover: No Remove overshoot: No Resample structure after tracing: Yes	Voxel size: 1.2361 x 1.2361 x 2 um Tracing settings: Normal masked: no mimimal tracing score: 0.3 Reconstruction settings: Easy Scales: x-y x1; z x1 Neighbor range: 10 Detect crossover: No Remove overshoot: No Resample structure after tracing: Yes	Voxel size: 1.2361 x 1.2361 x 2 um Tracing settings: Normal masked: no mimimal tracing score: 0.3 Reconstruction settings: Easy Scales: x-y x1; z x1 Neighbor range: 5 Detect crossover: No Remove overshoot: No Resample structure after tracing: Yes	Voxel size: 1.2361 x 1.2361 x 2 um Tracing settings: Normal masked: no minimal tracing score: 0.3 Reconstruction settings: Easy Scales: x-y x1; z x1 Neighbor range: 5 Detect crossover: Yes Remove overshoot: Yes Resample structure after tracing: Yes	Voxel size: 1.2361 x 1.2361 x 2 um Tracing settings: Normal masked: no minimal tracing score: 0.3 Reconstruction settings: Easy Scales: x-y x1; z x1 Neighbor range: 5 Detect crossover: Yes Remove overshoot: Yes Resample structure after tracing: Yes

Appendix E: Details regarding the quality of our images

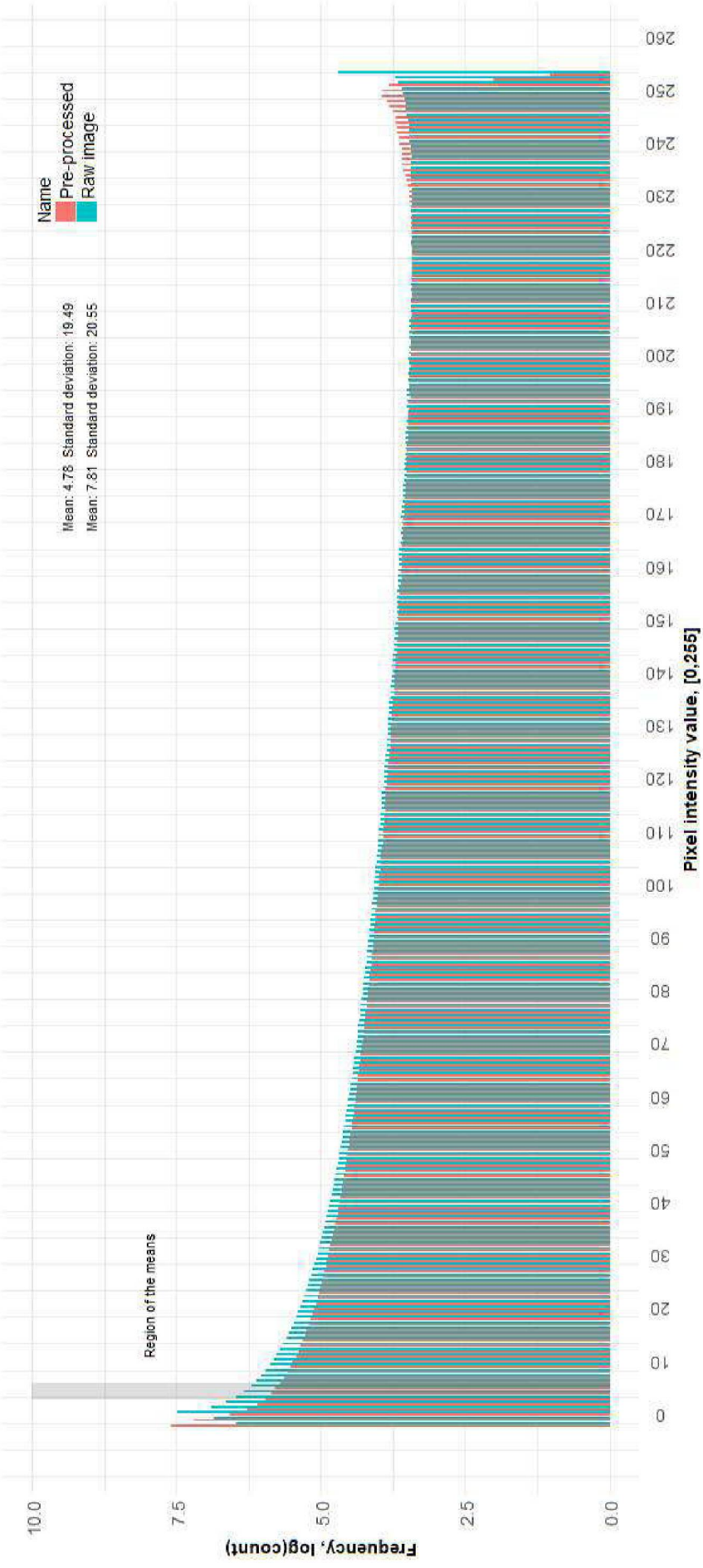

Figure E.1: Image intensity histogram for the Glu raw image and the image pre-processed with *Background subtraction* (rolling ball) (Sternberg, 1983) from ImageJ Fiji (Schindelin et al., 2012).

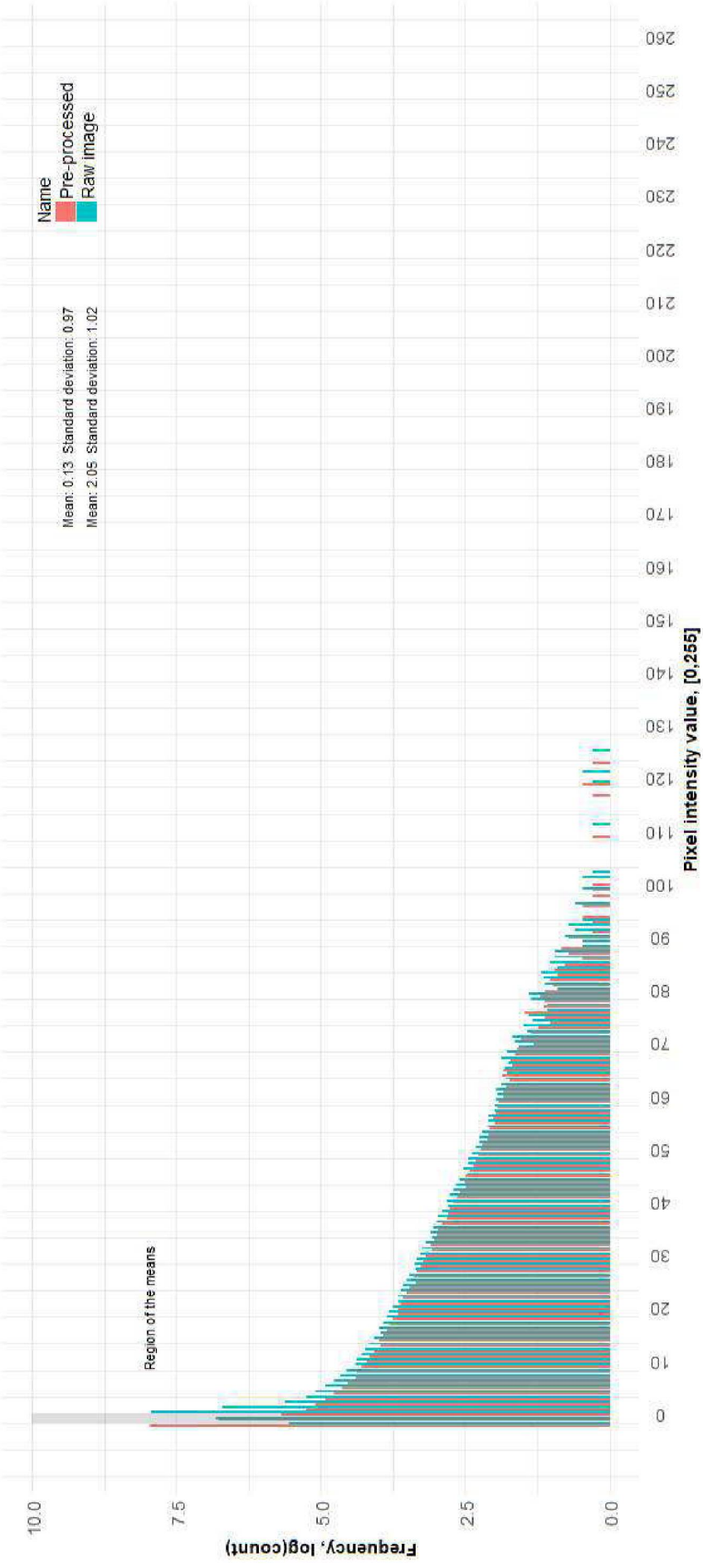

Figure E.2: Image intensity histogram for the PGal raw image and the image pre-processed with *Background subtraction* (rolling ball) (Sternberg, 1983) from ImageJ Fiji(Schindelin et al., 2012).

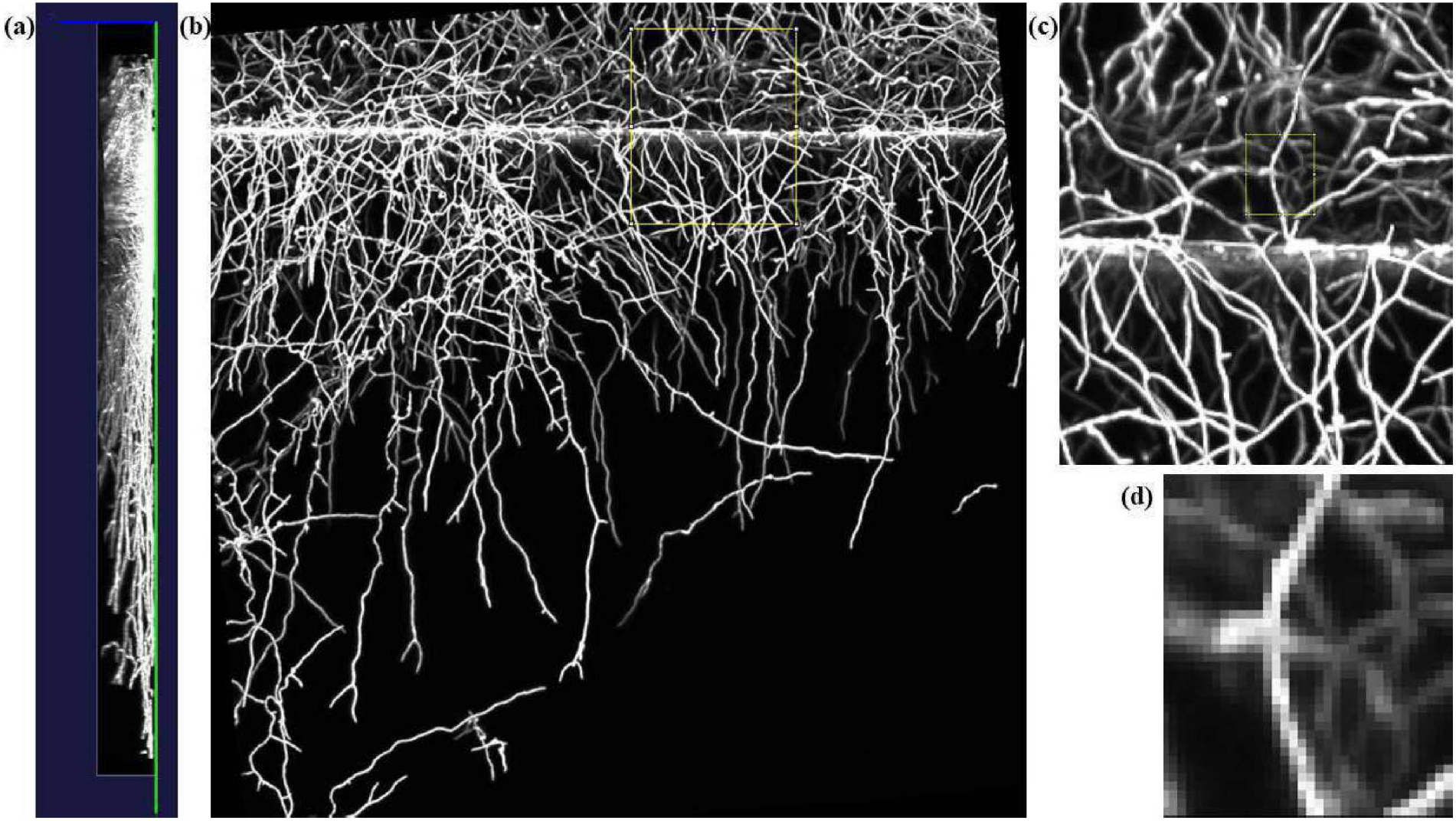

Figure E.3: (a) a view of a yz plane of a frame from Glucose experiment. It is possible to note that the intensity of the filaments decrease as z changes. (b) A view of a frame of the Glucose experiment in xy plane and (c) a zoomed region of the same image and (d) a sufficiently zommed image from the same image that shows the approximate size of the filaments is small compared to the image resolution: the filament size ranges from 2-5 pixels.

Appendix F: Biofilament metrics

The matlab code presented below is part of the `Biofilament metrics` function library.

```
%reads file
Neutube_3B = load_v3d_swc_file('D:\Leandro\TESTES COM IMAGENS\Biomass_Calculation\Biomass_Profiles_perFrame\2_t5.swc');

%makes swc matrix isotropic
Neutube_3B=anisotropic_to_isotropic_swc(Neutube_3B,1.2361,2.0000);

%creates adjacency matrix from swc matrix
Neutube_3B_adjMat=swc_to_AdjMat(Neutube_3B);

%creates a graph from the adjacency matrix
Neutube_3B_graph=digraph(Neutube_3B_adjMat);

%adds x,y and z coordinates of the swc matrix to the graph
Neutube_3B_graph=add_swc_info_to_graph(Neutube_3B_graph,Neutube_3B);

%calculates y_distances of every edge in the graph
y_dist=y_distances(Neutube_3B_graph);

%calculates euclidean distances of every edge in R^3 space and adds the distance results to the graph
distances=eucli_distances(Neutube_3B_graph);
Neutube_3B_graph.Edges{:,2}=distances;

profiles_t5_50=biomass_profiles(Neutube_3B,'y',50,3.7);
profiles_t5_40=biomass_profiles(Neutube_3B,'y',40,3.7);
profiles_t5_30=biomass_profiles(Neutube_3B,'y',30,3.7);
profiles_t5_20=biomass_profiles(Neutube_3B,'y',20,3.7);

function [biomass_profile,total_volume]=biomass_profiles(swc_mat,coordinate,n_bins,radius)

% the function biomass_profiles calculates the biomass profile of the image in n_bins regions as a
% function of position in space

% For example: biomass_profiles(graph,'y',20,5) calculates the biomass in 20
```

```
% sections of xz planes
% The results may be ploted and will show
%
% b ^
% i | .
% o | . .
% m | . .
% a | . .
% s |.__________.____>
% s y depth

if coordinate=='x'
   swc_column=3;
   graph_node_column=1;
   planes=[4 5];
elseif coordinate=='y'
   swc_column=4;
   graph_node_column=2;
   planes=[3 5];
   if coordinate=='z'
      swc_column=5;
      graph_node_column=3;
      planes=[3 4];
   end
end


%create full graph of the swc_mat and add the info from the swc
   ↪ to the
%graph and also calculates the euclidean distances of the edges
full_adjMat=swc_to_AdjMat(swc_mat);
full_graph=digraph(full_adjMat);
full_graph=add_swc_info_to_graph(full_graph,swc_mat);
full_graph.Edges{:,2} =eucli_distances(full_graph);

% gets lower and upper bounds of the swc_matrix and calculates
   ↪ the range and
% bin range
min_val=min(swc_mat(:,swc_column));
max_val=max(swc_mat(:,swc_column));
range=max_val-min_val;
bin_range=range/n_bins;

% calculates the total volume of each bin
% col 1 are the minimum values
plane_limits(1,1)= min(swc_mat(:,planes(1)));
plane_limits(2,1)= min(swc_mat(:,planes(2)));
% column 2 are the maximum values
```

```
80  plane_limits(1,2)= max(swc_mat(:,planes(1)));
81  plane_limits(2,2)= max(swc_mat(:,planes(2)));
82
83  ranges=plane_limits(:,2)-plane_limits(:,1);
84  area=ranges(1)*ranges(2);
85  volume=area*bin_range;
86
87  %creates the output matrix
88  biomass_profile=zeros(n_bins,2);
89
90  %to begin the loop and calculate the volumes, the initial
        ↪ bin_value is
91  %equal to the minimum value of the chosen coordinate
92  bin_val=min_val;
93  for cont=1:n_bins
94
95      %cuts the full swc matrix into section 'cont'
96      sectioned_swc_mat=section_swc(swc_mat,coordinate,bin_val,
            ↪ bin_val+bin_range);
97
98      %creates adj matrix and graph of the 'cont' sectioned swc
99      sectioned_graph=subgraph(full_graph,sectioned_swc_mat(:,1));
100
101     % average position and biomass volume calculation
102     biomass_profile(cont,1)=(bin_val+bin_range/2);
103     biomass_profile(cont,2)= biomass_profile(cont,2)+
            ↪ graph_volume(sectioned_graph,radius);
104
105     if cont>=2 && cont<=(n_bins-1)
106         % determines the edges crossing the bounds from the 2nd
                ↪ bin to
107         % the (n-1)th bin and computes the aditional volumes of
                ↪ the edges that
108         % cross the bounds delimited by bin_val and bin_val+
                ↪ bin_range
109
110
111         % gets the sorted nodes_outofbound_edges vector that has
                ↪ all nodes
112         % and creates a subgraph. With this subgraph, the vectors
113         % representing the edge are computed
114         [outofbound,nodes_outofbound_edges]=find_outofbounds(
                ↪ sectioned_swc_mat);
115         outofbounds_subgraph=subgraph(full_graph,
                ↪ nodes_outofbound_edges);
116         edge_vectors=calculate_edge_vectors(outofbounds_subgraph)
                ↪ ;
117
```

```
118         %gets the number of edges that cross bounds delimited by
               ↪ bin_val
119         %and bin_val+bin_range
120         [nEdges,~]=size(outofbounds_subgraph.Edges);
121
122         %creates a vector to compute the aditional volumes of the
               ↪  current
123         % previous, current and next bin
124         %biomass bounds, index 1 = biomass to be added to
               ↪ previous bin
125         % index 2 = biomass to be added to current bin
126         % index 3 = biomass to be added to next bin
127        biomass_bounds=[0 0 0];
128
129         %loop to calculate the volumes of the edges and add to
               ↪ appropriate
130         %biomass_bouns bin
131         for i=1:nEdges
132            nodes=outofbounds_subgraph.Edges{i,1};
133            parent_node_coordinate=outofbounds_subgraph.Nodes{
                  ↪ nodes(1),graph_node_column};
134            daughter_node_coordinate=outofbounds_subgraph.Nodes{
                  ↪ nodes(2),graph_node_column};
135            %calculates the bin_val minus parent coordinate and
136            %bin_val+bin_range minus parent coordinate
137            deltamin=bin_val-parent_node_coordinate;
138            deltamax=(bin_val+bin_range)-parent_node_coordinate;
139            %case 1
140            if sign(deltamin)==-1 && sign(deltamax)==1
141              if bin_val>daughter_node_coordinate && (bin_val+
                    ↪ bin_range)>daughter_node_coordinate
142                 length_fraction=deltamin/edge_vectors(i,
                       ↪ graph_node_column);
143                 edge_volume=length_fraction*outofbounds_subgraph.
                       ↪ Edges{i,2}*radius;
144                 biomass_bounds(2)=biomass_bounds(2)+edge_volume;
145
146                 edge_volume=(1-length_fraction)*
                       ↪ outofbounds_subgraph.Edges{i,2}*radius;
147                 biomass_bounds(1)=biomass_bounds(1)+edge_volume;
148
149              elseif (bin_val+bin_range)<daughter_node_coordinate
                    ↪  && bin_val<daughter_node_coordinate
150                 length_fraction=deltamax/edge_vectors(i,
                       ↪ graph_node_column);
151                 edge_volume=length_fraction*outofbounds_subgraph.
                       ↪ Edges{i,2}*radius;
152                 biomass_bounds(2)=biomass_bounds(2)+edge_volume;
```

```
153
154                 edge_volume=(1-length_fraction)*
                        ↪ outofbounds_subgraph.Edges{i,2}*radius;
155                 biomass_bounds(3)=biomass_bounds(3)+edge_volume;
156             end
157         %case 2
158         else
159             if sign(deltamin)==1 || sign(deltamax)==1
160                 length_fraction=deltamin/edge_vectors(i,
                        ↪ graph_node_column);
161                 edge_volume=length_fraction*
                        ↪ outofbounds_subgraph.Edges{i,2}*radius;
162                 biomass_bounds(1)=biomass_bounds(1)+edge_volume
                        ↪ ;
163
164                 edge_volume=(1-length_fraction)*
                        ↪ outofbounds_subgraph.Edges{i,2}*radius;
165                 biomass_bounds(2)=biomass_bounds(2)+edge_volume
                        ↪ ;
166             end
167             if sign(deltamin)==-1 || sign(deltamax)==-1
168                 length_fraction=deltamax/edge_vectors(i,
                        ↪ graph_node_column);
169                 edge_volume=length_fraction*outofbounds_subgraph
                        ↪ .Edges{i,2}*radius;
170                 biomass_bounds(3)=biomass_bounds(3)+edge_volume;
171
172                 edge_volume=(1-length_fraction)*
                        ↪ outofbounds_subgraph.Edges{i,2}*radius;
173                 biomass_bounds(2)=biomass_bounds(2)+edge_volume;
174             end
175         end
176     end
177
178     biomass_profile(cont-1,2)=biomass_profile(cont-1,2)+
            ↪ biomass_bounds(1);
179     biomass_profile(cont ,2)=biomass_profile(cont ,2)+
            ↪ biomass_bounds(2);
180     biomass_profile(cont+1,2)=biomass_profile(cont+1,2)+
            ↪ biomass_bounds(3);
181     end
182     bin_val=bin_val+bin_range;
183 end
184 total_volume=sum(biomass_profile(:,2));
185 %with all computed volumes, calculate volume fraction
186 biomass_profile(:,2)=(biomass_profile(:,2)/volume);
187
188 function network_volume=graph_volume(graph,radius)
```

```
189
190 % The function network_volume receives a graph that has weights
    ↪  (positioned in column 2 of graph.Edges)
191 % as edge distances and radii (positioned in column 4 of graph.
    ↪ Nodes)
192
193 % if called as graph_volume=(graph) will calculate the volume
    ↪ with the
194 % average radius of the nodes of an edge.
195
196 if nargin==1
197     %to be programmed
198 else
199     network_volume=sum(graph.Edges{:,2})*radius;
200 end
201
202
203 % This function swc_to_adjMat gets the matrix extracted from
    ↪ load_v3d_swc() of the swc file and
204 % transforms it into the adjacency matrix of a graph
205
206 function adjMat=swc_to_adjMat(swc_mat)
207
208 %gets the number of nodes from the swc matrix
209 [nNodes,nParam]=size(swc_mat);
210
211 %creates the adjacency matrix with the number of nodes
212 adjMat=zeros(nNodes);
213
214
215 for cont=1:nNodes
216     if(swc_mat(cont,7)~=-1 && sum(swc_mat(:,1)==swc_mat(cont,7))
        ↪ ~=0)
217         adjMat(swc_mat(cont,1),swc_mat(cont,7))=1;
218     end
219 end
220
221
222 function distances=eucli_distances(graph)
223
224 % This function calculates the euclidean distances between the
    ↪ edges of a graph
225 % The graph must have the graph.Nodes data with x,y and z
    ↪ coordinates of the
226 % nodes in graph.Nodes columns 1, 2 and 3.
227
228 [nEdges,~]=size(graph.Edges);
229 distances=zeros(nEdges,1);
```

```
230
231
232 for cont=1:nEdges
233     nodes=graph.Edges{cont,1};
234     distances(cont)= sum((graph.Nodes{nodes(1),1:3}-graph.Nodes{
        ↪ nodes(2),1:3}).^2).^0.5 ;
235 end
236
237
238 function graph=add_swc_info_to_graph(graph,swc_mat)
239
240 %adds x,y,z coordinates information and radius from swc matrix
        ↪ to graph
241 graph.Nodes.xData=swc_mat(:,3);
242 graph.Nodes.yData=swc_mat(:,4);
243 graph.Nodes.zData=swc_mat(:,5);
244 graph.Nodes.radius=swc_mat(:,6);
245
246
247
248 function sectioned_swc=section_swc(swc_mat,coordinate,
        ↪ lower_bound,upper_bound)
249
250 % separates the swc into a smaller matrices that include only
        ↪ the nodes
251 % within an upper and lower bound of the selected coordinate
252
253 if coordinate=='x'
254     swc_column=3;
255 elseif coordinate=='y'
256     swc_column=4;
257     if coordinate=='z'
258         swc_column=5;
259     end
260 end
261
262 indices= swc_mat(:,swc_column)>lower_bound & swc_mat(:,
        ↪ swc_column)<upper_bound;
263 sectioned_swc=swc_mat(indices,:);
264
265 function isotropic_swc_mat=anisotropic_to_isotropic_swc(swc_mat
        ↪ ,xy_scale,xy_z_ratio)
266
267 % anisotropic swc to isotropic swc
268 % this function receives an swc matrix variable, which was read
        ↪  from load_v3d_swc() and obtained by
269 % voxel scale tracing 1 x 1 x 1, and changes to appropriate
        ↪ scale of the
```

```
% image, set by the user

%inputs
% swc matrix -> swc_mat
% xy_scale -> scale of the xy pixels
% xy_z_ratio -> xy/z scale ratio or z scale (if xy_z_ratio>1)

isotropic_swc_mat=swc_mat;

isotropic_swc_mat(:,3:4)=swc_mat(:,3:4)*xy_scale;

if(xy_z_ratio>1)
   isotropic_swc_mat(:,5)=swc_mat(:,5)*xy_z_ratio;
elseif xy_z_ratio<0 && xy_z_ratio>0
   z_scale=xy_scale/xy_z_ratio;
   isotropic_swc_mat(:,5)=swc_mat(:,5)*z_scale;
end
```